Prepared by:
GEER Association
geerassociation.org
Hokkaido-Iburi Earthquake
Version 1.0
February 2019

Seismological, Geological, and Geotechnical Engineering Aspects of the 2018 M_W 6.6 Hokkaido Eastern Iburi Earthquake

Prepared by:
GEER Association
geerassociation.org
Hokkaido-Iburi Earthquake
Version 1.0
February 2019

Seismological, Geological, and Geotechnical Engineering Aspects of the 2018 M_W 6.6 Hokkaido Eastern Iburi Earthquake

Geotechnical Extreme Events Reconnaissance Association
Version 1.0
February, 2019

Prepared By:

Robert Kayen, Brad Wham, Alex Grant, Mikami Atsushi, Donald Anderson, Paolo Zimmaro, Pengfei Wang, Yi Tyan Tsai, Jeff Bachhuber, Chris Madugo, Joseph Sun, Chris Hitchcock, and Matthew Motto

Contents

List of Tables

List of Figures

Important Case Histories

Well-documented case histories of damaged areas from the 2018 **M**6.6 Hokkaido Eastern Iburi earthquake provide the data needed to develop design procedures used by geotechnical engineers. With GEER's open-community approach we seek to document important case histories that may provide robust empirical data needed by earthquake professionals to advance the art and practice of geotechnical engineering. Field observations are particularly important in the discipline of geotechnical engineering, because it is difficult to replicate conditions in the laboratory that soil deposits build by nature over thousands of years.

Unfortunately, extreme events like the 2018 Hokkaido Eastern Iburi Earthquake happen. It would be even more unfortunate if the engineering profession did not capture the perishable data that enables us to understand which design procedures result in good seismic performance and which procedures still need improvement. The GEER Association is structured to develop a systematic approach for conducting National Science Foundation (NSF) sponsored reconnaissance efforts so as to properly document these case histories.

Case History 1: A high density of regolith landslides occurred in the epicentral region. The slides are entirely in recent pumices and ashfall deposits mantling slopes in the region east of Mt. Tarumae, south of Shikotsu-ko Caldera lake. In some locations, landslide areal extent is in excess of 50% of the total land area. These landslides were typically a thin veneer of 1 to 3 m of recent pumice and ashfall material. The material is extremely low-density vesicular pumice that was wet and potentially saturated when the earthquake occurred. The slides traveled vertically 50-100 meters on slopes of approximately 25-35 degrees and ran out on flat rice fields for as much as 150 meters, indicating high velocity. The landslide morphology is flow failure, with no preservation of internal structure. The ash and pumice deposits on the slopes was deposited over four episodes of eruption from Tarumae ranging from 1739 to >5000BP.

Case History 2: A flow failure of soil collapse or liquefaction origin was observed in fill deposits placed in a residential community district of Kiyota ward in Sapporo. The community, Satozuka-1 is situated in a natural steep ravine that was filled with as much as 10 meters of pumice soil (Age ~40,000 ybp) in order to level the construction area. A flow failure occurred in this neighborhood that allowed for lateral migration of soil from the upper slope regions of the community onto the ground surface of the lower community. The upper community topographically deflated as large quantities of fluidized soil flooded the lower streets. Vertical subsidence associated with material loss in the upper neighborhood due to flow-failure extended 230m to 240m along the length of the affected area, with differential vertical settlements up to 2.2m. Remnant deposits in the topographically lower extent of the neighborhood from the flow-failure was found in the streets and beneath vehicles were a very light, porous, non-plastic pumice sand of fairly uniform size. At the time of our reconnaissance we were not able to fully observe the extent of the deposits as considerable remediation of the site had already occurred. Liquefaction and subsequent flow sliding occurred at Satozuka within a deposit of pumice fill placed during the 1980s.

Case History 3: Deep seated landslides: PG&E-SCE-InfraTerra team observed two deeper landslides that damaged electric transmission towers north of the epicenter. Both of these deep-seated, translational landslides occurred within bedrock and exhibited typical features for sliding failures along a discrete weak layer, including well-defined headscarps and sidescarps, and translated blocks with varying degrees of internal deformation. Interpretation of aerial imagery from before the earthquake

and post-earthquake field observations document geomorphic evidence of pre-existing failure, including incipient headscarp grabens. For the Horonai Mega Block Glide, a 900 meters long by 200-300 meters wide mass slid 350 meters south-southwest, blocking a west-northwest trending stream valley. This failure represents a partial failure of a larger pre-existing slide, which is bounded by similar large pre-existing slides that did not experience significant movement during the Hokkaido earthquake. This suggests a long history of deep-seated landsliding potentially concurrent with past large earthquakes.

Acknowledgments

The GEER reconnaissance was led Robert Kayen (United States Geological Survey & University of California, Berkeley) and included team members Atsushi Mikami (Tokai University) Donald Anderson (Brigham Young University), Alex Grant (US Geological Survey), and Brad Wham (University of Colorado Boulder). Paolo Zimmaro (University of California, Los Angeles [UCLA]), Pengfei Wang (UCLA), and Yi Tyan Tsai (UCLA) participated on the reconnaissance data processing remotely from the US. The team appreciates the support of the GEER Steering Committee. A second reconnaissance lead by the Pacific Gas & Electric Company (PG&E) visited a central area in October, 2018. The second reconnaissance was focused on the electrical utility grid and several large landslides in marine sedimentary deposits beneath the extensive landslides found pumice soil.

The authors of this report would like to thank the Sapporo Department of Water Works and colleagues at Kubota Corporation for providing valuable guidance and information before, during, and after the reconnaissance mission.

The work of the GEER Association is based upon work supported in part by the National Foundation through the Geotechnical Engineering Program under Grant No. CMMI-1266418. The GEER Association is made possible by the vision and support of the NSF Geotechnical Engineering Program Directors: Dr. Richard Fragaszy and the late Dr. Cliff Astill. GEER members also donate their time, talent, and resources to collect time-sensitive field observations of the effects of extreme events. Any opinions, findings, and conclusions or recommendations expressed in this material are those of the authors and do not necessarily reflect the views of the NSF.

1.0 Introduction

The 2018 Hokkaido Eastern Iburi M_W6.6 earthquake struck the southern coast of the north island of Japan in the early morning (3:08 AM JST) on September 6, 2018. The event had a hypocentral depth of 35 km, centered beneath the port city of Tomakomai. Extremely strong shaking with peak ground acceleration in excess of 0.5 g was felt in the communities directly north of Tomakomai, in the districts of Abira and Atsuma. There, a very high density of landslides occurred in pumices soil that affected the majority of slopes in the region above the floodplain. These landslides were typically a thin veneer of 1 to 3 m of recent (<9000 ybp) volcanic pumice mantling older marine sedimentary rocks. The source of the pumice layers are recent eruptions from Mt. Tarumae, south of Shikotsu-ko Caldera lake.

A flow failure of soil collapse or liquefaction origin was observed in fill deposits placed in a residential community district of Kiyota ward in Sapporo. The community, Satozuka-1 is situated on a natural steep ravine that was filled with pumice soil to level construction area to a gently sloping landscape for housing construction. The flow failure consisted of lateral migration of soil from the upper slope regions of the community onto the surface of the lower community. The upper community topographically deflated as large quantities of fluidized soil flooded the lower streets.

The motivation for organizing and fielding the Hokkaido Iburi event GEER reconnaissance rapidly was to document engineering and scientific effects of these unusual features that produced a remarkably high density of surficial landslides in ashfall and pumice deposits. The GEER Hokkaido field team's main goal is to quantify the spatial extent and characteristics of geotechnical failures and non-failures. It is important to document poor ground performance, but also good performance of ground in the epicentral region. Due to the necessary follow-on recovery and reconstruction activities, much of the critically important observable damage is perishable. Toward that end, GEER fielded a team within two weeks after the event, and soon after the initial humanitarian response phase had ended. The primary duties of the Hokkaido GEER reconnaissance team are to identify critical case histories, report our findings rapidly on the GEER website through PDFs, web pages, Google Earth kml files, and animations of UAV and LIDAR data. Experienced participants also have the responsibility to train new participants in the key-elements of reconnaissance fieldwork.

The authors conducted the GEER reconnaissance survey from September 27th to October 3rd. GPS tracklogs of the movement of the reconnaissance team were recorded and are presented in Figure 1-1. The team worked from two vehicles. Dr. Brad Wham met with engineers from Sapporo City Waterworks and Sewage Bureau Deputy to discuss overall performance of lifelines during the Hokkaido earthquake series. This report summarizes the observations of the GEER team, as well as the PG&E team that visited additional electrical power associated sites on late October. These included several hydropower dams, the Denryoku Tomahigashi Atsuma Coal Power Station in east Tomakomai, and damaged transmission towers founded on large deep-seated landslides.

Table 1-1. Overview of GEER team activities during the reconnaissance

GEER Member	Sept-27	Sept-28	Sept-29	Sept-30	Oct-1	Oct-2	Oct-3
Kayen	Scouting of target sites, UAV flights near Atsuma	UAV of Yoshino and dam landslides	UAV flights of Port and adjacent facilities, …	UAV flights of Rt 59 Slides and adjacent Flows, Rt 1065 Slides	Debrief w/ team, travel	-	-
Grant	Travel	Lidar scans of Yoshino and dam landslides, initial lidar of Satozuka	Lidar scans of Port liquefaction, Rt 59 slides w/Wham	Recon of structural damage in Atsuma, landslides along Rt 1065	Post Typhoon + aftershock recon (Abira), continued scans of Satozuka	Extensive scanning of Satozuka, UAV flights of Cow slide and WTP	Debrief w/ team, travel
Wham	Travel	cf. Grant	w/ Kayen for Port liq. Recon, led eastern recon of landslide extents	cf. Grant	Meeting with Sapporo Water, pipeline recon	Meeting with Atsuma Water, recon of WTP	Ibid.
Anderson	Travel	cf. Kayen	BLK lidar scans of Port liquefaction, w/Kayen in afternoon	cf. Kayen	w/ Grant and Wham	w/ Grant and Wham, Building tag survey	Ibid.
Mikami	Travel	cf. Grant	cf. Wham	cf. Grant	Travel	-	-

PG&E Member	20-Oct	21-Oct	22-Oct	23-Oct	24-Oct	25-Oct	26-Oct
Jeff Bachhuber - PG&E	Arrival/Trip Planning	Atsuma, Horonai, Atsuma Dam	Hobetsuizumi Landslide Evaluation	Coal Plant, Horonai Mega Block Glide	Nibutani & Hobetsu Dams, Sapporo liquefaction	Mega slide and Mizuho Dam	Departure
Joseph Sun - PG&E	Arrival/Trip Planning	Atsuma, Horonai, Atsuma Dam	Hobetsuizumi Landslide Evaluation	Denryoku Tomahigashi Atsuma Coal Power Station Liquefaction, Horonai Mega Block Glide	Nibutani Dam, Hobetsu Dam, Sapporo Liquefaction	Horonai Mega Block Glide, Mizuho Dam, Highway shallow slides	Departure
Chris Madugo - PG&E	Arrival/Trip Planning	Atsuma, Horonai, Atsuma Dam	Hobetsuizumi Landslide [Drone Survey]	Denryoku Tomahigashi Atsuma Coal Power Station Liquefaction, Horonai Mega Block Glide [Drone Survey]	Nibutani Dam, Hobetsu Dam, Sapporo Liquefaction	Horonai Mega Block Glide, Mizuho Dam, Highway shallow slides [Drone Survey]	Departure

Matthew Mutto - SCE	Arrival/Trip Planning	Atsuma, Horonai, Atsuma Dam	Hobetsuizumi Landslide Evaluation	Denryoku Tomahigashi Atsuma Coal Power Station Liquefaction, Horonai Mega Block Glide	Nibutani Dam, Hobetsu Dam, Sapporo Liquefaction	Horonai Mega Block Glide, Mizuho Dam, Highway shallow slides	Departure
Esam Abraham - SCE	Arrival/Trip Planning	Atsuma, Horonai, Atsuma Dam	Hobetsuizumi Landslide Evaluation	Denryoku Tomahigashi Atsuma Coal Power Station Liquefaction, Horonai Mega Block Glide	Nibutani Dam, Hobetsu Dam, Sapporo Liquefaction	Horonai Mega Block Glide, Mizuho Dam, Highway shallow slides	Departure
Chris Hitchcock - Infraterra	Arrival/Trip Planning	Atsuma, Horonai, Atsuma Dam	Hobetsuizumi Landslide [Drone Survey]	Denryoku Tomahigashi Atsuma Coal Power Station Liquefaction [Drone Survey], Horonai Mega Block Glide [Drone Survey]	Nibutani Dam, Hobetsu Dam, Sapporo Liquefaction	Horonai Mega Block Glide, Mizuho Dam [Drone Survey], Highway shallow slides	Departure
Koji Okumura - Hiroshima Univ.	Arrival/Trip Planning	Atsuma, Horonai, Atsuma Dam	Hobetsuizumi Landslide Evaluation	Denryoku Tomahigashi Atsuma Coal Power Station Liquefaction, Horonai Mega Block Glide	Nibutani Dam, Hobetsu Dam, Sapporo Liquefaction, Departure		

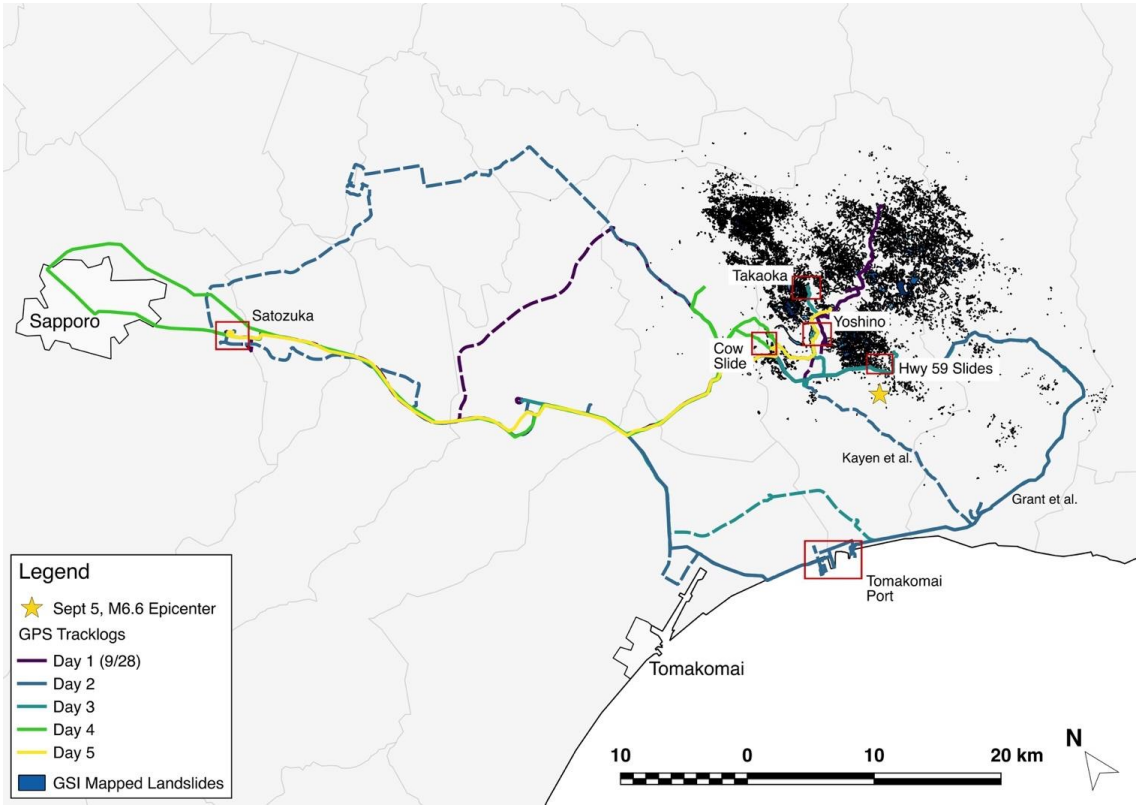

Figure 1-1. Tracklog of GEER team movements in the Hokkaido region in Japan.

2.0 Typhoon No. 21 (Jebi) Gebi

2.1 Introduction

This earthquake was preceded by a large amount of rainfall in the month of August, and the arrival of typhoon Gebi in the days prior to the event. The strong correlation between slope failure and rainfall is a topic of research interest, and this chapter provides an initial assessment of the precipitation in the epicentral-region before the earthquake.

Typhoon No. 21 Gebi was the twenty-first atmospheric event to strike the western Pacific in 2018. This typhoon caused great damage in coastal area of western Japan, and has been compared with the disastrous Typhoon Vera of 1959 that caused more than 5,000 fatalities. For example, the typhoon resulted in 3.7 meters of flooding of Kansai airport, (Osaka regional headquarters, JMA).

2.2 Trajectory Of Typhoons

The trajectory of Typhoon No. 21 Gebi is shown in Figure 2.1a. The typhoon crossed Japan in the Kansai region and moved up the Japan Sea side of the archipelago, passing the west coast of Hokkaido the day before the earthquake. As Gebi approached Hokkaido, the wind speed diminished. The maximum wind speed in the epicentral area at Atsuma was 34.3 m/s (77 miles/hour) from the south-east direction. Other typhoons that approached Hokkaido after July, 2018 are also shown in Figure 2.1a.

2.3 Precipitation

The daily precipitation at Atsuma from July to September, 2018 is shown in Figure 2.2a,b,c. Rainfall accumulation at Atsuma during the one-month period of August 6 to September 5 reached 225mm[3]. The heavy rainfall in mid-August was caused by a stationary storm front over Hokkaido[4].

Figure 2.3a,b,c shows daily precipitation in Sapporo from July to September. Rainfall accumulation during the one-month period of August 6 to September 5 registered 269mm[3]. Figure 2.4 compares monthly precipitation records at Atsuma for the last six years (2013-2018). The heaviest rainfall occurred during the summers of 2016 and 2018. This is shown as well in Figure 2.5, which shows annual rainfall for the last ten years. Precipitation in 2018 up to September 5 was 881.5mm, which was nearly equal to the average annual rainfall over an entire January-December period (1010.5mm[3]).

The 24-hour and 48-hour antecedent rainfall (Sept 5 local time; M6.6 mainshock occurred at 3:08am Sept. 6) in the region of the most intense landslide triggering ranged from 11 to 21mm (Figures 2.6, 2.7). Sapporo and the hills north of the Shikotsu-ko Caldera lake recorded 24-hour rainfall associated with Typhoon Gebi of 29 to 85mm.

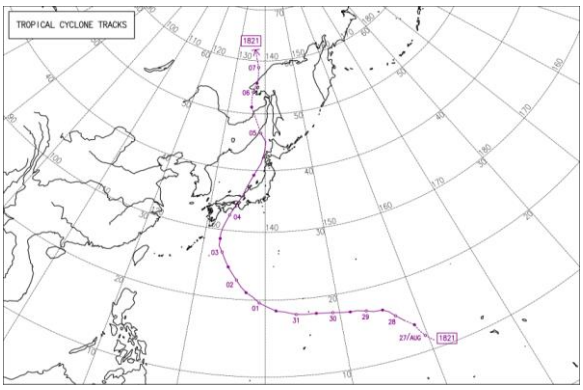

(a) No. 21 Gebi

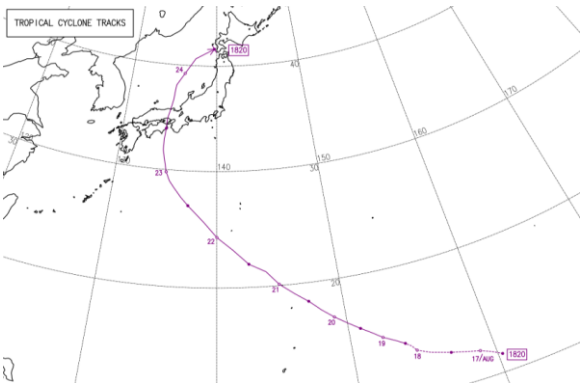

(b) No. 20

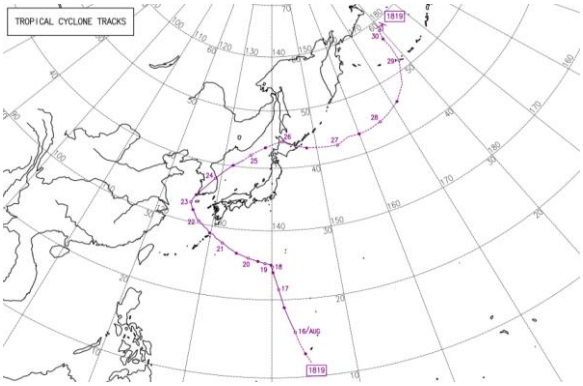

(c) No. 19

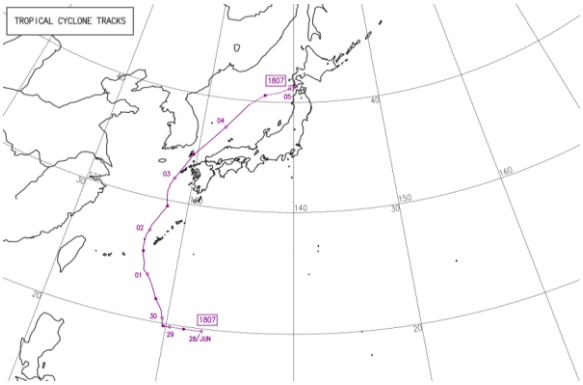

(d) No. 7

Figure 2-1. Trajectory of typhoon No. 21 Gebi (a) and other typhoons that approached Hokkaido after July 2, 2018. Source: Japan Meteorological Agency (JMA; 2019a)

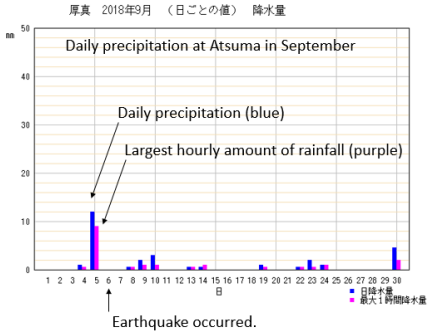

(a) September, 2018

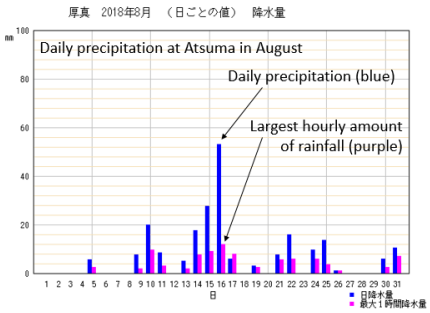

(b) August, 2018

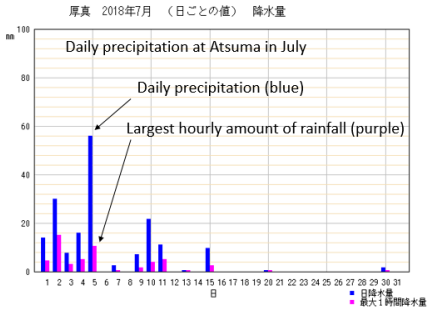

(c) July, 2018

Figure 2-2. Precipitation at Atsuma. Source: Japan Meteorological Agency (2019b)

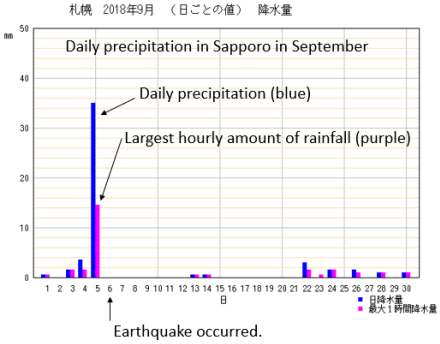

(a) September, 2018

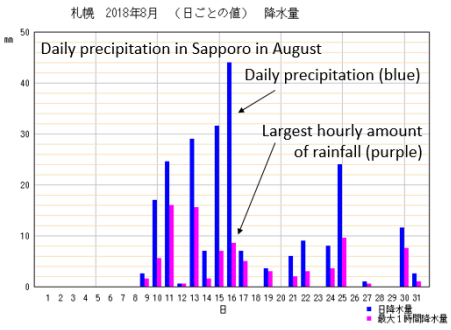

(c) August, 2018

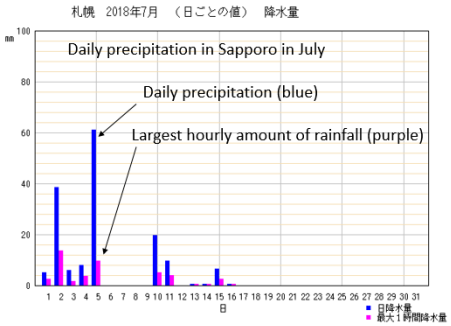

(c) July, 2018

Figure 2-3. Precipitation at Sapporo. Source: Japan Meteorological Agency (2019b)

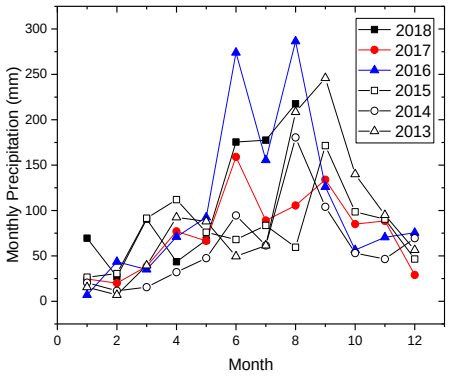

Figure 2-4. Graph showing monthly precipitation at Atsuma, 2013-2018.

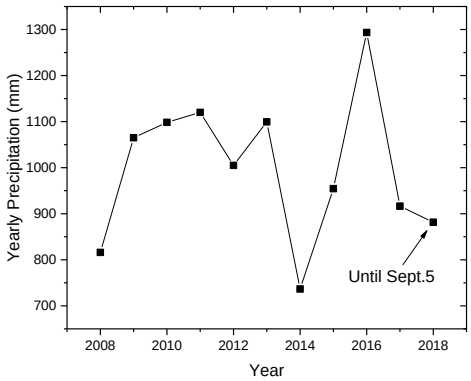

Figure 2-5. Graph showing yearly precipitation at Atsuma, 2008-2018.

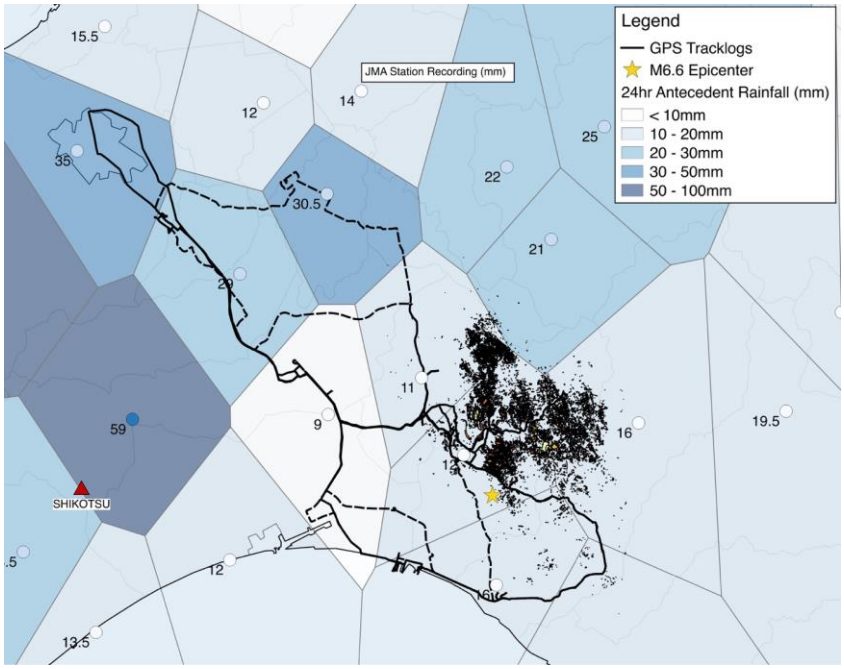

Figure 2-6. 24-hr rainfall totals for Sept 5, 2018 (local time) in mm. Black polygons show locations of mapped landslides by GSI.

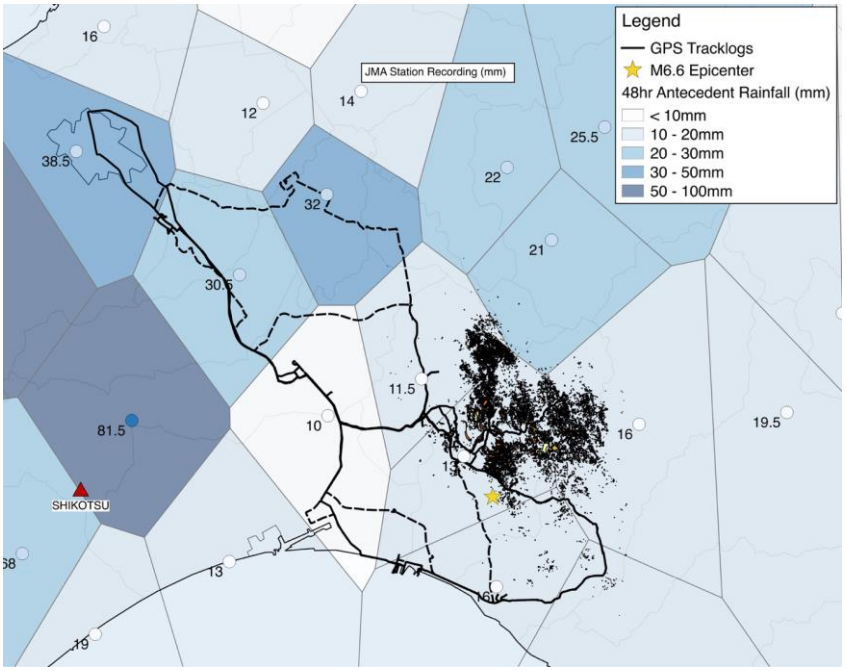

Figure 2-7. 48-hr rainfall totals for Sept. 4 – 5, 2018 (local time) in mm.

3.0 Hokkaido Eastern Iburi Earthquake Tectonic Setting, Regional Geology

3.1 Framework Geology

The Island of Hokkaido is a composite structure of several distinct orogens brought into contact via the southward migration of the Okhotsk plate and development of the Hidaka Collision Zone below SE Hokkaido. Running west to east, modern Hokkaido is shaped by Miocene age primarily submarine volcanism, the low-lying Yufutsu basin—home to Sapporo, Chitose, and Tomakomai—and then east to the Hidaka Collision where a sequence of Himalayan Orogeny plutons and metamorphism shape the core of the landscape of the eastern highlands (Fig. 3.1; Isomi, 1965; Geologic Survey of Japan (GSJ) 1967; Okada, 1982)

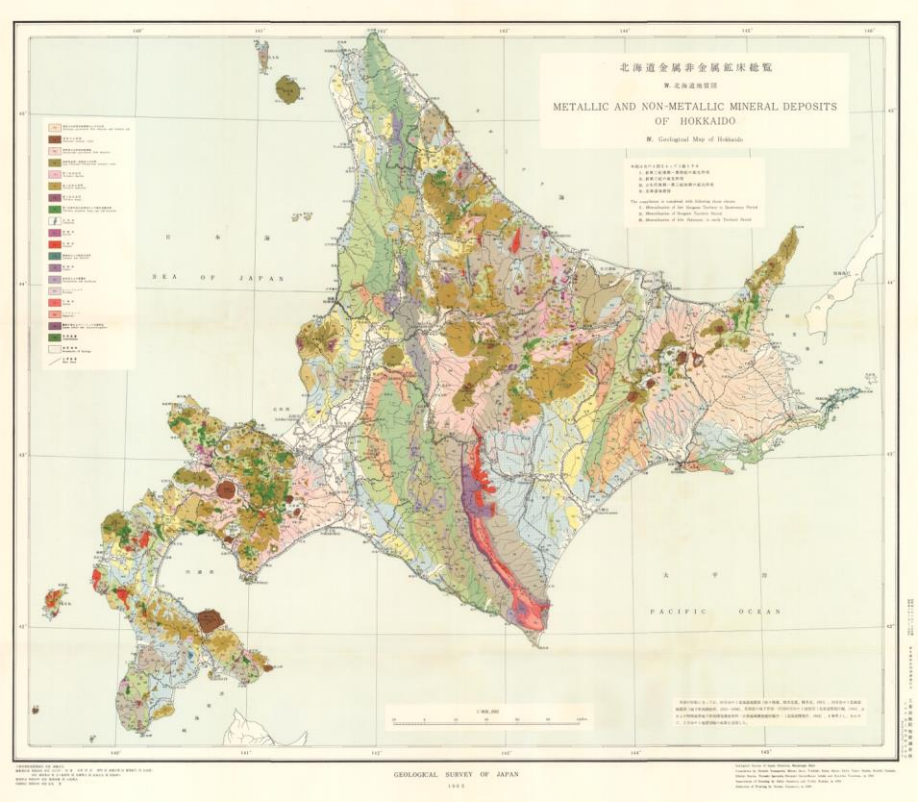

Figure 3-1. 1:800,000 scale geologic map of Hokkaido by the Geologic Survey of Japan (1967). Earthquake effects, and reconnaissance were focused in the constriction of midwestern Hokkaido near Sapporo and Chitose, primarily in late Pleistocene to Holocene volcanic or alluvial soils and Miocene age sedimentary units (primarily sand and mudstone), light blue and green in the above along the southern sections of the 142° Meridian.

Running approximately north-south along the lowland corridor between Sapporo and Tomakomai is the Yufustu basin, a deep structural basin dividing Hokkaido where depths to basement shear wave velocities of 2.5km/s are in excess of 3km, and in the region of the GEER reconnaissance depth to basement ranges from 6 – 8km (Marafi et al., 2017). Focusing of seismic waves along the Yufutsu basin may be partially responsible for the observed distribution of strong shaking NNW of the earthquake source and may have contributed to the widespread liquefaction observed 50km from the epicenter in Southern Sapporo (Satosuka).

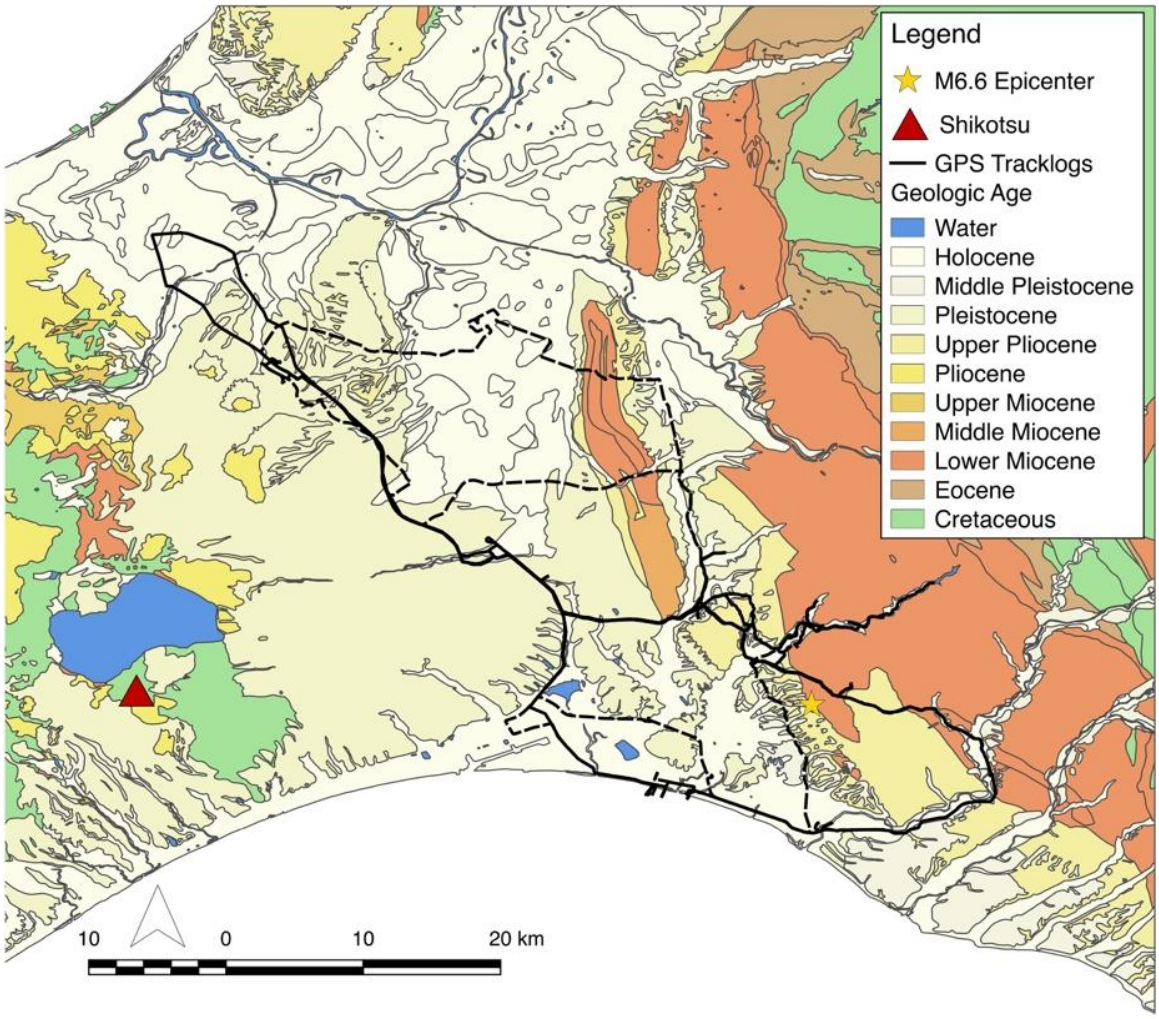

Figure 3-2. Simplified geologic ages (from 1:200,000 scale mapping, GSJ) within the reconnaissance study region, GPS tracklogs of the reconnaissance teams shown in black lines. Surficial deposits are primarily Miocene or Pleistocene in age, including extensive Shikotsu-1 pumice and scoria deposits (Pleistocene).

Within the midwestern lowland and foothills regions of Hokkaido the principal units explored as part of the GEER reconnaissance were a sequence of Miocene age sand- and mudstones, locally the Kawabata and Oiwake formations (Fig. 3-2). The Oiwake formation is an Uppermost Miocene mudstone, sandstone, and conglomerate (Ishida et al., 1980) found in the southern and eastern

margins of observed landslides in our reconnaissance. Exposure was only observed in one location along Hwy 59 as heavily weathered and fractured mudstone. Most observed landslides were within the Kawabata formation, Lower Miocene conglomerate, sandstone, and mudstone. In our reconnaissance the Kawabata was observed only where exposed by shallow landslides near Horonai. Subsequent reconnaissance by Pacific Gas and Electric found large exposures of the Kawabata sandstone and mudstone within a deep-seated landslide (Fig. 3-3), reporting the unit to be a sequence of turbidite sandstone and interbedded mudstone.

Figure 3-3. Exposure of the Kawabata formation within a deep-seated translational rock slide, image from Jeff Bachhuber 42.736835°, 142.005206.

Superimposed on these large-scale geologic structures is the active volcanism of Hokkaido. 18 Holocene-active volcanoes are located within the island of Hokkaido, eight of which have historic eruptions (Smithsonian Global Volcanism Program, 1995). Within the reconnaissance mission area, pumice deposits from a series of eruptions from the Shikotsu Calera to the west mantle the landscape in up to several meters of pumice and derivative volcanic soils (Figs 3.4-5, Table 3-1; Ishii, 1963; Minato et al., 1972; Arai et al., 1986; Yanagida, 1994; Machida, 1999).

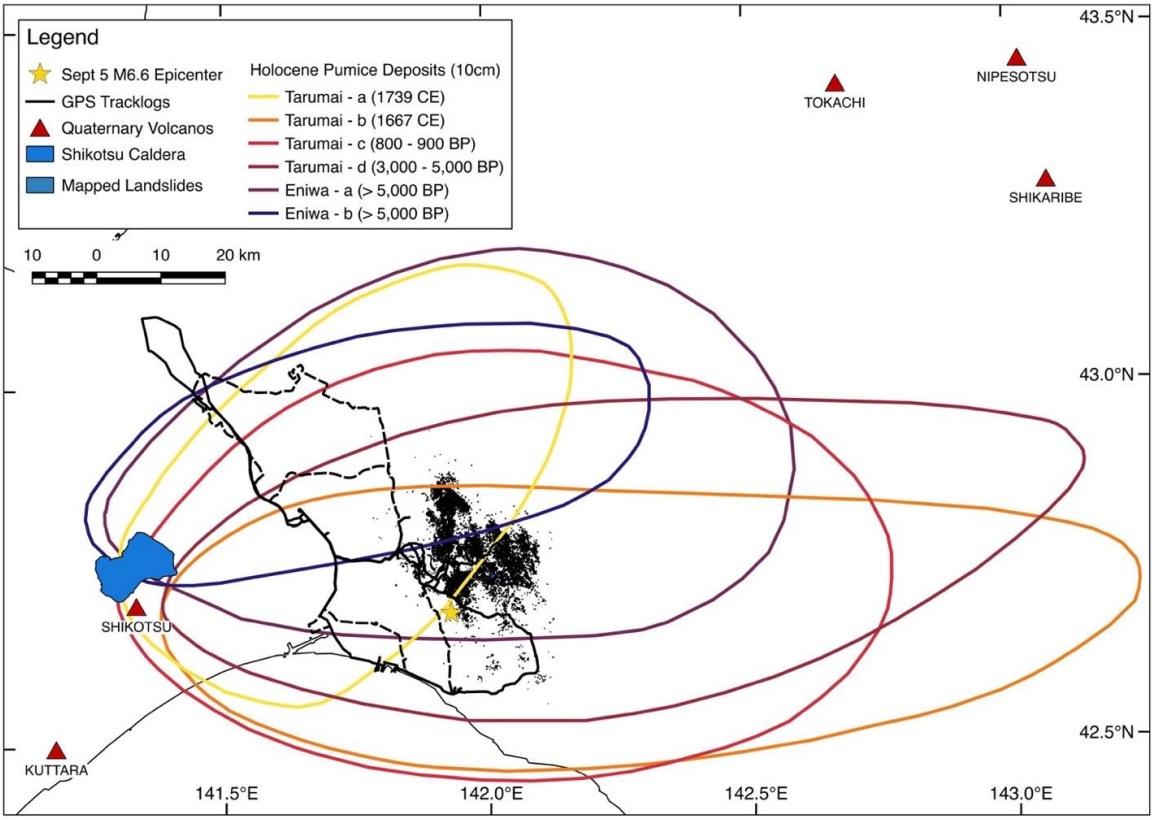

Figure 3-4. Pumice-fall contours (10cm) of significant eruptions of the Shikotsu volcano. All triggered landslides are within the 100cm deposition of Shitoksu pumice (20 - 40ka). Mapped from Ishii (1963).

Table 3-1. Summary of major Holocene and late Pleistocene Shikotsu Caldera eruptions from Ishii (1963). Right, cartoon after Ishii (1963) showing the stratigraphy of pyroclastic deposits at Hayakita on the western edge of observed landslides triggered by the Sept 5 earthquake.

Deposit		**Index**	**Age**	**Approx. Thickness at Hayakita (cm)**
Holocene	Tarumai a	Ta-a	1739 CE	5
	Tarumai b	Ta-b	1667 CE	20
	Tarumai c	Ta-c	800 – 900 BP	25
	Tarumai d	Ta-d	3,000 – 5,000 BP	90
	Eniwa a	En-a	> 5,000 BP	60
	Eniwa b	En-b	> 5,000 BP	40
Pleistocene	Shikotsu 1		20 – 40 ka	>100

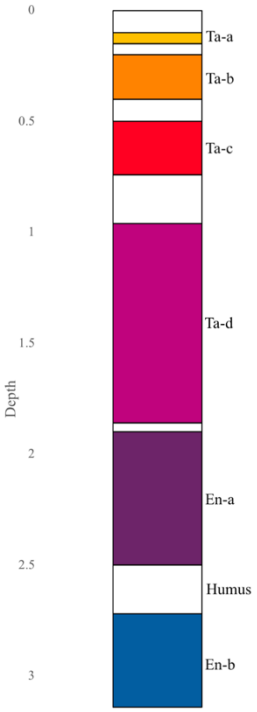

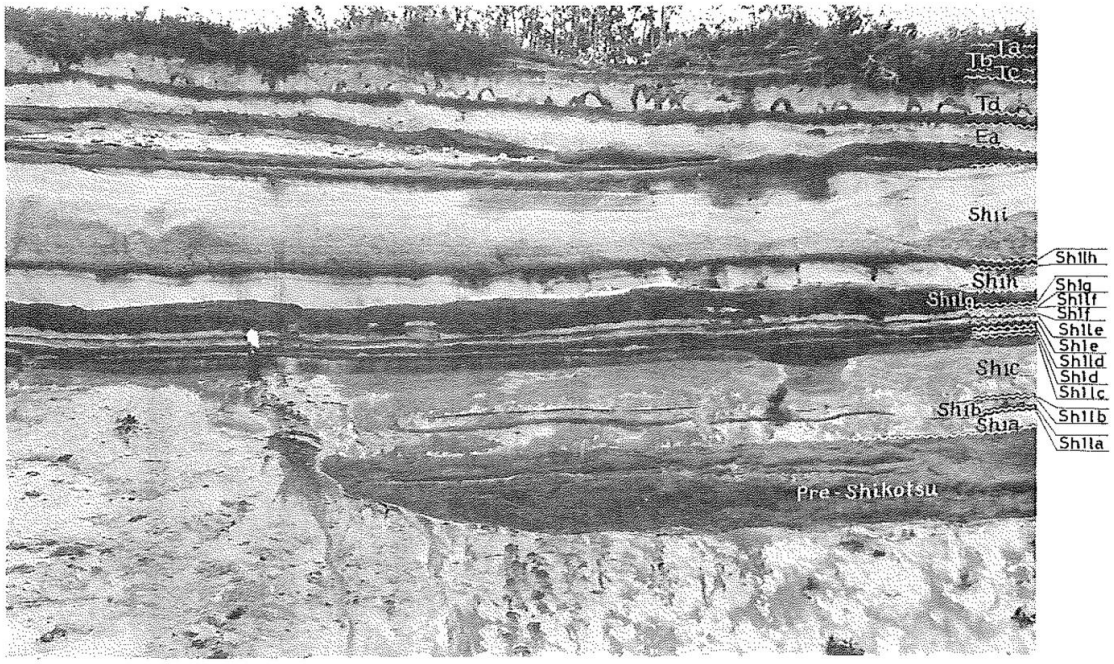

Figure 3-5. Hayakita pyroclastic type section from Minato et al. (1972). Note person for scale in left-center of image. During reconnaissance only the top 1 – 2m of pyroclastic deposits were observed, locally less than 1m resting directly on bedrock (often slopes >20°).

3.2 Regional Tectonics

Hokkaido is located on the Okhotsk microplate between the twin subduction zones of the Pacific Plate along the Japan-Kuril trench to the west and incipient subduction of the Amuria Plate in the Japan Sea to the east. Westward-oblique subduction of the Pacific Plate along the Kuril arc resulted in the Hidaka collision zone in central Hokkaido (Taira, 2001, Fig. 3-6). Active faults within Hokkaido are primarily associated with the Hidaka collision zone and in the NE where N-S trending reverse faulting associated with the E-W compression of the island have developed (Taira, 2001).

As in much of Japan, Hokkaido, particularly southwestern portions of the island adjacent to the Kuril trench and Hidaka collision zone, is highly seismically active. Since 1940, 18 earthquakes of M7.0 or greater have been recorded in the around Hokkaido (Fig. 3-7), including the 1952 M8.1 and 2003 M8.3 subduction zone earthquakes off of Cape Erimo in the south-central portion of the Island. In the last ten years (Oct 2008 – Oct 2018) 92 M5.0 or greater earthquakes have been recorded around Hokkaido.

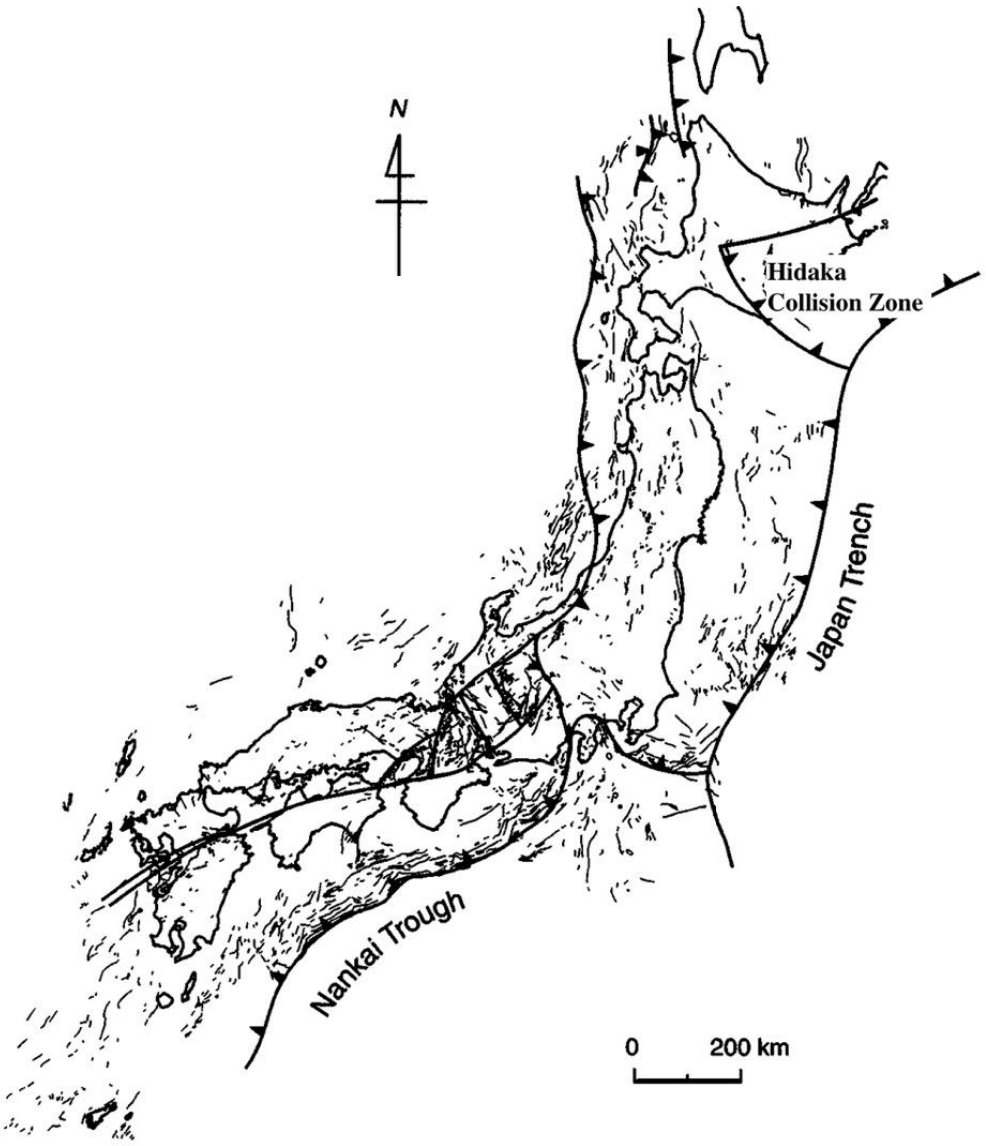

Figure 3-6. Plate boundaries and quaternary faults of Japan. Modified from Taira (2001).

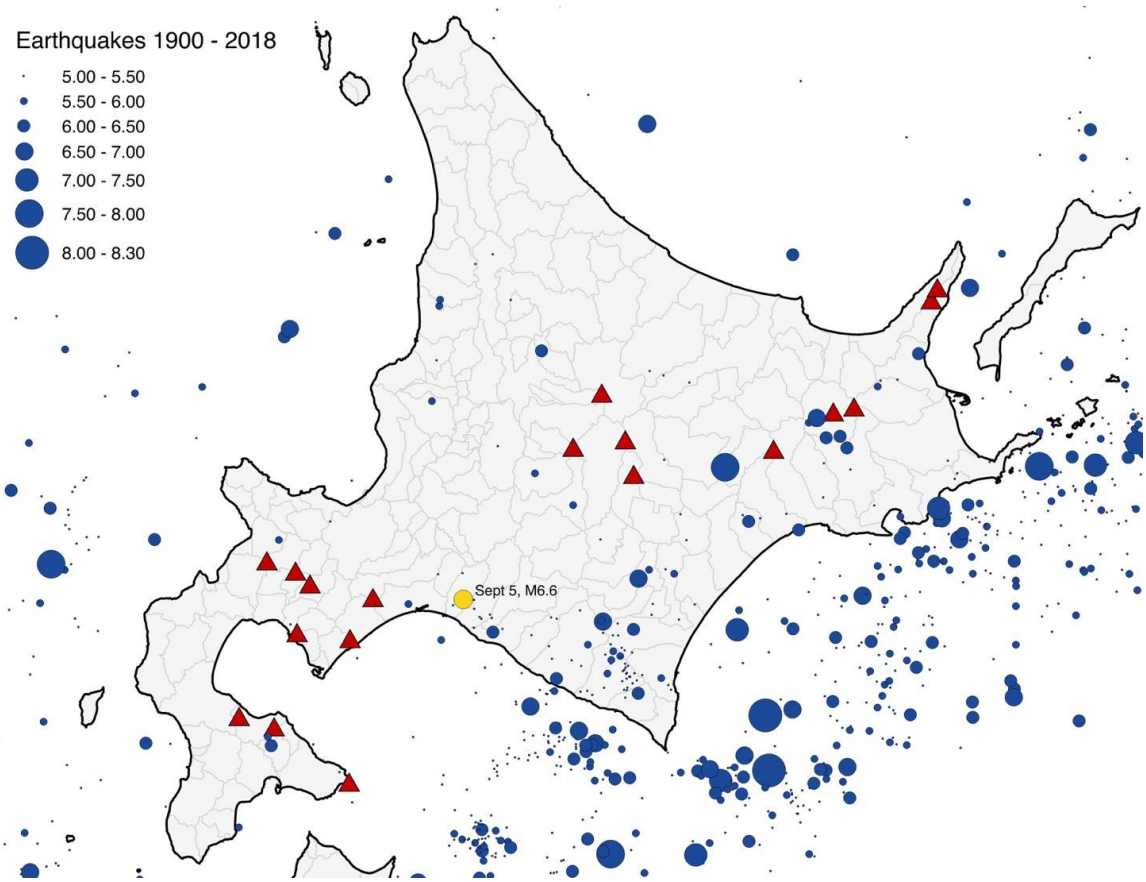

Figure 3-7. Seismicity of the Hokkaido region (M5+) since 1900 available from ANSS ComCat via the USGS interactive catalog search tool (https://earthquake.usgs.gov/earthquakes/search/). Major volcanos on Hokkaido Island shown as red triangles.

3.3 The Sept 5, 2018 Earthquake Sequence

The M6.6 Tomakomai earthquake occurred at 18:07:59 UTC on September 5th, 2018 [3:07am Sept. 6 local time], epicentral location: 42.686°N 141.929°E. The USGS-NEIC moment tensor solution suggests a fault source striking 333° dipping NE 61°. Geospatial Information Authority of Japan (GSI) InSAR analyses suggest a more northerly 358° strike with a steeper 74° eastward dipping source (Fig. 3-8). Hypocentral depth was estimated as 35km (USGS) – 37km (JMA), with a depth to top of faulting of 16km (GSI).

The Sept 5 mainshock was followed by an aftershock sequence that continued to generate strong shaking throughout the month of September (Fig. 3-9). Aftershocks propagated bilaterally N-S from the mainshock source. During our GEER-reconnaissance M5.0 and M4.8 aftershocks were felt, and appeared to result in renewed roadway damages (cracking, differential settlement), but no new landslides.

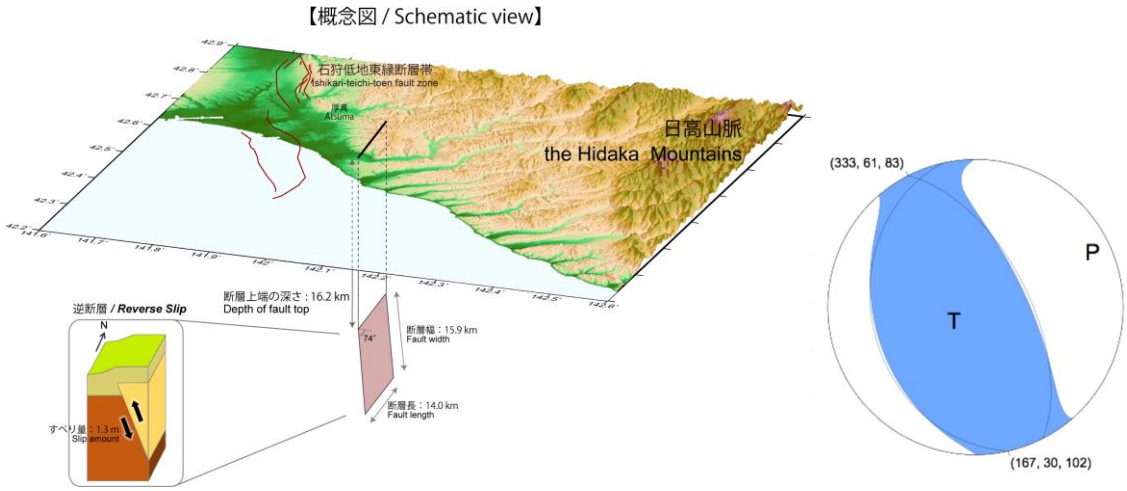

Figure 3-8. Source solutions for the M6.6 Sept 5, Tomakomai earthquake. Left, GSI fault plane solution from InSAR analyses. Right, USGS-NEIC moment tensor solution.

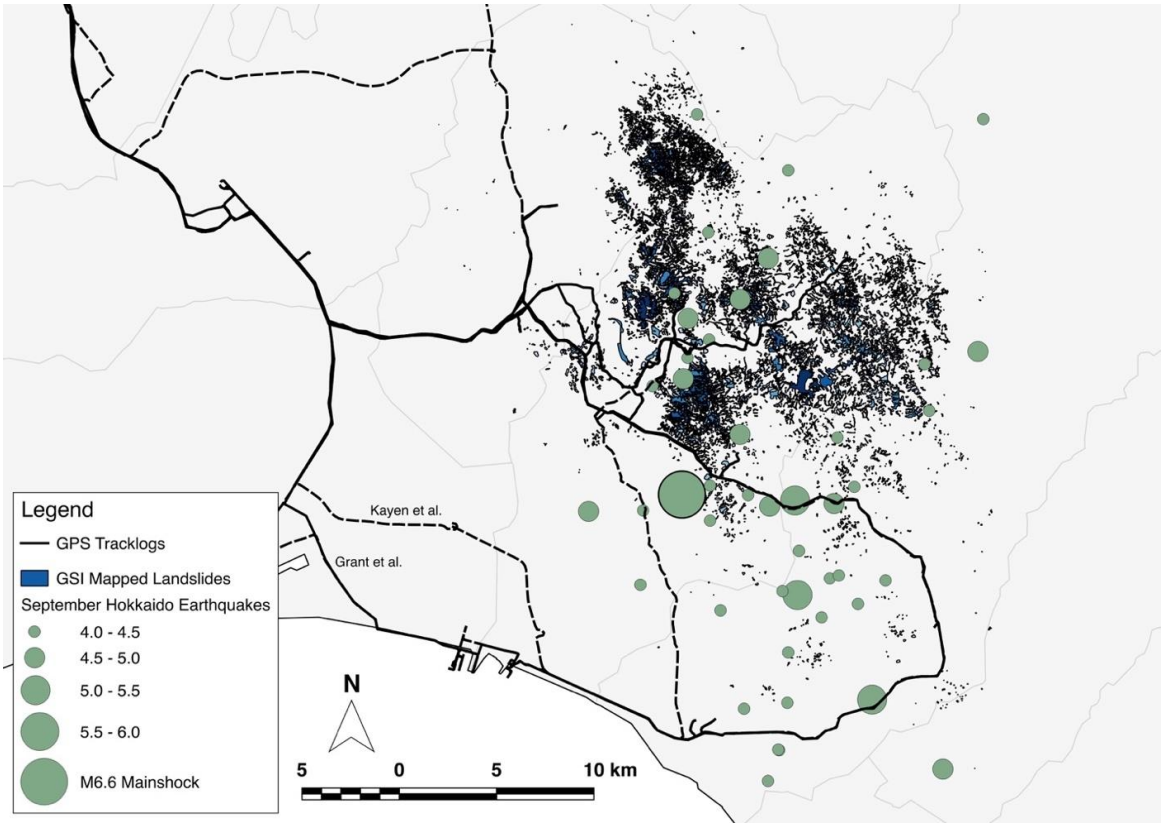

Figure 3-9. The September 2018 Hokkaido, Japan earthquake sequence with triggered landslides (blue polygons) and reconnaissance tracks (black lines).

4.0 Ground Motions

4.1 Available Recordings And Site Conditions

In this section we analyzed ground motion recordings of the M_W 6.6 Hokkaido Eastern Iburi mainshock. We obtained raw unprocessed ground motion recordings from the K-NET and KiK-net networks (http://www.kyoshin.bosai.go.jp/) and processed them using standard NGA protocols as implemented in the RCTC package by Wang et al. (2017). This processing consisted of applying high-pass acausal Butterworth filters in the frequency domain. Corner frequencies are then selected by visually inspecting the Fourier amplitude spectra and then testing the influence of alternate corner frequencies on displacement time series. The lowest corner frequency producing displacement time series having relevant appearance was selected. In this approach, the filtering process was combined with a baseline correction as needed (i.e. when filtering alone does not remove non-physical trends in the displacement time series). Ground motion intensity measure values used in this chapter are median component intensity measures (RotD50), computed from the processed time series (Boore 2010).

Our ground motion database contains ground motions recorded in a 200km radius from the epicenter and comprises recordings from 205 stations. Table A1 (available in the Appendix of this report) shows main characteristics of each recording including station locations, time-averaged shear wave velocity in the upper 30 m (V_{S30}) measured or inferred at station sites, source-to-site distances for all stations (i.e. rupture distance, R_{Rup} and Joyner and Boore distance, R_{JB}), and selected intensity measures including peak ground acceleration and velocity (PGA and PGV, respectively), and pseudo spectral acceleration values at various oscillator periods. In this report, lacking robust peer-reviewed finite fault models in the open literature, we utilize a model generated using the epicenter location, M_W, strike, dip, and rake as inputs, in combination with a global magnitude scaling relationship (Wells and Coppersmith, 1994) to calculate along-strike length and down-dip width. For 68 station sites, V_{S30} values are measured from profiles with maximum depth greater than 30m, for 136 sites V_{S30} values are derived from profiles with maximum depth smaller than 30m through V_{Sz}-to- V_{S30} relationships (where V_{Sz} is the time-averaged V_S to profile depth z), and one V_{S30} value is estimated using proxy-based relationships following procedure developed by the Next-Generation Attenuation (NGA) database project (Seyhan et al., 2014).

4.2 Ground Motion Characteristics In The Epicentral Area

In this section we analyze recordings from stations in the epicentral area. In our database, 31 stations are located at a Joyner and Boore distance R_{JB} = 50km or less. Among them, the IBUH01 (R_{JB}=13.5km, V_{S30}=306.8m/s), HKD127 (R_{JB}=13.5km, V_{S30}=221.6m/s), and HKD125 (R_{JB}=15.3km, V_{S30}=306.8m/s) recorded the highest PGA values: 1.12g, 0.97g, and 0.7g. Stations IBUH01 and HKD127 are located northwest of the epicenter in the updip direction of the causative fault (which roughly runs on a NS direction, dipping in the NE direction; strike = 333°, dip = 61°), while HKD125 is located northeast of the fault in the downdip direction of the fault. Figure 4-1 shows the spatial distribution of recording stations in the epicentral area, moment tensor of the event, and recorded PGA values (in units of g).

We analyze potential forward directivity effects for several recordings in the near-fault area. Rupture directivity effects are usually detected if long-period pulses are present in the horizontal direction normal to the strike of the fault (fault normal direction, FN; Somerville et al., 1997; Watson-Lamprey and Boore, 2007). Such polarization of shaking is not present in the fault parallel direction (FP). For earthquake generated by reverse fault mechanisms (such as the M_W 6.6 Hokkaido, Eastern Iburi earthquake), forward directivity effects are usually present in the updip direction. Stations HKD126,

HKD128, IBUH01, HDKH04, and HKD127 are the closest to the fault in the updip direction or in proximity of the corners of the fault. As a result, they would be the most likely to show rupture directivity effects. Figure 4-2 shows response spectra for the nine stations with R_{JB} < 20km. The FN component is higher than the FP and RotD50 components at long periods (i.e. T > 1s) for six stations: HKD126, HKD128, IBUH01, HKD127, and HDKH04 in the updip direction (or close to the fault corners) and HKD125 in the downdip direction.

The analysis of Figure 4-2, seems to indicate that for this earthquake, forward directivity effects are present. To further investigate such effect, we analyze all stations in the updip direction or in the close proximity of the fault corners, within a radius of 50km from the epicenter. We are especially interested in the ratio between the FN component and the median component intensity measures (RotD50) at long periods. If forward directivity effects are present, this ratio should be higher than one and its magnitude should increase as the period increases (Somerville et al., 1997). Figure 4-3 shows the ratio FN/RotD50 for spectral acceleration at T =1s, 2s, 3s, and 5s versus rupture distance. Also reported in Figure 4-3 are linear trends for each spectral acceleration value with distance. Figure 4-3 clearly shows a trend of decreasing FN/RotD50 with distance for all spectral accelerations. The ratio is higher at smaller distances for longer spectral accelerations. For larger distances, this ratio tends to have a horizontal asymptote at FN/RotD50=1. As a whole, the analyzed data seem to provide evidence of the presence of directivity effects. Such conclusion should be considered preliminary and further studies are needed to better comprehend its magnitude.

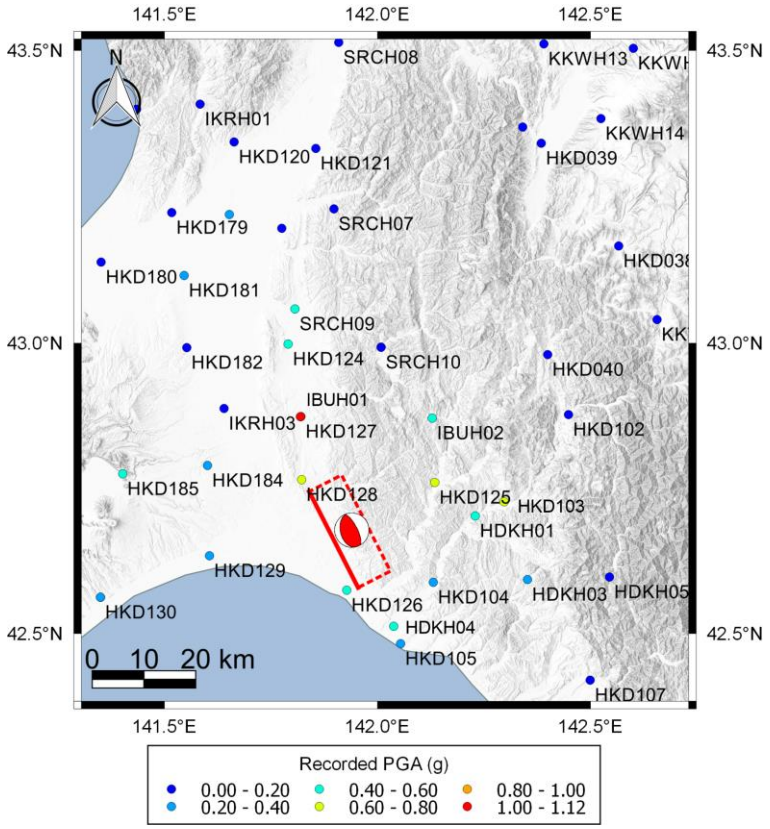

Figure 4-1. Overview of available recording stations in the epicentral area and recorded PGA.

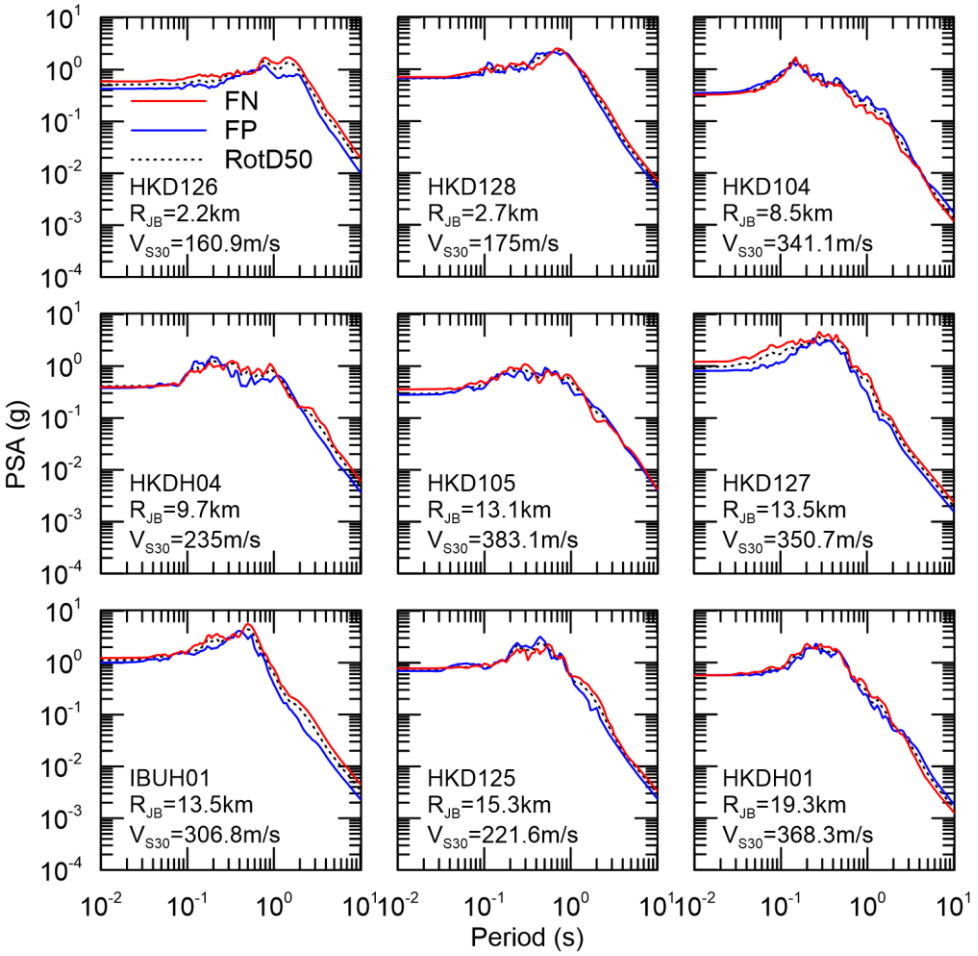

Figure 4-2. Response spectra (5% damping) for selected recording station in the epicentral area.

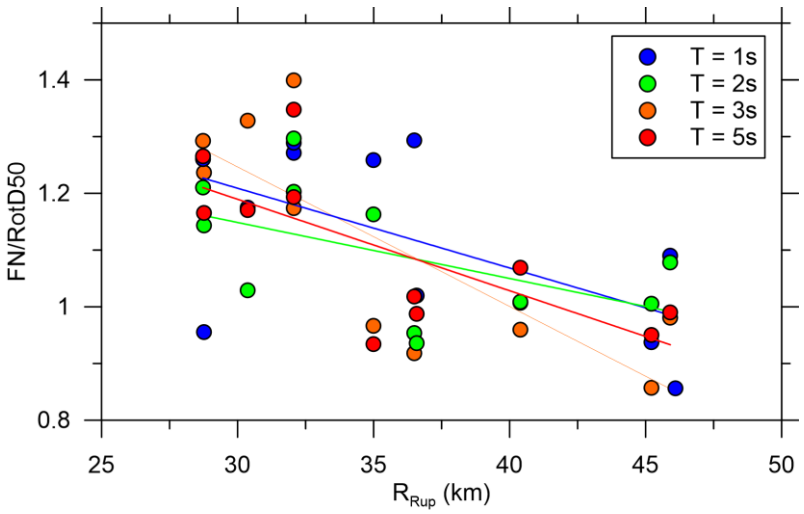

Figure 4-3. FN/RotD50 ratios versus rupture distance for stations in the updip direction for various periods (T = 1s, 2s, 3s, and 5s).

4.3 Comparisons To Global Ground Motion Models And Residuals Analysis

To visualize and better identify relevant features of the recorded ground motions from this event, in this section we perform comparisons between recorded data and predictions from ground motion models (GMMs). Our comparisons are performed against the Boore et al. (2014, hereafter BSSA14) model for shallow crustal earthquake without regional adjustment and with a regional adjustment for Japan. This adjustment is implemented in the model to capture an apparent faster anelastic attenuation with distance observed in data from Japan and Italy (showing similar trends).

Figure 4-4 shows median predictions for PGA and PGV from the global version of the BSSA14 model (labelled as BSSA14 global) and the BSSA14 model with regional adjustment for Japan (BSSA14 Japan), along with recorded data plotted with different symbols for three site categories: (1) soft soil (V_{S30} = 0 – 360 m/s), stiff soil (V_{S30} = 360 – 760 m/s) and rock (V_{S30} > 760ms). All model predictions have been made using a common V_{S30} = 350 m/s. This value represents an estimate of average site conditions in the epicentral area. The data shows an evident steep attenuation with distance for R_{JB} greater than 80-100km. Overall, this evident trend is captured by BSSA14 model with regional adjustments for Japan. Similar trends of fast anelastic attenuation with distance have been observed during recent events in Italy (e.g. Scasserra et al., 2009; Stewart et al., 2012; and Zimmaro et al., 2018).

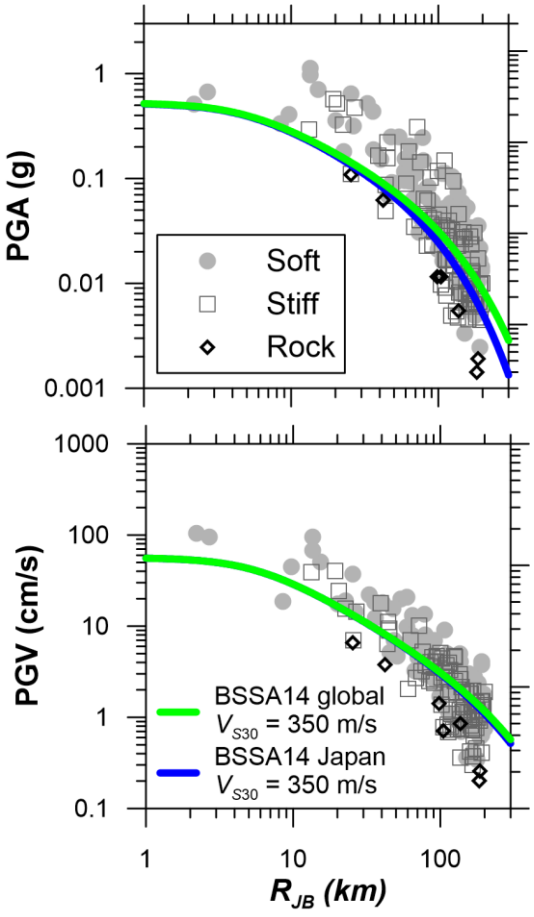

Figure 4-4. Variation of PGA and PGV with R_{JB} for rock, stiff, and soft soil.

To more clearly visualize the comparison between GMM estimations and recorded data, we perform residuals analysis. Total residuals (R_i) are calculated for each recorded PGA and PGV value as follows:

$$R_i = \ln(Y_i) - \mu_{ln}(\mathbf{M}, R_i, V_{S30,i}) \quad (1)$$

Where Y_i is the recorded intensity measure from recording i, and μ_{ln} is the prediction median for the same intensity measure (in natural-log units) as a function of model parameters (i.e. magnitude, **M**; distance, R; and V_{S30}). We then partition total residuals into three components (Stafford, 2012): (1) the random effect for each event η (commonly referred to as event term), (2) a bias term assumed to be equal to zero in the present analysis (c_k), and (3) the remaining residuals (within-event residual). Figures 4-5 and 4-6 show within-event residuals for PGA and PGV for the BSSA14 global model (Figures 4-5a and 4-6a) and for the BSSA14 model with regional adjustment for Japan (Figures 4-5b and 4-6b). Binned means and standard deviations are also shown in Figures 4-5 and 4-6. Remarkably, at larger distances (i.e. R_{JB} > 100km), the regionally-adjusted model performs better than the model without regional adjustment as expected.

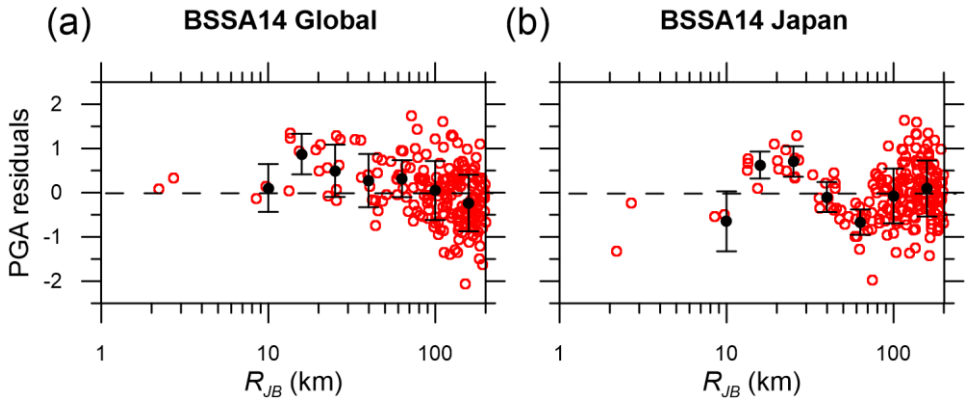

Figure 4-5. Within-event residuals of PGA from recorded ground motions relative to predictions of the (a) BSSA14 global model, and (b) the BSSA14 model with regional adjustment for Japan. Binned means shown with +/- one standard deviation.

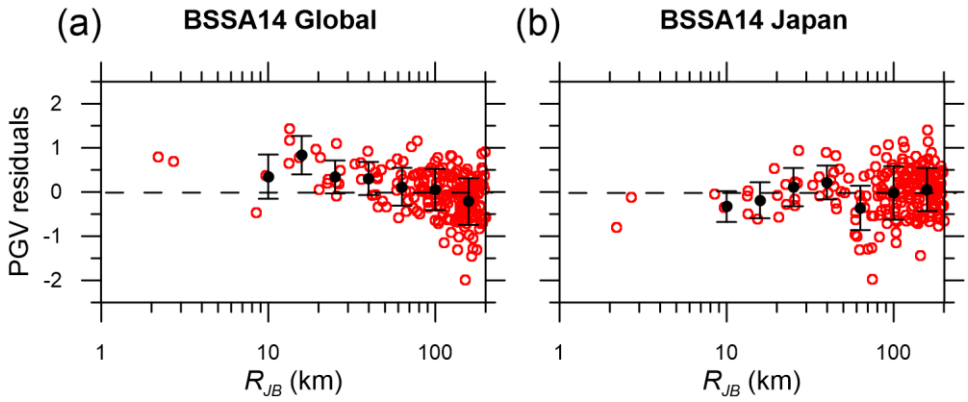

Figure 4-6. Within-event residuals of PGV from recorded ground motions relative to predictions of the (a) BSSA14 global model, and (b) the BSSA14 model with regional adjustment for Japan. Binned means shown with +/- one standard deviation.

Global recordings from subduction earthquakes typically show that sites located in the backarc region are characterized by a much steeper attenuation with distance than forearc sites (e.g. Abrahamson et al., 2016). This steeper attenuation with distance in the backarc region was also observed in recent subduction and shallow crustal earthquakes in Japan (e.g. Abrahamson et al., 2018 and Kishida et al., 2013, respectively). This feature is due to wave propagation effects and is likely related to the lengths of ray paths through forearc and backarc regions (Abrahamson et al., 2018). To analyze this feature, we perform residuals analysis separating stations in the backarc and in the forearc region.

Figures 4-7 and 4-8 show within-event residuals for PGA in the forearc and in the backarc regions. The residuals for the BSSA14 global model clearly show a steeper attenuation with distance for sites located in the backarc region (residuals trending downward for large distances). This effect disappears in the BSSA14 model with regional adjustment for Japan. Similar trends can be observed for PGV residuals shown in Figures 4-9 and 4-10. Our analysis shows that the overall attenuation of the ground motion for large distances is much faster for sites in the backarc. This effect is captured by the BSSA14 model with regional adjustment for Japan.

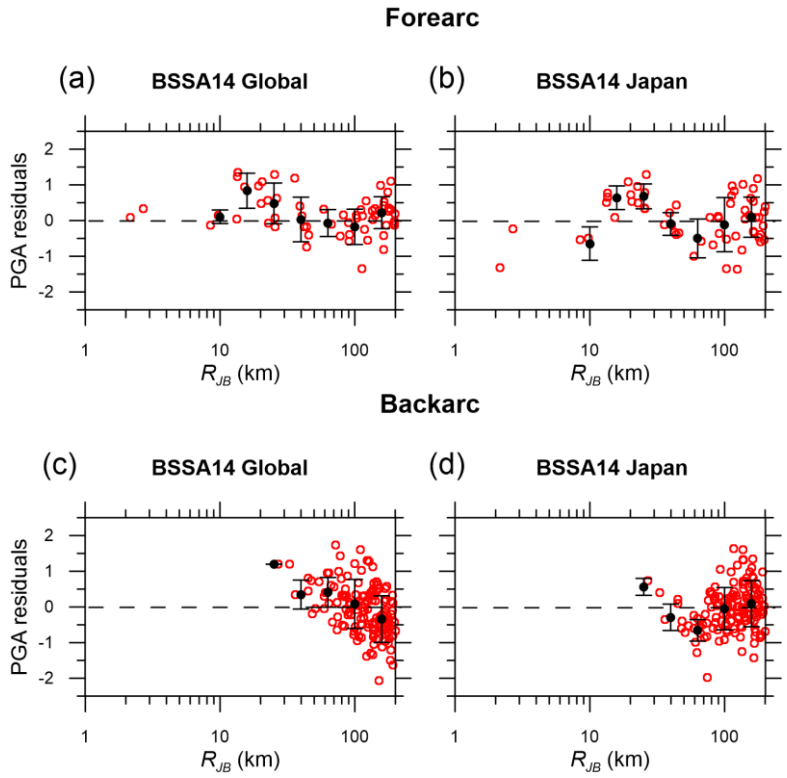

Figure 4-7. Within-event residuals of PGA from recorded ground motions relative to predictions of: (a) the BSSA14 global model in the forearc region, (b) the BSSA14 model with regional adjustment for Japan in the forearc region, (c) the BSSA14 global model in the backarc region, (d) the BSSA14 model with regional adjustment for Japan in the backarc region. Binned means shown with +/- one standard deviation.

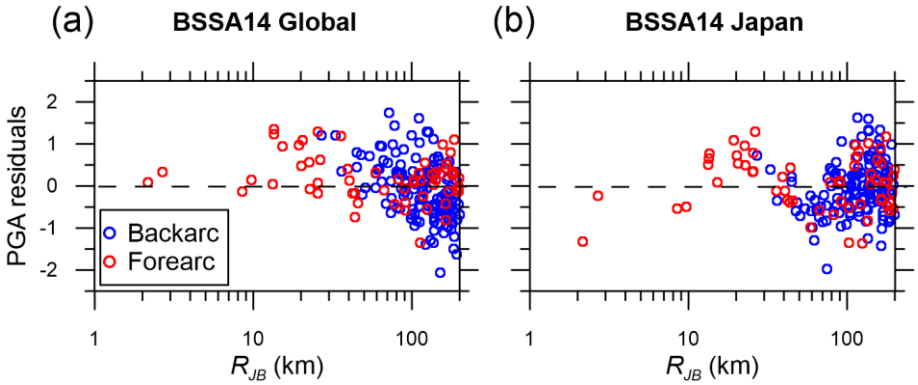

Figure 4-8. Backarc/forearc within-event residuals of PGA from recorded ground motions relative to predictions of: (a) the BSSA14 global model, and (b) the BSSA14 model with regional adjustment for Japan.

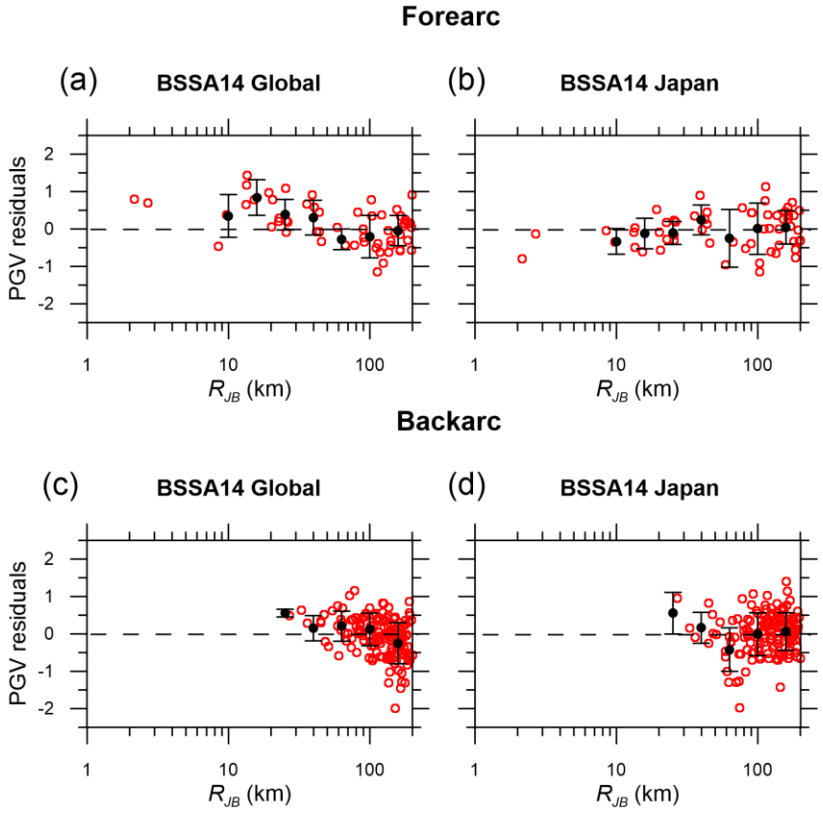

Figure 4-9. Within-event residuals of PGV from recorded ground motions relative to predictions of: (a) the BSSA14 global model in the forearc region, (b) the BSSA14 model with regional adjustment for Japan in the forearc region, (c) the BSSA14 global model in the backarc region, (d) the BSSA14 model with regional adjustment for Japan in the backarc region. Binned means shown with +/- one standard deviation.

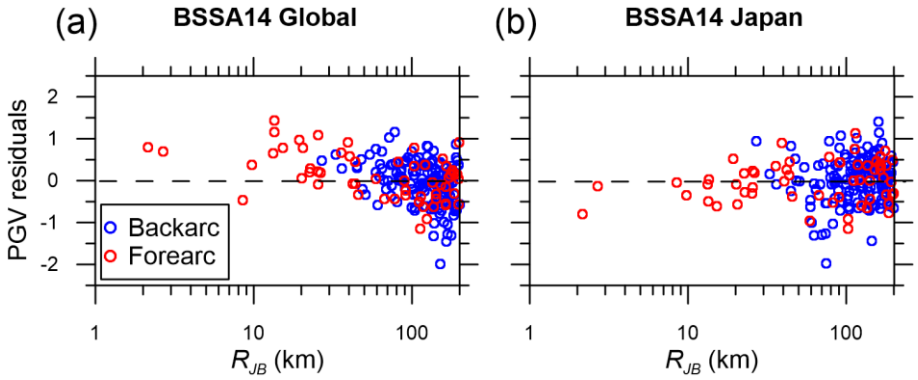

Figure 4-10. Backarc/forearc within-event residuals of PGA from recorded ground motions relative to predictions of: (a) the BSSA14 global model, and (b) the BSSA14 model with regional adjustment for Japan.

4.4 Spatial Distribution Of Strong Ground Motion

Throughout this document we report and analyze the effects of the earthquake on the natural and built environment. In this section we evaluate the spatial distribution of ground motion to estimate selected intensity measures (PGA and PGV) at sites of interest. To achieve this scope, we first perform Kriging of within-event residuals (e.g. Kwak et al., 2012; 2016) using the BSSA14 model with regional adjustment for Japan and a global variogram model (Jayaram and Baker, 2009) to take into account spatial correlation of intensity measures. Figure 4-11 shows the spatial distribution of within-event residuals from this event for PGA (Figure 4.11a) and PGV (Figure 4.11b). Also shown in Figure 4-11 is the approximate position of the volcanic arc. Figure 4.11 does not show specific differences between within-event residuals in the backarc and forearc regions. This confirms that the regionally-adjusted BSSA14 model captures the steeper attenuation with distance observed in the backarc region. Both, PGA and PGV residuals are lower in regions located N-NW and N-NE of the epicenter. This means that the GMM over predicts the motion in those areas.

We then compute the spatial distribution of PGA and PGV using equation 2:

$$\overline{\ln(Y)}_j = \mu_{\ln}\left(\mathbf{M}, R_j, V_{S30\,j}\right) + \eta + \varepsilon_j \qquad (2)$$

Where $\overline{\ln(Y)}_j$ is the mean intensity measure estimate at location *j*. Figures 4-12 and 4-13 show maps of the spatial distribution of PGA and PGV calculated using equation 2. Both maps have been prepared for a common V_{S30} value of 350m/s. Two- and three-dimensional site effects (e.g. topographic effects) are not captured in these maps. Table 4-1 shows a summary of estimated PGA and PGV values at relevant locations inspected and discussed in other chapters.

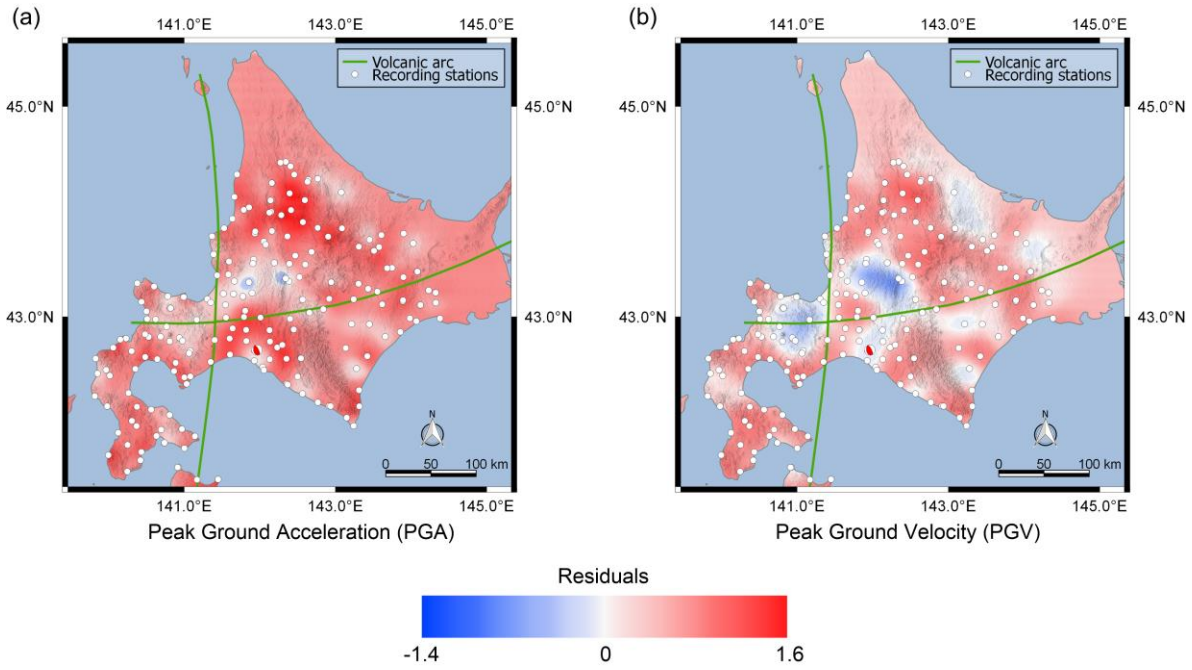

Figure 4-11. Map of within-event residuals of (a) PGA and (b) PGV from recorded ground motions relative to predictions of the BSSA14 model with regional adjustment for Japan.

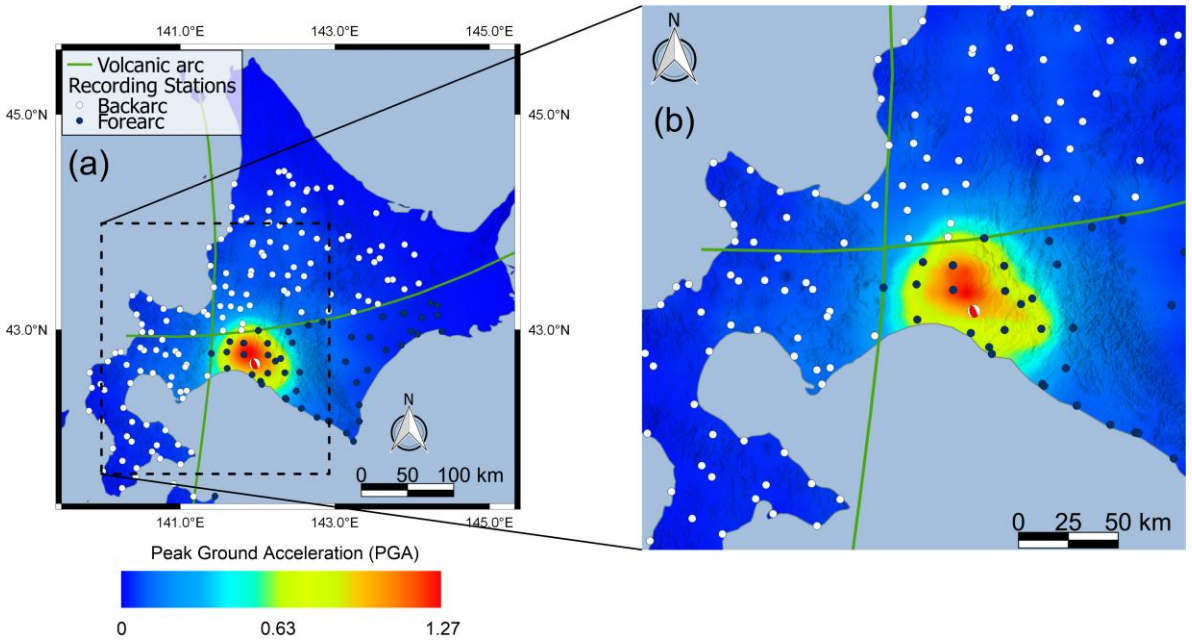

Figure 4-12. (a) Map of spatial distribution of PGA in Hokkaido; (b) Zoom in the epicentral area.

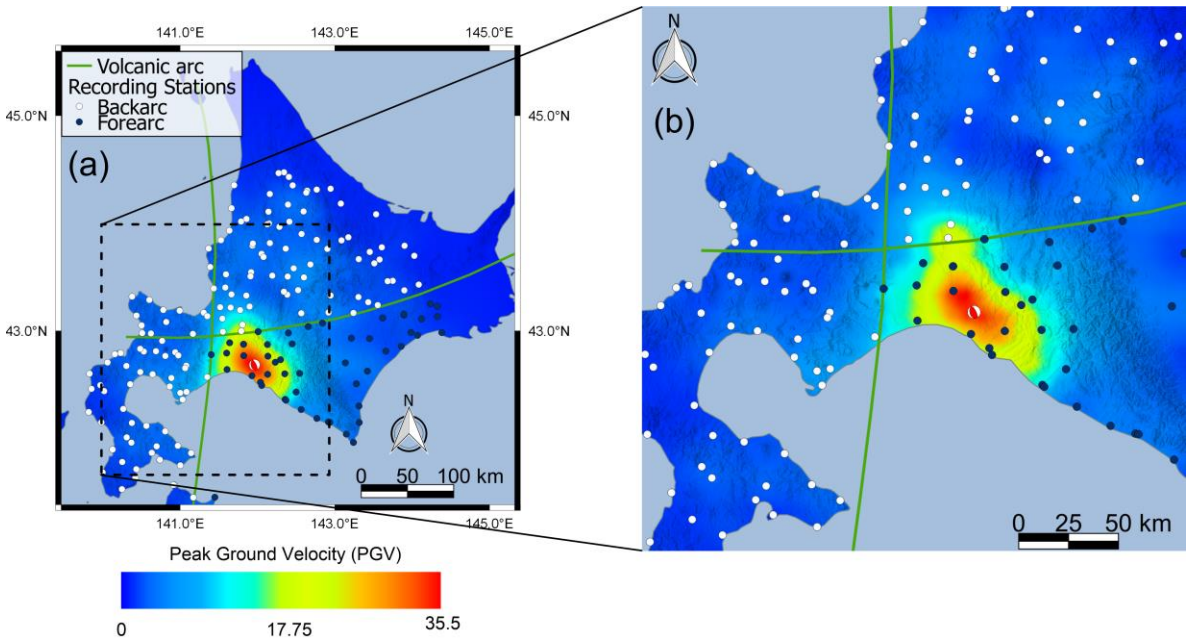

Figure 4-13. (a) Map of spatial distribution of PGV in Hokkaido; (b) Zoom in the epicentral area.

Table 4-1. PGA and PGV values estimated at inspected locations.

#	Longitude	Latitude	Feature description	R_{Rup} (km)	R_{jb} (km)	PGA (g)	PGV (g)
1	141.91	42.74858	Landslide along planar surface of pumice destroying the Yoshino town at the foot of the slope (UAV SfM model available).	29.1	0	1.2	36.6
2	141.9936	42.76631	Extensive landslide triggered the around Atsuhoro Dam.	31.2	5.3	1.0	24.1
3	141.8702	42.7568	Complex planar soil slide of ~1 – 1.5m of soil and turf sliding along pumice in a dairy farm.	28.8	0	1.2	35.5
4	141.8778	42.7644	Low angle slide.	28.9	0.50	1.2	35.4
5	141.9358	42.75145	Landslide of hillslopes above the Tomisato Water Treatment Plant.	29.6	0.35	1.2	35.1
6	141.7834	42.60658	Sand boils surrounding a light tower at southern edge of the Tomakomai port.	30.7	11.09	0.6	18.5
7	141.7833	42.60683	Minor settlement of concrete slabs and ponding of water.	30.7	11.09	0.6	18.5
8	141.782	42.60731	No damage at critical positions within the port.	30.7	11.16	0.6	18.5
9	141.4565	42.98908	Major flow-failure and settlement of a roadway in Satozuka.	50.3	41.37	0.18	6.3
10	141.4558	42.98861	Severe tilting of structure on the left contrasted with minor tilting of structure to the right. The structure of the left was an older structure while the structure of the right was of a more modern make with what thought to be pile foundations.	50.3	41.37	0.18	6.3
11	141.4568	42.98889	Severe tilting and settlement with lots of flow liquefied deposits on the road.	50.2872	41.33422	0.18	6.3
12	141.4563	42.98925	Modern apartment building with severe structural damage due to flow failure.	50.33641	41.39408	0.18	6.3
13	141.4557	42.98861	Flow failure, 3D diagonal tilt of house and roadway settlement.	50.32495	41.38014	0.18	6.3
14	141.4561	42.98919	Roadway settlement (manhole sticking out over pavement surface).	50.34055	41.3991	0.18	6.3
15	141.9397	42.57506	Sand boils on levees along Mukawa River.	28.66977	1.292649	0.41	23.5

5.0 Landslides

The M6.6 Tomakomai earthquake triggered more than 3,300 landslides in southern Hokkaido (Fig. 5.1) covering a total area of 66.75km^2 (GSI, 2018). Landslides were mapped by the Japanese Geographical Survey Institute (GSI) from aerial photographs collected Sept. 6-11). Landslides were a leading cause of human and structural losses in this earthquake, and in the epicentral regions of Atsuma, Mukawa, and Abira were likely responsible for virtually all of the 37 fatalities and 321 completely destroyed buildings (FDMA (2019) http://www.fdma.go.jp/bn/2018/detail/1074.html).

Landslide occurrence was pervasive in the region NW of the epicenter, in many places over 50% of a particular hillslope failed. Observed landslides were typically thin (50 – 100cm deep), involving only the soil – pumice mantle that covers the local landscape. Landslides were primarily found in steep, forested and recently logged, low-relief hills (e.g., Fig 5-2A,D). Several additional landslides were found in low-angle pastureland (e.g., Fig 5-2B). In most cases, landslide failure and runout appeared to have been rapid and partially to significantly influence by high saturation levels, landslide runout channels were consistently streaked, and deposits fluidized in appearance (e.g., Fig 5-2C). Where landslides occurred along relatively steep topography, remaining deposits were in highly disrupted lobes, often extending well into, or across rice or other agricultural fields at the toe of the slope (Fig 5-2C). Horizontally oriented trees were common where deposits were left undisturbed. Along low-angle hillslopes, planar failures along a shallow pumice layer were observed where the surficial soil and grass were left intact over displacements of several meters (~2 – 10m). Two large dam-forming rock slides were observed by a later reconnaissance by Pacific Gas and Electric (PG&E) in regions that were inaccessible during the GEER reconnaissance mission. Observed rock slides appeared by be along a clay or altered ash layer at depth within the Kawabata formation and led to significant damages to power infrastructure. In several locations landslides were observed overtopping concrete retention walls and mesh rock-fences. Failure of retention walls themselves was not observed.

Landslide mapping by GSI made little attempt to discretize individual landslides where runout deposits coalesce, or relatively small slides occurred in close proximity (e.g., Fig 5-2A landslides mapped as a single connected failure). It is possible the number of landslides triggered by this earthquake if mapped from the perspective of unique source-zones could be over 5,000 landslides (from 3,307).

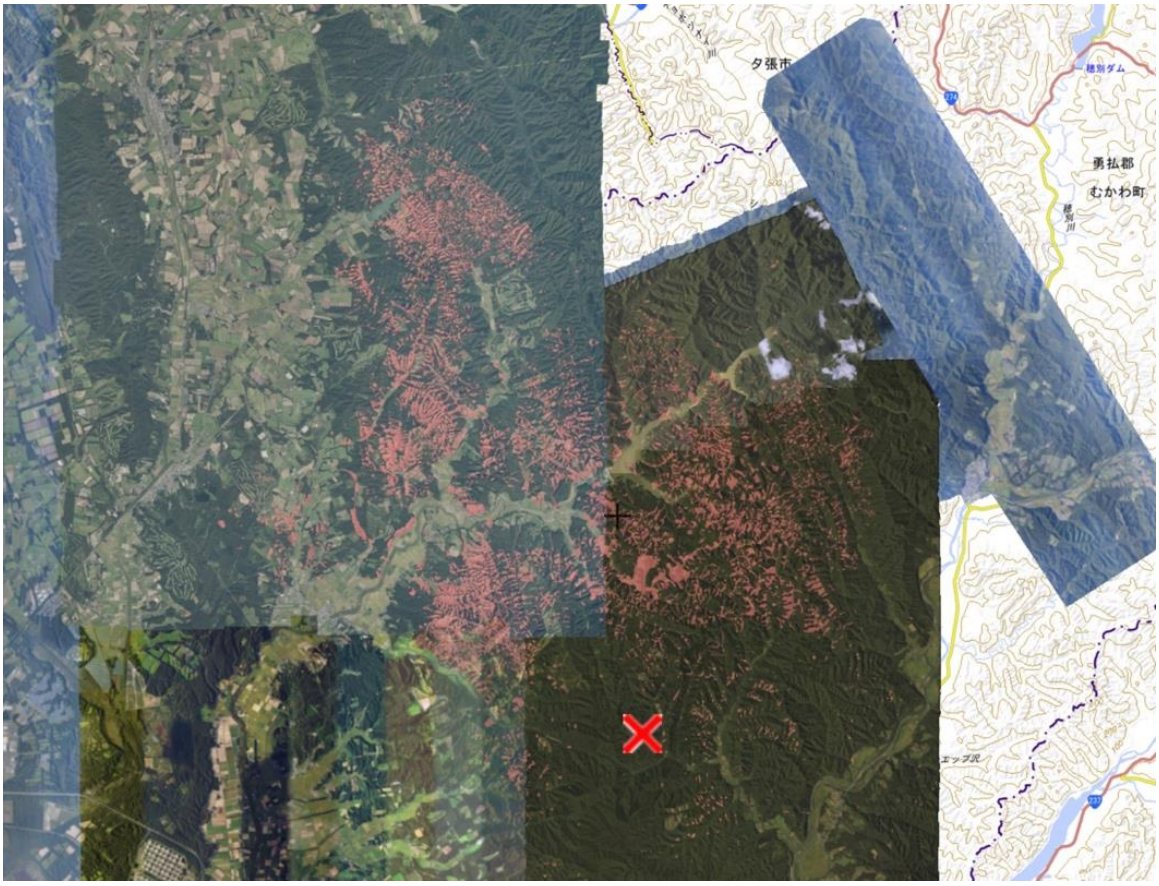

Figure 5-1. Post-earthquake aerial photos collected Sept 6 – 11 and coseismic landslides mapped by the Japanese Geographical Survey Institute (http://www.gsi.go.jp/BOUSAI/H30-hokkaidoiburi-east-earthquake-index.html#10, last accessed Oct, 2018). M6.6 epicenter [GSI] marked by red 'X', landslides shown as pink polygons

Figure 5-2. Typical landslides observed following the 2018 earthquake. A. shallow flowslide along pumice failure surface along Rt. 59. B. Low angle planar soil slide along pumice failure place (cow-slide). C. Fluidized runout of a highly destructive flowslide along Rt 1065. D. Shallow debris slides at Horonai, failure depths limited by near-surface Kawabata formation that did not appear to slide.

5.1 Pumice Deposits

The meizoseismal region is mantled by several meters of successive pumice deposits from Late Pleistocene to Historic eruptions originating near the Shikotsu Caldera. Landslide failure planes were most likely located within Tarumai pumice, Ta-b (1667 CE), Ta-c (0.8 – .9 kya), or Ta-d (3 – 5 kya). Observed failure depths (50 – 100cm, typ.) do not support the potential for failure within the more massive Shikotsu pumice deposits (20 – 40 kya), or the Holocene Eniwa Pumice (>5 kya).

Thick organic soil deposits observed at the base of the Rt 59 landslides (Fig. 5-3) likely fully developed organic soil horizons derived from Ta-d, suggesting Ta-c and or Ta-b as pumice failure planes.

Figure 5-3. Pumice exposed by reconstruction work in the toe of Landslides along Route 59. Right, cartoon of the near-surface pumice stratigraphy at Hayakita after Ishii (1963). 70cm Pumice deposit (left) likely from Ta-b and Ta-c eruptions, possibly resting on organic soils derived from Ta-d. Image and soil column figure reflect data collected 13km apart.

5.2 Landslides in Steep Hillslopes

A large majority of landslides observed in the GEER reconnaissance were relatively thin (<2m thick) planar slides to flowslides that occurred along hillslopes of approximately 25 – 35° slope angles. Runout from these landslides was frequently greater than 10m, and in some instances of channelized flowslides runouts were well in excess of 100m. Distinctions between highly mobile flowslides and planar debris slides appeared to be strictly related to pre-failure hillslope geometry, where planar or convex portions of the landscape failed as debris slides (e.g., Figs 5-4, 5-6) and channelized (concave) portions of the landscape developed into long-runout flowslides (e.g., Fig. 5-5). In both cases the same package of surficial pumice is along the basal failure surface, however increased saturation within concave channels in the landscape likely facilitated observed increased runout.

Figure 5-4. UAV SfM model of the Yoshino landslide complex. Landslide failure was along a shallow, approximately planar, surface of pumice (Ta-b/c?) causing complete destruction of the community at the toe of these slopes and running into the adjacent rice fields. Failed slope angles ~30° (141.91, 42.74858).

Figure 5-5. Extensive landslide triggering near Atsuhoro Dam. Long runout flowslides occurred in most hillslope concavities, coalescing and completely inundating side-channels throughout the landscape (e.g., left edge of this image). Landslides occurred in hillslopes of various ages of logging production / tree-cover. Dam crest is ~515m long for scale (141.9936, 42.76631).

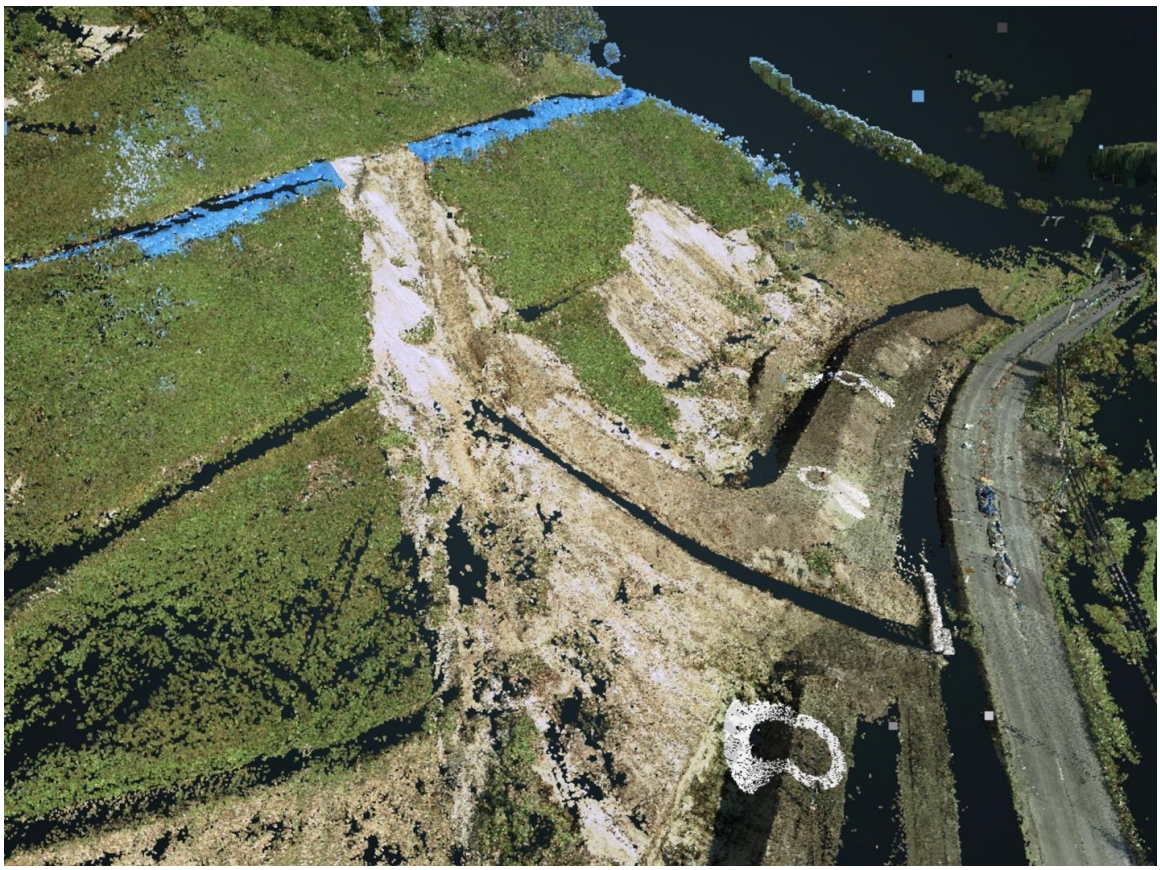

Figure 5-6. Terrestrial lidar point cloud of shallow landslides along Route 59. The foreground landslide as observed was over 130m long, and considerable reworking (e.g. earthen berm) of the runout deposits had previously occurred. Distal slide never greater than 1m in thickness 42.6974, 141.9471.

5.3 Landslides in Low-Angle Hillslopes

Several landslides around Atsuma were observed in hillslopes at angles of 20° or less that developed planar soil slides with displacements of a few to tens of meters (e.g., Figs 5.7-8). The most impressive of which, Fig 5-7 'Cow-slides', was a complex planar soil slide of ~1 – 1.5m of soil and turf sliding along pumice in a dairy farm. Within the small cow-slide system were three sets of landslides failing in opposing directions, at least three small landslide-dammed ponds, complex arcuate crack systems throughout the hillslope, and a beautiful compressional zone at the toe of the landslide. Smaller displacement slides were observed in nearby hillslopes (Fig 5-8) of shallower angles (~12°).

Figure 5-7. Top. UAV-SfM model of the multiple dam-forming 'Cow slides' near Atsuma [42.7568°, 141.8702°]. Bottom. Image looking across the face of the landslide. Surficial turf and organic soils failed as a coherent mat, displacing upwards of 70m downslope damming the central irrigation ditch. Principal failures moving left to right (white arrows) along slopes of ~20°, and included highly complex head and side cracking systems and compressional ridge of displaced turf and soil at the toe. Landslide failure was nearly continuous over the left ridge into a steeper slope severely damaging a residential structure, and right to the adjacent slope also failing towards the irrigation channel.

Figure 5-8. 'Low-angle' slide along a ~12° slope within pastureland near Atsuma 42.7644°, 141.8778°]. Sliding plane ~1.5-2m in depth, with relatively intact sliding of the failed mass. A smaller failure along the facing hillslope (right of this image) with little permanent deformation was also observed. These landslides were not mapped by the GSI from aerial images.

5.4 Water Treatment Plant Landslides

Landslides due to the near-total failure of hillslopes above the Tomisato Water Treatment Plant (WTP) caused significant damages to the plant, including stripping an enclosed access stairway from the water tower and transporting it over 60m downslope (Fig. 5-9). WTP structures were founded on deep piles and generally performed very well. Evidence of landslide deposits was observed 13m above grade on the upslope side of the water tank and overtopped the main building. However, landslides led to the destruction of the stairway accessing the upper water tank and a smaller auxiliary building that is not visible in these post-landslide images.

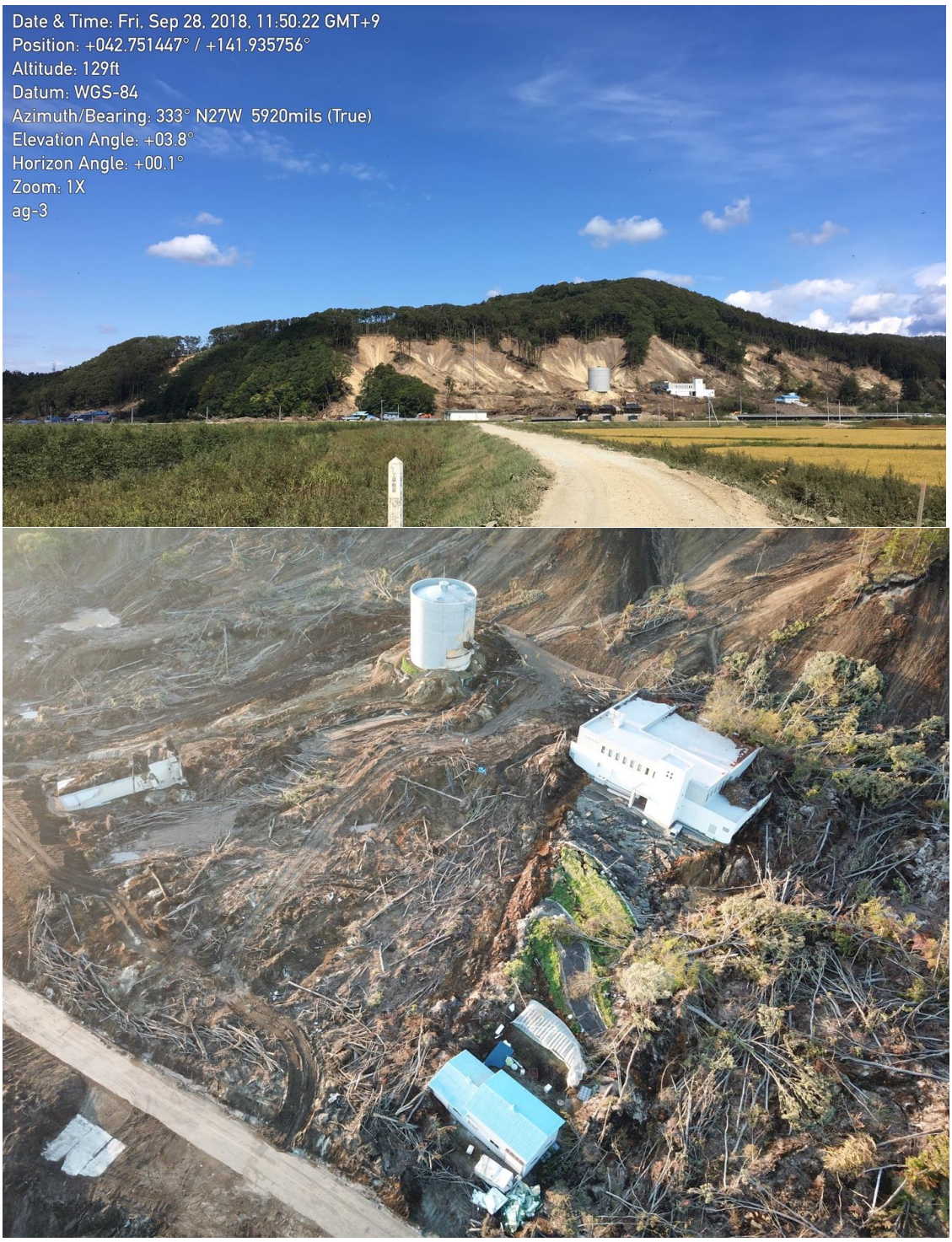

Figure 5-9. Landslide damages at the Tomisato Water Treatment Plant. Top, overview of slope failure. Bottom, UAV-image showing the displaced stairway (left) and protected shadow zone by the surviving main-building. Both water tower and main building are founded on deep piles

5.5 Performance Of The USGS-Ground Failure Predictions Of Landslide Probability

Following significant earthquakes, the USGS automatically generates ground failure (landslide and liquefaction) hazard maps based on small-scale global topographic and geologic and shakemap shaking intensities. For the Hokkaido earthquake, USGS landslide estimates were for a significant (~12km^2) area to be exposed to landslide hazard with little to no population exposure. Macroscale estimates of landslide hazard magnitude from the USGS appear consistent with field observations, but USGS model predictions misidentified the exact zones of high landslide occurrence. As shown in Fig. 5-10, zones of high predicted landslide probability computed by the USGS overpredicted high landslide probability along the Shikotsu Caldera (no reported landslides) and east beyond the Mukawa river (very few landslides observed, no major landslides reported). Areas observed and mapped to have extensive landslide triggering during this earthquake are generally along the western edge of low landslide probability from the USGS model, or in zones of no predicted landslide probability. Landslides observed in this reconnaissance typically occurred within moderately slopes hillsides (15 – 30°), likely where sufficient holocene pumice deposits accumulated, and not in the steepest portions of the landscape predicted to fail in the USGS model were more surficial bedrock may be present. Directionality of strong ground motion NNW from the earthquake source and unconsolidated surface deposits (pumice) not captured by the USGS model may also contribute significantly to the observed misfit between predicted and observed landslide concentrations.

5.6 Deep-Seated Landslides

In contrast to ubiquitous shallow landslides in and around the epicentral area, the PG&E-SCE-InfraTerra team observed two deeper landslides that damaged electric transmission towers north of the epicenter. Both of these deep-seated, translational landslides occurred within bedrock and exhibited typical features for sliding failures along a discrete weak layer, including well-defined headscarps and sidescarps, and translated blocks with varying degrees of internal deformation. Interpretation of aerial imagery from before the earthquake and post-earthquake field observations document geomorphic evidence of pre-existing failure, including incipient headscarp grabens. For the Horonai Mega Block Glide, this failure represents a partial failure of a larger pre-existing slide, which is bounded by similar large pre-existing slides that did not experience significant movement during the Hokkaido earthquake. This suggests a long history of deep-seated landsliding potentially concurrent with past large earthquakes.

5.6.1 Horonai Mega Block Glide

Approximately 3.2 km southeast of Horonai Village, an entire bedrock ridge measuring approximately 900 meters long by 200-300 meters wide slid 350 meters south-southwest, blocking a 200-meter-wide west-northwest trending stream valley. The slide blocked the stream in the valley, forming a landslide lake. At its northeast (upslope) end, the landslide created a basin measuring several hundred meters long filled with large rock masses and piles of debris. The post-slide length of the ridge is approximately 200 meters less than the pre-slide length due to shortening at the toe of the slide where it was buttressed against the far side of the stream valley, and spalling of debris into the graben on the uphill side of the slide.

Total slide translation was accurately measured using a distinctive vegetation-free transmission line corridor that crossed the axis of the ridge at a nearly perpendicular angle (Figure 5-11) and could be matched with the transmission line corridors on the intact hillslope to both sides of the failure and transmission towers that were still standing outside the margins of the slide (Figure 5-11).

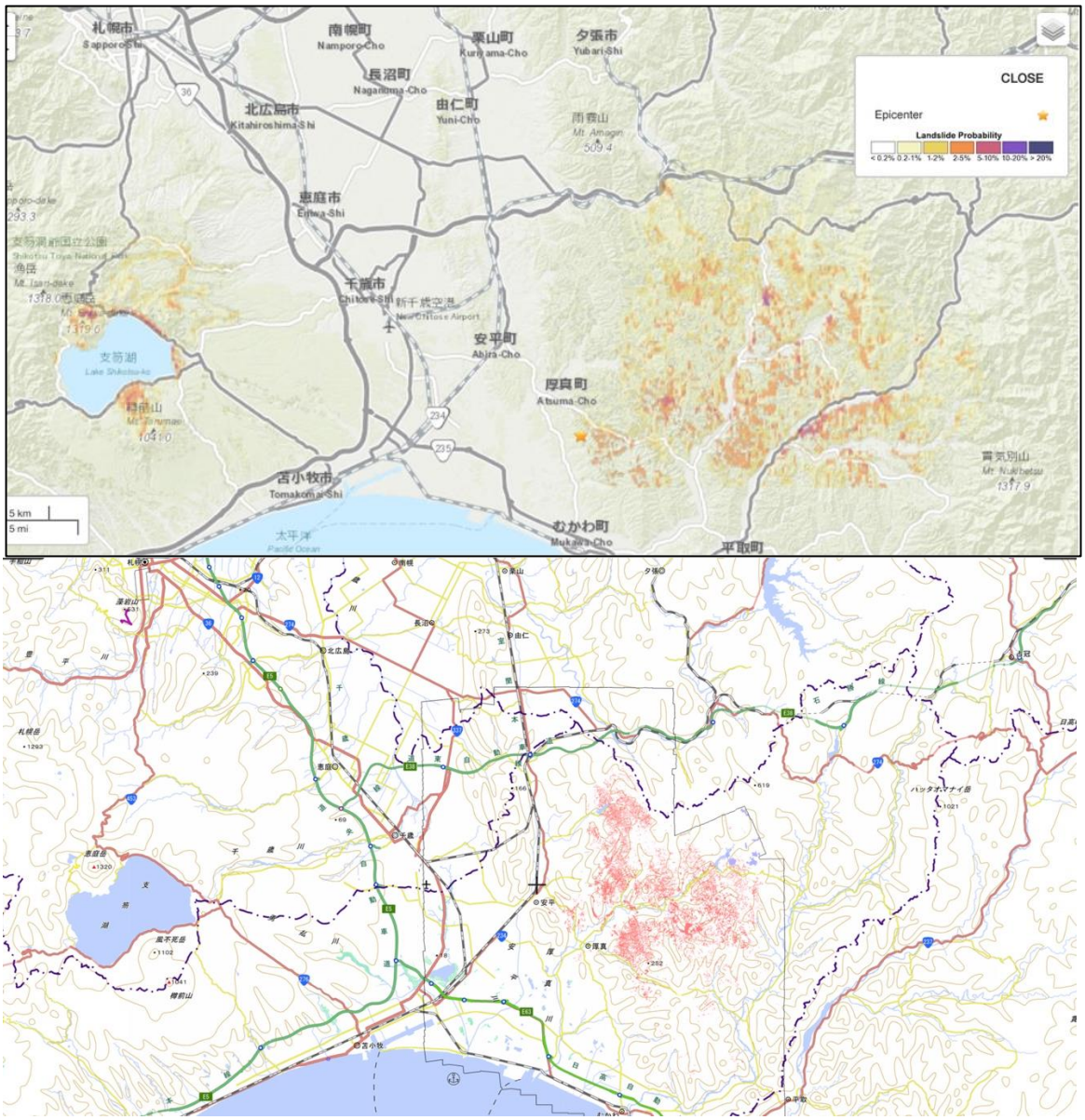

Figure 5-10. Comparison of USGS Landslide Probability prediction (top) and mapped landslides (bottom).

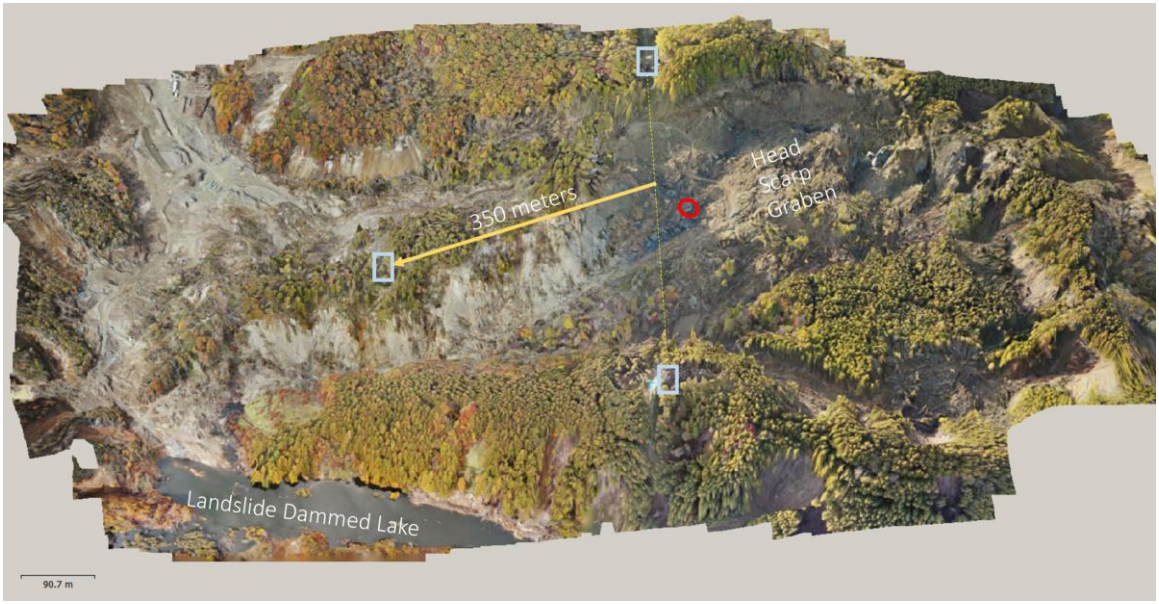

Figure 5-11. Drone composite image showing Horonai megaslide with offset (solid yellow line) of electrical tower relative to original electrical alignment (yellow dashed line). Tower locations are shown as white boxes. Approximate center point of composite image: 42.736835°, 142.005206°

The middle transmission tower on the landslide collapsed and was translated downslope along the axis of the slide approximately 350 meters from the pre-slide location. This tower likely was pulled over during translation by resistance from the electric conductor wires that remained connected to the stationary towers located on either side of the slide before the lines broke. Towers on either side of the slide did not appear tilted or otherwise pulled out of plumb but had minor damage (cracking) to their foundation blocks. Shallow secondary slides, including translational and debris flow failures, formed along the slide scarps and translated blocks, and also encroached on the foundations of the two stationary towers outside of the main landslide. Reconstruction work that was proceeding during the field reconnaissance included moving these two towers away from the encroaching shallow slides and enlarging foundations and tower structures to heighten the lines and increase the conduit spans to enable the entire mega slide to be spanned, eliminating the need to replace the translated tower with a new tower on the slide mass.

We understand that the electric company plans to construct an emergency spillway to drain or control the impounded landslide dam reservoir upstream of slide, and geotechnical drilling within the landslide toe (ongoing at the time of the field visit by the PG&E-SCE-InfraTerra team) will be used to help plan excavation for this work.

Mapping along the margins of the slide and core recovered from the landslide toe in geotechnical borings indicate that the ridge is composed of hard interbedded Kawabata marine mudstone and fine sandstone. The layered sequence of turbidite sandstone and interbedded mudstone dips gently to the southwest. Specific efforts were made to identify possible weak layers in the translated slide mass or scarps to determine the likely basal sliding surface and slide mechanics. With the exception of some very thin (<1/8-inch thick) hardened ash layers sandwiched between hard bedrock blocks, candidate weak beds were not observed in the slide scarps and blocks. However, a zone of stiff clay blocks and debris were found in a localized zone at the very base of the sidescarp along the north margin of the large slide that could represent a weak mudstone or possible weathered ash layer that could be associated with the landslide basal failure zone. Similar clay zones were observed in the geotechnical

boring core borings approximately 50 meters below the crest of the ridge. The clay zones consist of a weak, one-foot-thick clay layer that separates fractured rock above from competent rock below. Blocks of similar clayey material were found in the deepest part of the basin northeast of the slide. The location and depth of the core boring clay, and similarity to the material found at the base of the side scarp higher on the slide mass, suggest that this clay zone represents the slide plane material. Samples were collected of this material, and the PGE-SCE-Infraterra team plans to perform some geotechnical laboratory work to classify and characterize the strength.

Several key evaluations are believed important to further assess the mechanics for this large slide:

- Geotechnical characterization of the basal failure clay samples;
- Development of geotechnical cross section(s) of the slide;
- Slope stability back-analyses;

This work will help evaluate why this large landslide mobilized during the earthquake, especially in light of the scale of the failure and amount of translation, impacts on the electric transmission lines, and apparent low angle failure surface relative to the stiffness of the clay layer materials. Comparison of conditions and geometries between the large mobilized slide and adjacent existing landslides that did not mobilize, could help inform models for earthquake triggered deep seated landsliding.

5.6.2 Hobetsuizumi Landslide

Approximately 2.3 km northeast of Hobetsuizumi and 1.75 km east of Route 74 the PG&E-SCE-InfraTerra team observed a landslide measuring approximately 120 meters long by 80 meters wide above a meander bend in small unnamed river (Figure 5.12). The slide is part of a larger pre-existing landslide complex that has pushed the river to the south. The slide translated the base of a transmission tower (No. 71) of the KEPCO Iwachishi Line (66 kV) approximately 15 meters downslope, causing it to collapse in the uphill direction.

Figure 5-12. Drone image with view to northeast showing Hobetsuizumi megaslide with offset of electrical tower (within red circle). Water seepage visible at location indicated by blue arrow with red arrow showing upper inset slide plane. Photo location: 42.718279°, 142.151628°.

A steep stream-cut exposure along the eastern margin of the landslide reveals that the slide occurred in fine grained marine bedrock. In the same exposure, water could be seen draining from the inferred slope-parallel slide plane, which separates crushed rock above from more competent rock below (Figure 5-12). Based on the exposure and observed surface offset, failure likely occurred along pre-existing bedding planes and the slide was primarily translational.

A graben measuring approximately 15-20 meters wide and 10 meters deep formed at the head of the slide (Figure 5-13). Pre-existing topography visible within the slide block downslope of the graben includes a broad, slope-parallel depression likely formed during previous slide movement.

HEPCO activities to restore the Iwachishi 66 kV Transmission Line included relocation of the collapsed tower to the top of the ridge located upslope of the landslide graben and replacement of two other towers north and south of Tower 71 on hillsides along the electrical corridor. Replacement of the towers included drilling of deep piers into bedrock.

Figure 5-13. Drone image of the upper graben within the headscarp of the Hobetsuizumi megaslide. Note collapsed electrical tower (within red circle). 42.719687°, 142.151401°.

6.0 Liquefaction

6.1 General Observations

Limited surface expressions of liquefaction were observed during our reconnaissance following the Hokkaido earthquake, though a dramatic and highly damaging flow failure in Sapporo (described below) was observed. Numerous sand boils and small vertical and horizontal displacements due to lateral spreading were observed near the East Port of Tomakomai. Cracking and small downslope displacements along levee crests were observed near Mukawa. Away from the coast, in the epicentral region of Abira and Atsuma, the GEER team noticed uplifted manholes indicating poorly compacted backfill for buried utilities. The most serious cases of liquefaction of backfill was observed in Abira township. Due to the timing of our reconnaissance and rapid response of local authorities, additional evidence of liquefaction may have been removed prior to the GEER team reconnaissance along susceptible areas along rivers and the coast. At the southern edge of Sapporo city, significant damages to the Satozuka neighborhood [141.4565, 42.98908] were caused by flow failure of pumice fill. Vertical displacements of residential structures and roadways due to evacuated material was in excess of 2m in places. Complete damages and costs due to this (liquefaction) flow-failure feature are to be determined, but the Sapporo City Waterworks Bureau reported 62 red-tagged and 47 yellow-tagged structures within the Satozuka flow slide. Terrestrial lidar scans were collected at both the East Port of Tomakomai and Satozuka liquefaction sites to preserve displacement and damage data. These datasets are available via DesignSafe.

6.2 East Port Of Tomakomai

The GEER team visited the East Tomakomai Port situated in the south-west section of the Atsuma area. At the time of our reconnaissance the largest section of liquefaction-damaged port facility pavement had been removed. Remaining liquefaction induced settlement along the edges of the active container yard were typically 10cm or less (vertical). Material found from sand ejecta was sandy silt of marine origin, with minor traces of shells fragments. The ejecta was an anoxic color of dark grey. This material has little fines content and did not seem to have any plasticity. The liquefied areas of the active port were cordoned off, and the main container rails and deck were undamaged and operational. Adjacent to the port facility were undeveloped fields where widespread sand boils were observed via UAV surveying. Historic maps of the area from the 1950s and 60s show the area was formally a shallow harbor before reclamation and the development of the port facilities.

Figure 6-1. Sand boils surrounding a light tower at southern edge of the Tomakomai port. Sand boils were observed near the southern seawall and in the container back-yard at the port and in undeveloped areas of the port between the marine container facility and the HEPCO coal plant. 42°36’23.7”N 141°47’00.7”E.°

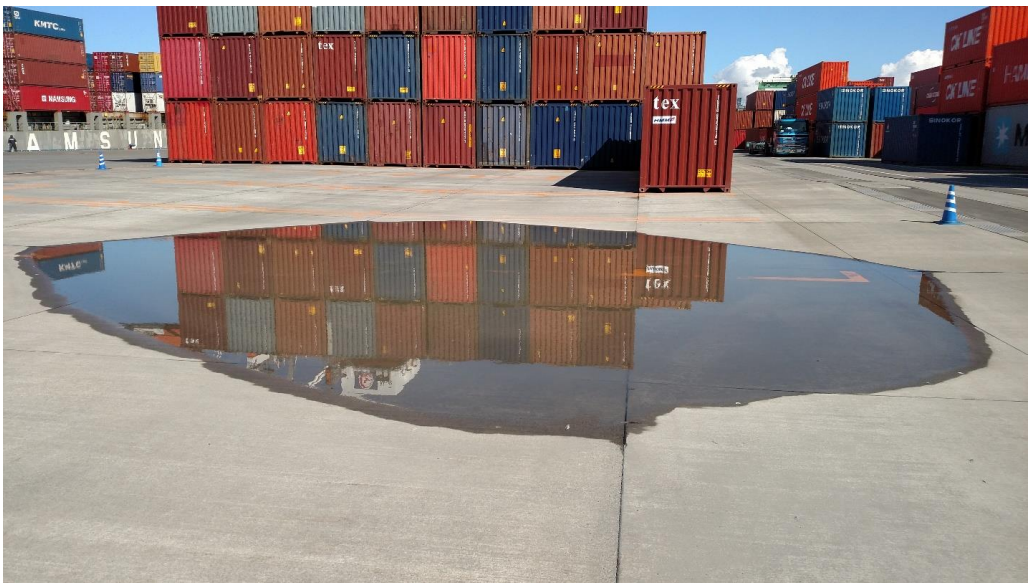

Figure 6-2. Minor settlement of concrete slabs and the ponding of water. Truck traffic was directed around these locations but were otherwise not hindered. 42° 36’ 24.6” N 141° 46’ 60.0” E.

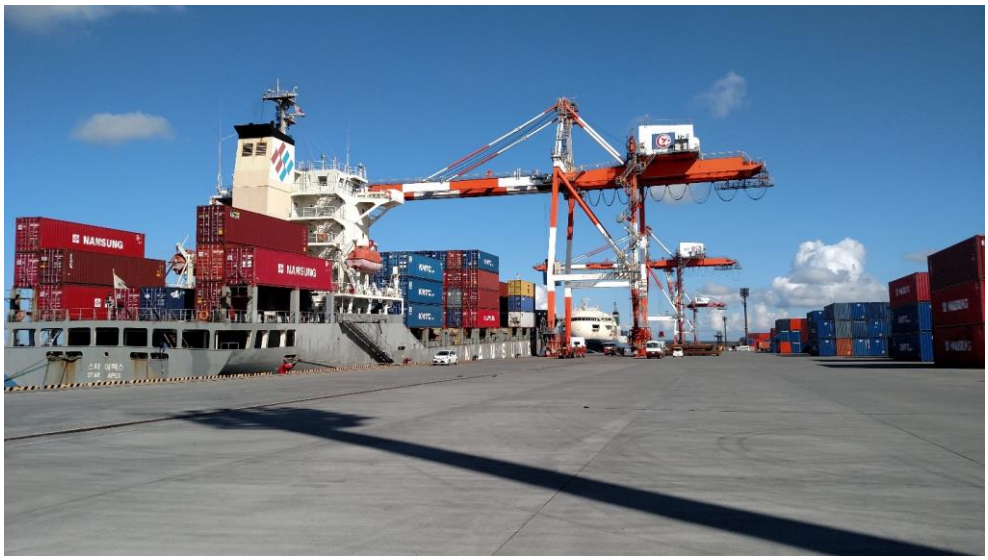

Figure 6-3. The critical locations of the port were undamaged and in heavy use when the GEER team visited on 28 September 2018. 42°36’26.3”N 141°46’55.3”E.

6.3 River Flood Control Levees Near Mukawa Town

We observed several cases of embankment crest settlement and liquefaction of the native soil adjacent to embankments. Damage was observed in the Mukawa area and upriver in the flood control levees north of Mukawa along the river. The GEER team inspected these locations and found blue tarped tops of levees covering decimeter scale longitudinal cracks and vertical offsets. There was evidence of sand boils at several locations along the riverward toe of the levee (Figure 13)

Figure 6-4. Sand boils observed by Japanese researchers (left), Map of Mukawa river locations near coast highway 235 (center), examples of blue tarp covered crest settlements of flood control levees along the Mukawa river (right). Japanese researchers identified liquefaction features (yellow circles) along the riverward side of the levee embankment. 42°34'30.2"N 141°56'23.0"E.

6.4 Sapporo City, Satozuka

Within Sapporo city, volumetric collapse or liquefaction of pumice backfill below the neighborhood of Satozuka led to a highly destructive flow slide. While most of the flow-failure deposits had been removed by time of our reconnaissance, widespread evidence of vertical displacements, damages to structures, roadways, and pipelines were evident. Remnant deposits from the flow-failure found below floated cars (Figure 6-15) were a very light, porous, non-plastic pumice sand of fairly uniform size. Vertical subsidence associated with material loss due to flow-failure extended 230 – 240m along the length of the affected area, with differential vertical settlements up to 2.2m. At the time of our reconnaissance we were not able to fully observe the extent of the deposits as considerable remediation of the site had already occurred. Liquefaction and subsequent flow sliding occurred at Satozuka within a deposit of pumice fill placed during the 1980s. Pumice was mined from 20 – 40kya deposits of the Shikotsu-1 volcanic eruption and used to fill in a 10m deep ravine where present-day Satozuka was developed. Liquefaction and flow slide induced vertical displacements were greatest within the central channel of the former ravine where pumice fill deposits were thickest.

Structural performance within Satozuka was highly dependent on foundation design. Older (1980s) structures on mat foundations suffered significant differential settlements leading to damaging or descriptive rotation of the dwelling (e.g., Figures 6-11, 6.13-14). Modern (post 2000) dwellings on pile or other deep foundations appear to have been unaffected by any liquefaction-induced displacements below them (e.g., Figure 6-10). Similarly, manholes in the Satozuka neighborhood were founded on native soils below the pumice fill and exhibited no vertical displacement following liquefaction and flow

sliding (e.g. Figures 6-9 and 6-12). However, significant breakages of pipe and service disruptions did occur due to pullout failures in the lifeline network (see Chapter 7 for additional information.) Figures 6.7–15 show the effects of flow-failure across Satozuka running from source to deposit of the flow slide.

Extensive terrestrial lidars scans were collected as part of the GEER reconnaissance to digitally preserve the Satozuka site for future case history development. 38 individual lidar scans collected over three days were collected along the length of the flow-failure and from above via an adjacent parking garage structure. The complete raw data and single merged point cloud from all scans are available via DesignSafe. Due to the pumice rich soil, any SPT and CPT testing in the area may not give reliable penetration values. This is because pumice is a crushable material that is broken apart during dynamic testing (Miura et al, 2003). On the other hand, the soil had extremely low residual strength, and the expectation would be that the penetration resistance will be very low. Kiyota ward flow liquefaction area is a good target for further testing the mechanical properties of volcanic sediment, especially pumiceous soils.

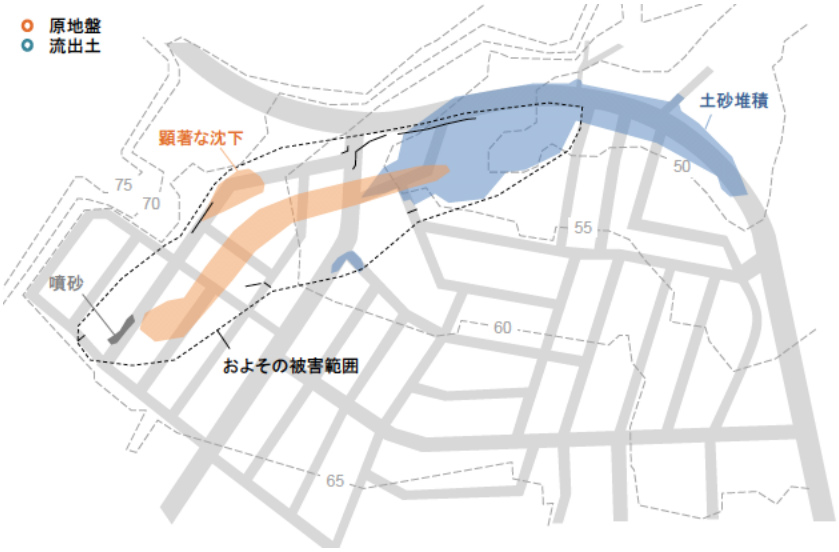

Figure 6-5. Overview of the Satozuka flow-failure. Orange – loss of material, Blue – deposition. Dashed grey lines show modern topography of the area, linear orange zones of loss reveal a former channel that was backfilled with pumice.

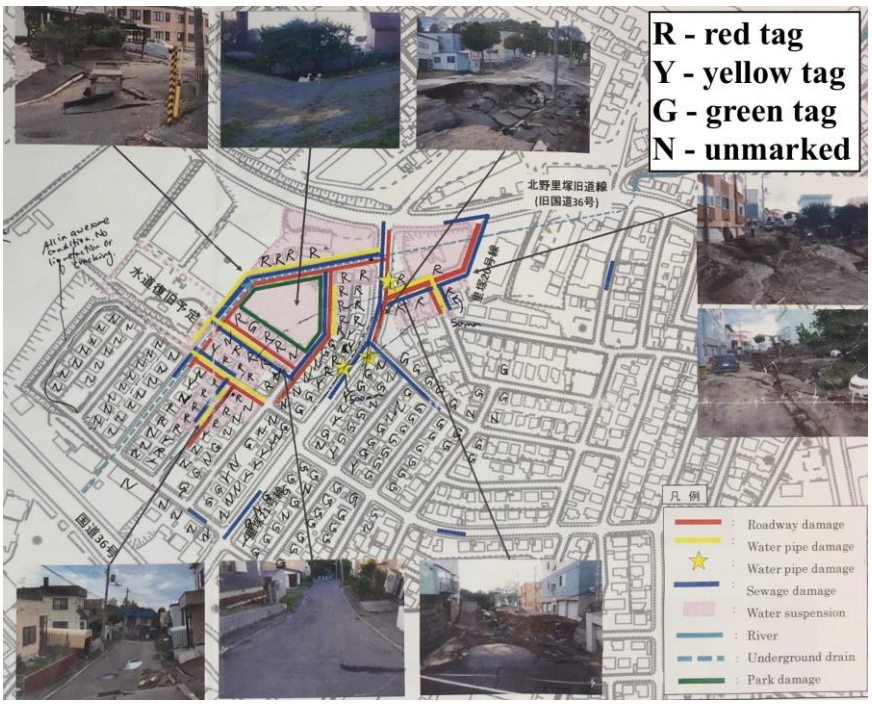

Figure 6-6. Distribution of structural tags due to flow-failure damage. Damages were most concentrated around the community park (green pentagon) and along a single street in the upslope direction (lower-left) following the former river channel where pumice backfill was locally thickest. Note adjacent structures tagged 'Red' and 'Green' likely due to foundation differences (e.g., Fig 6.10) Background image modified from data provided by the Sapporo City Waterworks Bureau.

Figure 6-7. Head scarp of the Satozuka flow-failure. The full extent of cracking and potential damages was obscured by tarping and ongoing repairs, vertical offset at this location ~4ft (1.22m).

Figure 6-8. Looking down-slide from above the head scarp. Tilt of structure at end of street typical.

Figure 6-9. Stable manhole covers revealing the broader vertical settlement of Satozuka outside the more intense channelized material evacuation. Local utilities were placed on the underlying soils at depths of up to 10m and did not show vertical displacements during liquefaction.

Figure 6-10. Contrasting building ages and foundations showing significantly different performance during the Satozuka flow-failure (main channel of deformation passes through these homes). Left, older mat foundation home with significant rotation and differential settlement. Right, contemporary home on piles, structure stable relative to down dropped surface (~2m).

Figure 6-11. Significant rotation of a residential structure due to flow-failure-induced differential settlement

Figure 6-12. Manhole, founded on native non-liquefiable material at 10m depth. Surrounding pumice fill evacuated during flow-failure leading to significant vertical deformation shown here.

Figure 6-13. Modern apartment building with severe structural damage due to flow liquefaction. 42°59’21.3”N 141°27’22.6E.

Figure 6-14. Lower Satozuka flow slide, differential settlement highlighted by severely tilted structures towards the central flow path. Deposition zone off-camera to the right. 42°59’20.1”N 141°27’24.6”E.

Figure 6-15. Deposition zone of the Satozuka flow-failure slide. Nearly all depositional material was removed prior to reconnaissance (red arrows indicate deposit highpoints). Rafted cars originally in closed garage bays that were damaged and filled with pumice.

7.0 Performance of Dams

7.1 Synopsis Of Dam Performance, Inspection, And Review

A significant number of dams are located on Hokkaido Island for the purposes of water supply and electric power generation (Figure 7-1). A particular area of interest for the post-earthquake reconnaissance was to perform an initial canvassing of dam performance in the general epicentral area of the earthquake. The screening assessment included site visits to four dams: Atsuhoro Horonai-Atsuma, Mizuho, Nibutani, and Hobetsu Dams (Table 7-1 for descriptions). Relatively high levels of ground shaking were recorded at the dam sites, in cases close to 1.0 g.

Table 7-1. Overview of Visited Dams

Dam Name	Dam Type	Dam Height (m)	Base Acc. (gal)	Crest Acc. (gal)	Damage State	Link to Japan Database
Nibutani	Concrete Gravity	32	158	206	None	http://damnet.or.jp/cgi-bin/binranA/enAll.cgi?db4=0149
Hobetsu	Embankment	38	224	706	None	http://damnet.or.jp/cgi-bin/binranA/enAll.cgi?db4=0114
Mizuho	Rockfill	26	491	937	Minor	http://damnet.or.jp/cgi-bin/binranA/enAll.cgi?db4=0164
Atsuhoro – Horonai Atsuma	Concrete Gravity	-	-	-	None	Local engineers were not consulted and dam parameters/response not acquired

Geotechnical dam engineers from PG&E and SCE performed visual screening of accessible areas of the four dams in the interest of understanding the performance of dams during seismic events.

In addition to visual observations by the PG&E/SCE/Infraterra field team, discussions were held with dam operators which included information conveyed on ground motion recordings from seismographs at the dam sites and in cases at the base and top of the dam structures. The team was able to walk on and around the Hobetsu Dam, but for other dams access was only permitted from abutment areas.

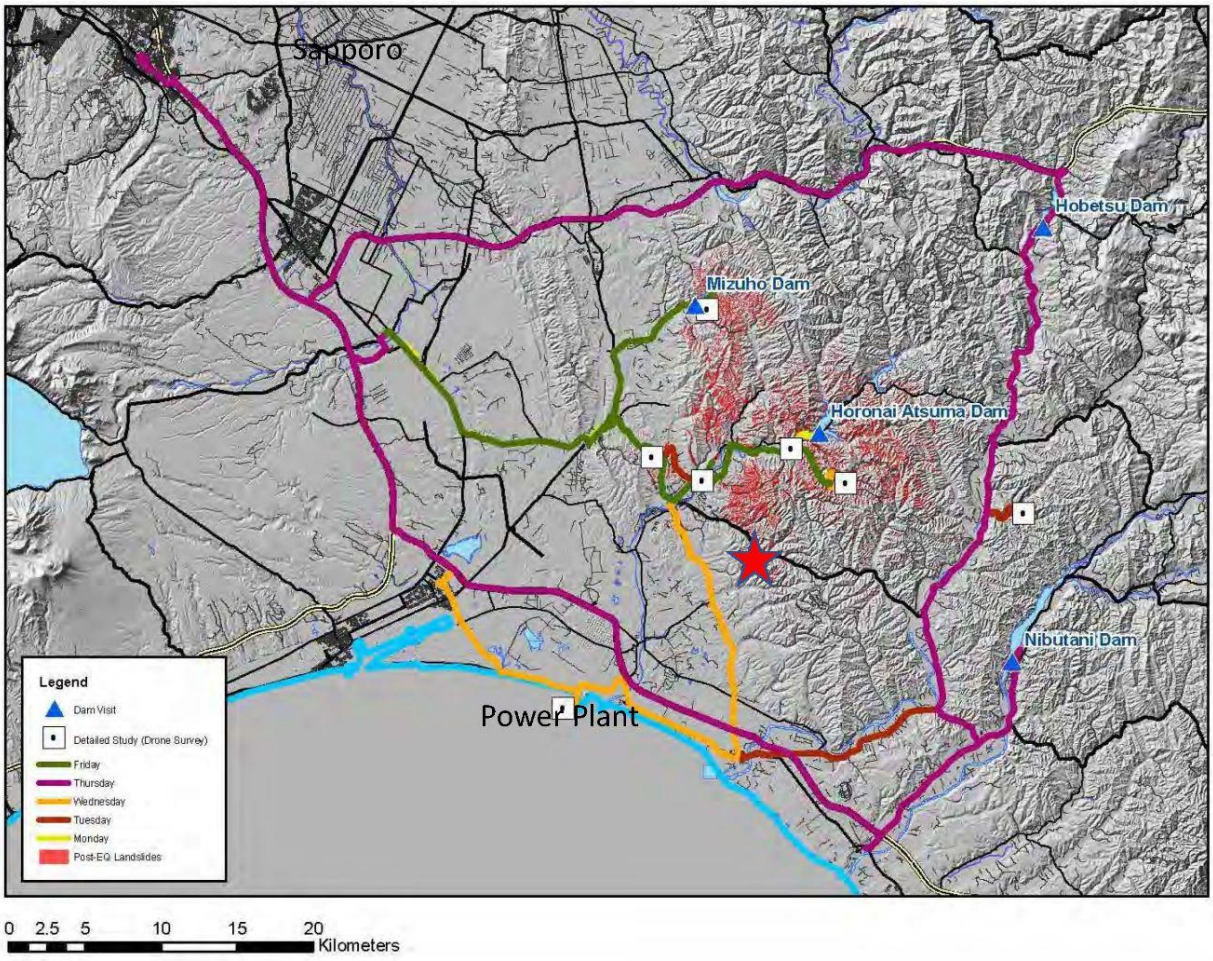

Figure 7-1. Locations of Hokkaido Dams and Dams visited by PG&E/SCE/Infraterra team and reconnaissance track logs (Japan Dam Database: http://maps.ontarget.cc/dams/en.html#!id=0164)

Figure 7-2 compares the variation between ground motions recorded at the base and crest of the embankment/rockfill Hobetsu and Mizuho Dams relative to those documented for California dams from past earthquakes (Harder, 1993).

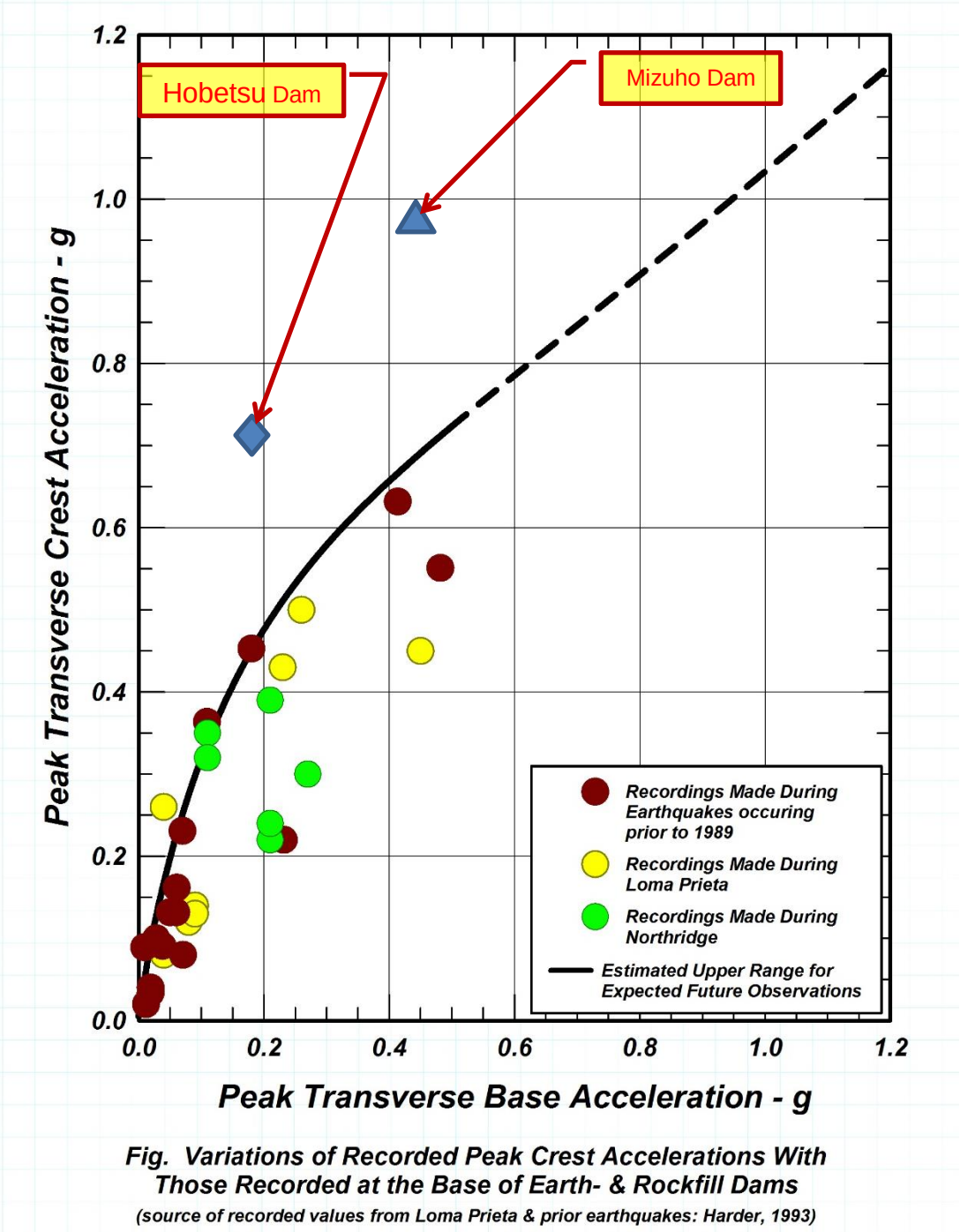

Figure 7-2. Base acceleration versus crest acceleration of various dams. Developed by I.M. Idriss.

It should be noted that all 4 dams visited by the team in Hokkaido represent modern dams built after 1985, and only minor or no damage was observed. The recent vintage of the dams was a key aspect of the good performance of the dams, as they appeared to be well-designed structures with favorable details including conservative dimensions, good concrete or well compacted embankment fills, and

apparent positive drainage control. These dams had significantly better elastic performance than example older California dams evaluated by Harder (1993) with corresponding greater crest motions. Figure 2 shows that estimating seismic dam response using the historical Harder chart may be unconservative for evaluation of modern and well-built dams.

Additional details from the visits and discussions with local dam engineers for Nibutani, Hobetsu, and Mizuho dams are provided in the following report sections.

7.2 Dam Performance - Hobetsu Dam

The PG&E/SCE reconnaissance team visited Hobetsu Dam (http://damnet.or.jp/cgi-bin/binranA/enAll.cgi?db4=0114) on October 25, 2018. The dam located near the town of Mukawa in Hokkaido Prefecture (Lat/Long: 42.885648, 142.179387, Google Map: https://goo.gl/maps/1cNqL2Qhgrq).

Mizuho Dam is a 38 m high embankment dam with a crest length of 283 m and a total dam volume of 529,000 m^3 (http://damnet.or.jp/cgi-bin/binranA/enAll.cgi?db4=0114). The main purpose of the dam is for agriculture and irrigation and has a storage capacity about 10,330 m^3. Construction of the dam started in 1970 and the dam was completed in 1985.

The upstream shell is rockfill with a slope of 3.32:1 (H:V) over the upper portion and 4:1 over the lower portion. There is a 5 m wide bench at the slope transition, 23.4 m below the dam crest. The downstream shell is earthfill, with a slope of 2.25:1 (H:V) and 4 m wide benches at 8.9 m, 18.9 m, and 28.9 m below the dam crest. The dam has a low-permeability core that extends from just below the dam crest down to a core trench, with upstream and downstream filter zones. At the right abutment there is a concrete spillway oriented perpendicular to the axis of the dam. A concrete spillway channel runs along the right abutment.

An operational crew was present at the time of the visit, and provided information on the peak recorded ground motions at the site by instruments at the base and crest. During the event, the peak ground acceleration recorded at the dam base and crest were 224 gals and 706 gals, respectively. Despite the significant amplification of ground motion (over a factor of three) no damage was reported, which was supported by the team's observations.

There were no signs of deformation or bulging on the upstream or downstream slopes, and no obvious cracking of the downstream fill. A network of concrete surface drains run across the downstream slope dam to collect runoff. These drains would likely be vulnerable to relative deformation of the slope, but there were no signs of damage or distortion. Similarly, there was no observed damage to the spillway control structure or channel. The only potential impact observed was fresh crack (approximately ¼ inch wide) in the pavement at the crest near the contact between the right abutment and the spillway channel. There was no visible separation between the dam and spillway channel.

No landslides were observed around the dam or reservoir. Based on post-earthquake satellite and aerial images reported by PASCO (https://www.pasco.co.jp/disaster_info/20180906/), the dam is located outside the zone of extensive areal wide landslides experienced during the earthquake.

Figure 7-3. Downstream view of Hobetsu Dam from right abutment (Image from the Japan Dam Foundation http://damnet.or.jp/cgi-bin/binran/enPAL.cgi?idm=9645). 42.885648, 142.179387,

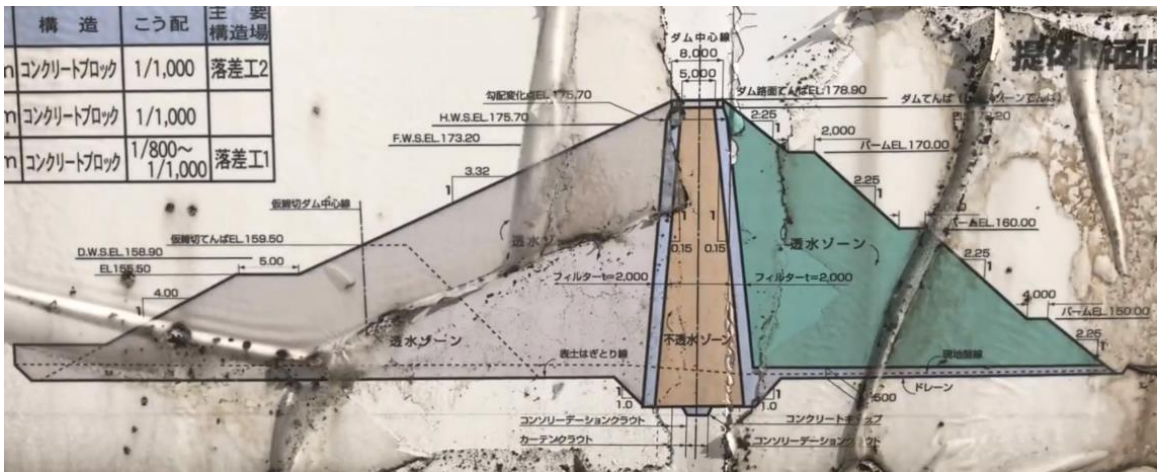

Figure 7-4. Section drawing of Hobetsu Dam posted onsite.

Figure 7-5. Plan drawing of Hobetsu Dam posted onsite. 42.885648, 142.179387,

Figure 7-6. Upstream view of Hobetsu Dam from right abutment. 42.885648, 142.179387,

Figure 7-7. Hobetsu Dam Spillway.

Figure 7-8. Surface drain on downstream slope of Hobetsu Dam. No damage or deformation of the drains was observed. 42.885648, 142.179387,

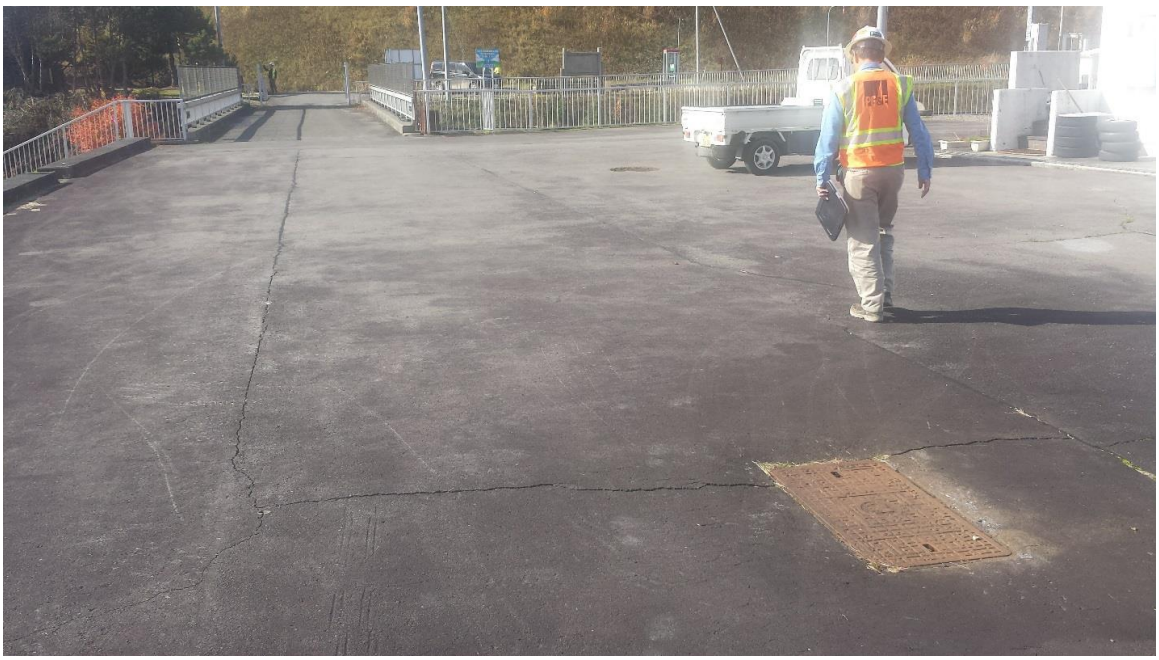

Figure 7-9. Fresh crack in crest pavement noted near contact between right abutment and spillway channel. 42.885648, 142.179387,

7.3 Dam Performance - Nibutani Dam

The PG&E/SCE reconnaissance team visited the Nibutani Dam, a concrete dam (二風谷ダム *Nibutani-damu*) site on October 25, 2018 (https://good-hokkaido.info/lake-nibutani/). The dam is located on the Saru River in Hokkaidō, Japan, which stands at Nibutani in Biratori town, Saru District (Lat/Long: 42.629302, 142.148654, Google Map: https://goo.gl/maps/84citypjSs42).

The dam is 32 meters high and 550 meters long concrete gravity dam with a storage capacity of $17X10^6$ m^3. Spillway capacity is 5,000 m^3/sec through 12 gated spillway chutes and a sish ladder is constructed near the right side of the dam. Work on the dam began in 1990 and was completed in March 1997, despite objections from the local Ainu people.

When the team visited the dam site, we were able to communicate with the onsite dam operation crew and they kindly pulled the instrumented strong ground motion record at the dam site for us. They also briefed us of their emergency response procedures after the earthquake. Ground motion recorded during the earthquake was 158 gal at the base of the dam and 206 gal at the dam crest. The onsite crew immediately inspected the dam after the earthquake and another round of inspection was made 3 hours later. We were informed that the dam suffered no damage and leakage did not increase after the event. No mal-function of gates operation were reported either. There was no emergency drawdown performed after the earthquake.

We were not allowed to walk on the dam body. Our inspection mainly focused around the left abutment where grading was made to create a level area for the operational center and the parking area. We expect some fill were placed to create this level area especially near the dam where a bridge was built to connect the operation center to the dam. Minor damage related to the fill compaction and/or differential settlement was observed most along the paved driveway leading to the bridge connect the

abutment to the dam. There was a 5-ft by 5-ft wide sinkhole covered with tarp near the abutment bridge contact. The intensity of the shaking was also demonstrated by the damaged handrail supported in concrete and the wood fence along the edge of the abutment slope.

Figure 7-10. Downstream view of the Nibutani Dam from upstream right abutment 42.629302, 142.148654.

Figure 7-11. Upstream view of Nibutani Dam from left abutment 42.629302, 142.148654.

Figure 7-12. Downstream view of Nibutani Dam from left abutment 42.629302, 142.148654.

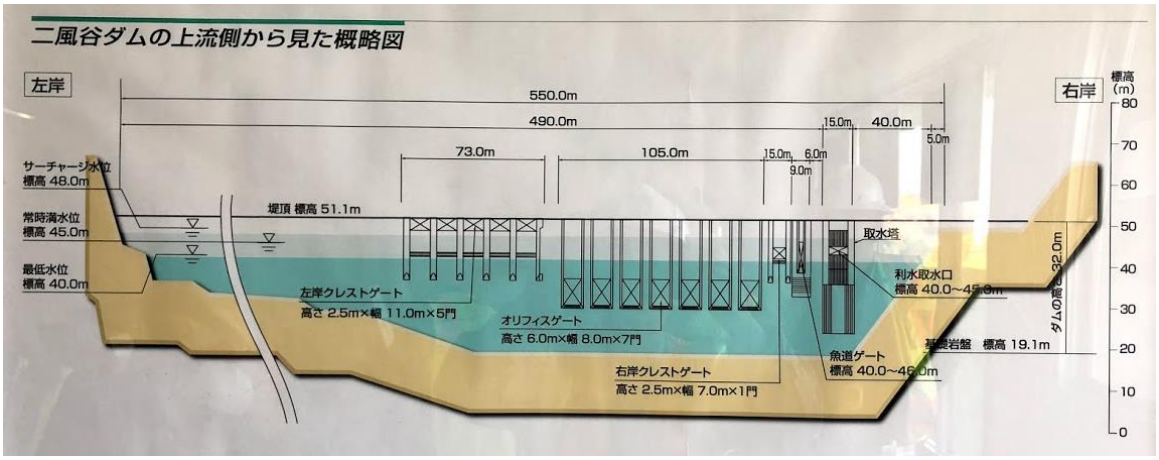

Figure 7-13. Longitudinal profile of Nibutani Dam

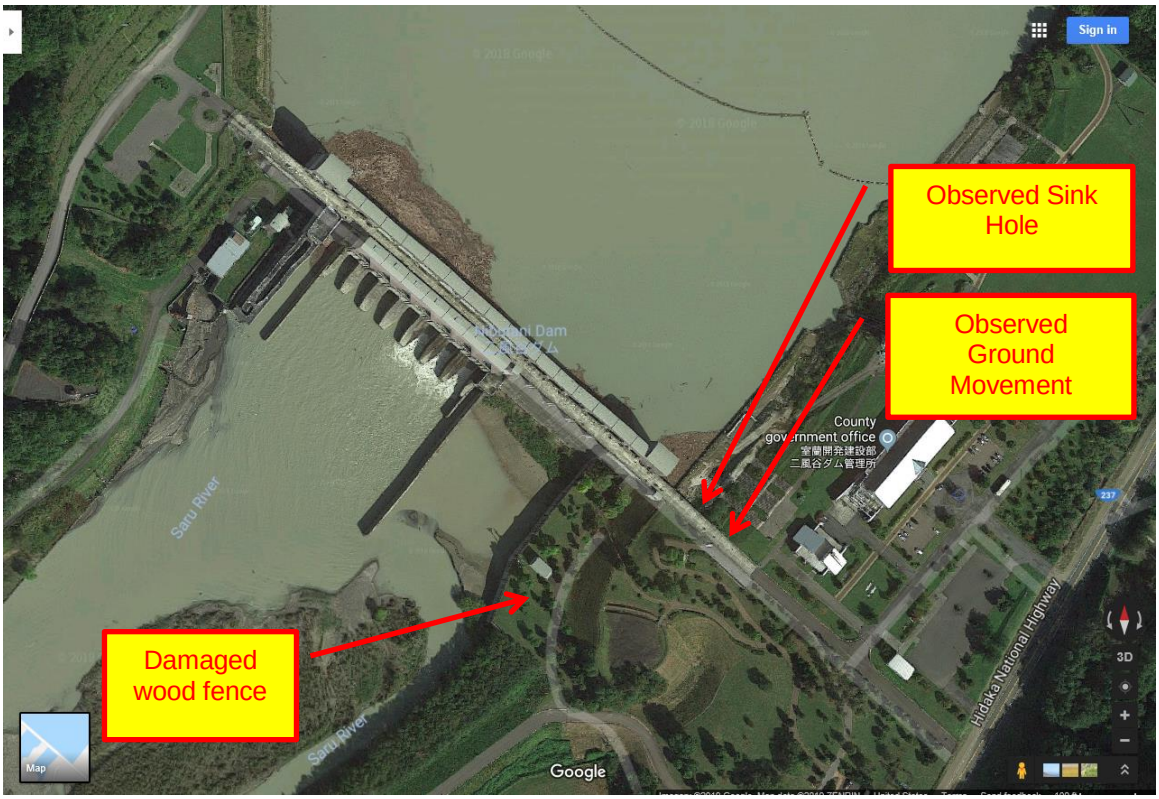

Figure 7-14. Plan view of Nibutani Dam and location of observed damage

Figure 7-15. Differential settlement of bridge approach and adjacent fill area 42.629302, 142.148654

Figure 7-16. No damage to the deep foundation support bridge deck connect to the gates 42.629302, 142.148654

Figure 7-17. Differential settlement of the fill area 42.629302, 142.148654

Figure 7-18. Separation of the concrete pavement 42.629302, 142.148654

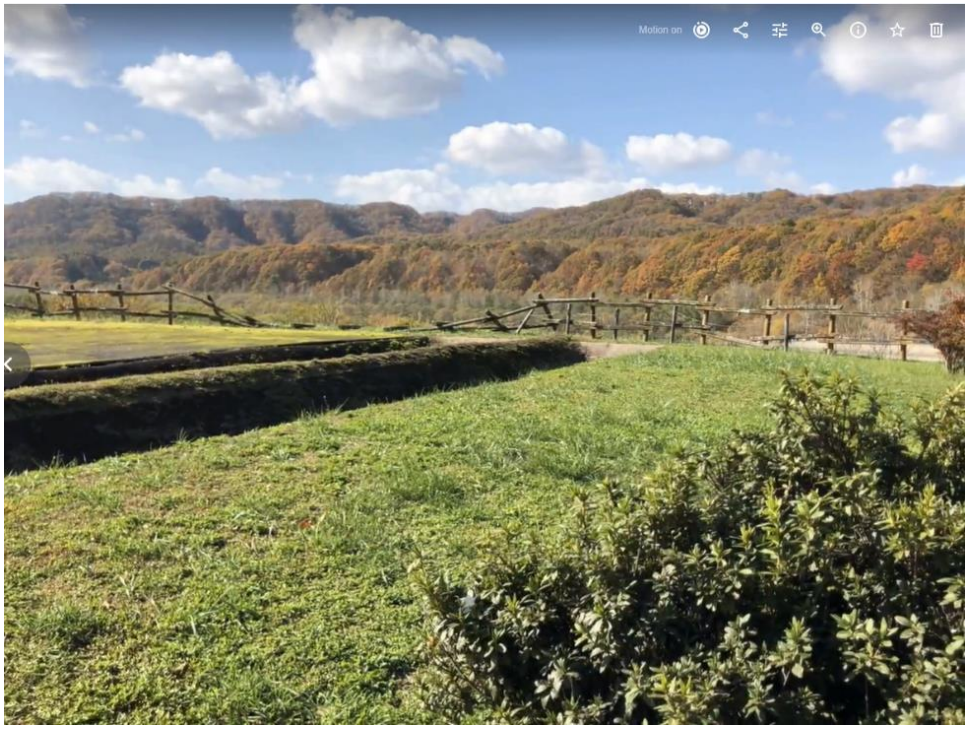

Figure 7-19. Collapse of wood fence near left abutment 42.629302, 142.148654

Figure 7-20. Damage of hand rail 42.629302, 142.148654

Figure 7-21. Sink hole near abutment bridge contact 42.629302, 142.148654

8.0 Performance Of Lifelines

Seismically induced damage to lifeline systems occurred in many observed locations. Previously discussed in this report include significant damage to roadways due to landsliding (Section 5), liquefaction damage to port facilities (Section 7), detrimental damage to a water treatment facility (Section 5.4), electric power tower damage due to deep-seated landsliding (Section 5.6) and extensive damage to buried water, wastewater, and other utilities in Satozuka due to liquefied ground movements (Section 6.4).

8.1 Transportation And Electrical Systems

Damage to roadways due to landsliding and cracked pavement was widespread throughout the region. Many areas remained inaccessible to the team due to closures and associated repairs. Several major throughways in the Atsuma region were wiped out by landslides, circumvented only by dirt farming roads between fields and along river levees. Self-defense force troops, police, firefighters and other workers totaling 40,000 participated in the recovery effort.

All flights to New Chitose Airport, located 24 km northwest of the epicenter, were cancelled on the day of the quake. Airport operation, however, were resumed midday the following day. Subway and tram operators in Sapporo reduced service frequency immediately follow the quake, returning to normal operation after two weeks of inspections and power conservation.

Approximately 13,000 people were reported to be evacuated to 768 evacuation facilities. Due to power loss and traffic it took some residents more than 24 hours to reach shelters. Approximately 2500 and 652 people remained in evacuation centers as of 9/10 and 9/24, respectively.

8.2 Electric Power

As a result of the earthquake nearly 5.3 million residents, the population of Hokkaido Prefecture, lost electrical power service. The widespread outage was a result of damage to the Tomato-Atsuma coal-fired thermal power plant, owned and operated by Japan's Hokkaido Electric Power Company (HEPCO), the largest in Hokkaido. The power station is located 10 km east of port city Tomakomai and 13 km southwest of the September 6th epicenter (Figure 1-1).

When fully operational the coal-fired plant has a capacity of 1.65 million kw, about half of the electricity needed during peak demand for the Hokkaido area at the time of the quake (approximately 3.8 million kW). The utility has the capacity to provide a maximum of 5.2 million kw to the prefecture.

8.2.1 Power Generation Damage

The Tomato Atsuma Power Plant includes three primary units, listed in Table 8-1. HEPCO reports indicate that the September 6th event caused steam leaks in units No. 1 and No. 2 as well as a fire in the vicinity of the turbine of No. 4 (HEPCO 2018). The plant is located on reclaimed land at the Eastern side of the port. Soil liquefaction was observed, damaging roads in and around the power plant and coal yard as well as the seawall at the southern end of the plant, but thought to have marginal implications for power generation relative to the reported internal damages.

In response to the quake, the Tomato Atsuma Power Plant underwent emergency shutdown procedures. This shutdown resulted in an imbalance of grid power supply-demand and frequency

disruption, causing emergency relays to trip at plants and key distribution points across Hokkaido. All 2.95 million households across the island experienced electric power service interruption due to this progressive emergency shutdown.

8.2.2 Power Plant Recovery

In response, HEPCO immediately restarted a 300 MW hydroelectric power plant and quickly brought online the 250 MW Sunagawa Power Station (coal). By 6:30 p.m. JST on the day of the earthquake, power was restored to 340,000 households in Hokkaido. HEPCO followed by bringing online the following thermal power plants: Naie Power Station (350 MW-coal); Date Power Station (700 MW-oil); Shiriuchi Power Plant (700 MW- oil); Onbetsu (280 MW – Diesel), altogether providing 2900 MW supply capacity. Table 8-2 provides an overview of thermal power plant status on 6 September and recovery during the days immediately following.

On September 8th the Japan's Minister of Economy, Trade, and Industry asked all residents of Hokkaido to reduce power consumption by 20% during the hours of 8 AM to 8:30 PM to reduce the need of implementing rolling blackouts due to demand greater than supply. Despite only achieving a electricity conservation rate of 15.4% the central government was able to hold off implementing rolling blackouts. The call for a targeted power reduction was relaxed by the Minister on September 14 as the power supply reached robust capacity.

To make up for needed demand HEPCO also accepted power from other suppliers, employing the Kitamoto intercontinental line. The power generation response curve is provide in Figure 8-1 showing the number of households without power following the quake and restart of various power generation facilities. In areas that experiences prolonged outage HEPCO deployed power supply vehicles to hospitals and other important facilities. The Tomari Nuclear Power Plant (2,070 MW), the only nuclear power facility in Hokkaido, was shut down for maintenance at the time of the earthquake and was not involved in the recovery effort.

On September 11th power was restored to all residents except for about 196 houses in the most heavily damaged areas that could not be entered. As of September 16th the blackout continued to affect 59 homes in the towns of Abira and Atsuma.

Table 8-1. Tomato-Atsuma coal-fired power plant units and return periods (HEPCO 2018)

Unit Number	Status during Earthquake	Reported Damage	Major Repairs	Recovery Date	Capacity (MW)
No. 1	In operation→ Stop	Steam leaks	Replaced 2 damaged boiler tubes	9/19 9:00	350
No. 2	In operation→ Stop	Steam leaks	Damage repair of 12 boiler tubes and 2 pulverizing coal machines	10/10 6:00	600
No. 4	In operation→ Stop	Fire & turbine failure	Repair and inspection of damaged ends of main turbines, Eccentricity correction of the main turbine shaft	9/25 3:00	700

* Unit 3 was decommissioned in 2005

Table 8-2. Hokkaido thermal power station situation immediately following earthquake (HEPCO 2018)

Unit	Status during earthquake	Main measures up to parallel	Recovered date and time	output (MW)	Supply power[*1] (MW)
Sunagawa Unit 3	Balanced stop	Start up at the shortest time after receiving power	9/6 13:35	125	125
Onbetsu Unit 1	Balanced stop	Start up at the shortest time after receiving power	9/6 20:10	74	199
Naie Unit 2	During startup	Start up at the shortest time after receiving power	9/7 0:20	175	374
Sunagawa Unit 4	Balanced stop	Turning start / eccentricity correction accompanying main turbine turning stop after receiving electricity	9/7 0:57	125	499
Shiriuchi Unit 1	Operation→ Stop	Start up at the shortest time after receiving power	9/7 3:45	350	849
Naie Unit 1	Operation→ Stop	Damage repair of the atmospheric discharge plate	9/7 4:24	175	1,024
Onbetsu Unit 2 [*2]	Balanced stop	Reset start sequence of air compressor after power reception, limit adjustment of high pressure bleed valve, start according to supply and demand	9/7 9:08	74	1,024[*3]
Date Unit 1	Balanced stop	Hydrogen release in the generator due to stoppage of the emergency generator, hydrogen replacement / boost after receiving power	9/7 11:18	350	1,374
Date Unit 2	Operation→ Stop	Hydrogen release in the generator accompanying stoppage of emergency generator, hydrogen replacement / boost after power reception, turning on/off eccentricity correction due to main turbine turning off (time difference of about 7 hours after Unit 1 parallel is necessary due to limit of capacity of starting transformer required)	9/7 19:18	350	1,724

The Mori Power Station (geothermal energy, 25,000 kW) recovered at 3:04 on 9/7

[1] Cumulative power supply of thermal power supply resumed operation

[2] On September 11, due to large shaft vibration, it is stopped (restoration method under consideration)

[3] Onbetsu No. 1 is stopped from 6:36 on September 7th to September 11th 16:07 due to oil leakage from the lubricating oil cooler, so it is deducted from supply power

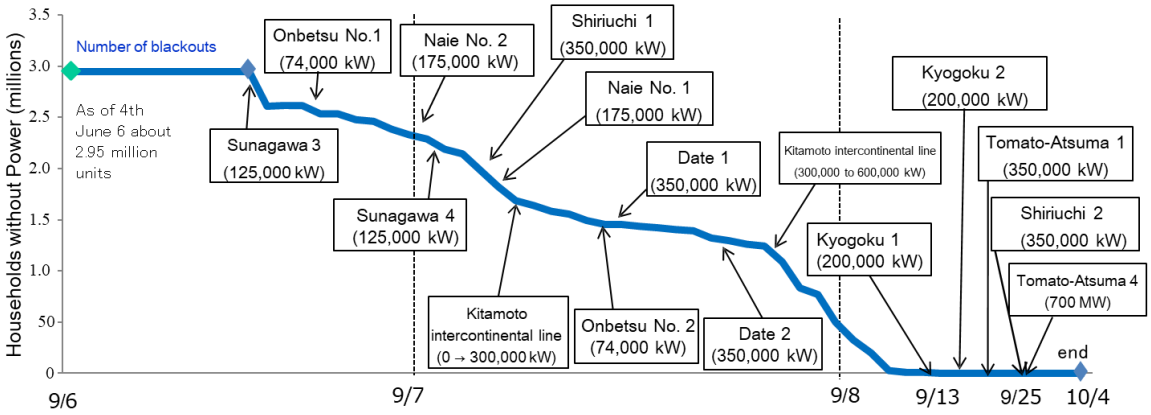

Figure 8-1. Households without power vs. time following 9/6 earthquake and progression of thermal power plant restart (HEPCO, 2018)

8.2.3 Power Equipment Damage

In addition to power plant damage, electric power recovery was also hindered by power transmission and distribution equipment damage. Transmission towers were impacted to various degrees by landsliding. In addition to locations discussed previously in Section 5.6, Figure 8-2a shows an example of successful performance of a transmission tower positioned at the crown of a landslide which induced 20-40 cm at the tower foundation (no indication of tilting or translation) while Figure 8.2b shows images of a tower collapse due to translational movement. The following lists transmission tower damages reported by HEPCO (2018).

- Two steel transmission towers in the Yufutsu District of Mukawa carrying the Iwachishi Line (66 kV) (Tower No. 71 and No. 107) collapsed due to landsliding.
- The 275 kV Southern Higashi Line 1 (Eastern Route 1) suffered lead wire disconnection, requiring repair.
- The Shinhoku Line (66 kV) wire disconnected
- Hunkatsu trunk line (275 kV): Collapse around the transmission line
- Bucheon Line (66 kV): tree contact
- Transmission tower No. 52 on the Karikachi Line (275 kv): repair by mid-November

Distribution equipment suffered widespread damage. HEPCO reported on 10/5 a total of 1,095 damages to utility poles and other distribution support equipment including breakage (44), tilt (787), collapse (20), and foundation damage (244). High-voltage line damage included 56 breaks and 105 instances of crossing lines. Transforms suffered 57 incidents of damage and 1,422 incidents of inclination.

Additional study of power system response and recovery is warranted. Following up with Hokkaido Electric Power Co. officials after repairs are fully under control and their availability allows is valuable. Detailing the specific chain of events that lead to island wide outage and assessing both poor and successful performance of individual system components distributed across the highest impacted region is of significant interest.

Figure 8-2. Electric power tower (a) at top of translational slide (Cow Slide) with no observable damage to foundation elements. Settlements at concrete footings range from 20-40 cm. (b) collapsed Iwachishi Line (66 kV) (November, 1, 2018 HEPCO report)

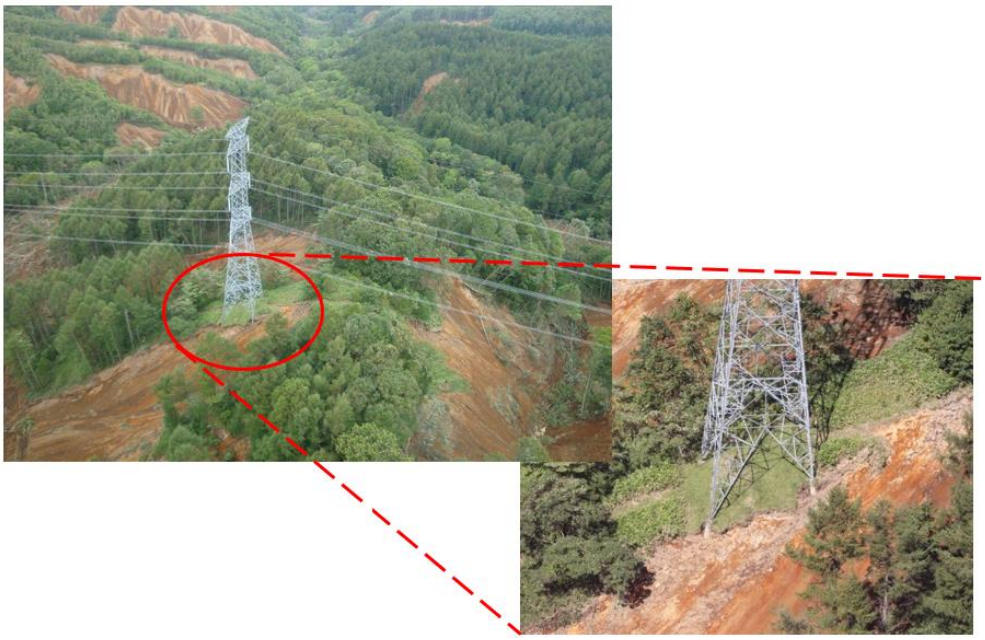

Figure 8-3. High capacity electic transmission tower narrowly avoiding significant damage due to nearby landsliding (Source: http://wwwa.hepco.co.jp/pdf/18091601.pdf)

8.3 Water Supply

Disruption of water service occurred in several areas due to earthquake. Significant occurrences of damage with regard to water system performance include: (1) the Atsuma water purification facility, which was heavily damaged by landsliding (Section 5.4), and (2) pipe damage and associated outages in Satozuka, Sapporo City resulting from significant ground settlement and liquefaction (Section 6.4).

An 11 September 2018 article reports about 5,000 households in Atsuma and Abira remained without water service at the time of publishing, 5 days following the earthquake (Asashi Shimbun, 2018, http://www.asahi.com/ajw/articles/AJ201809110026.html).

8.4 Estimated Economic Losses:

Estimates of direct and indirect damages due to the earthquake and typhoon are provided below. These are initial estimates provided by the referenced media outlets. The estimates may be inaccurate/skewed but do provide some perspective as to the large impact to the region.

- Direct damages alone, including those attributed to roads, rivers and forest land, are estimated to exceed 150 billion yen (US$1.8 billion). [The Straight Times (2018) https://www.straitstimes.com/asia/east-asia/swift-assistance-needed-to-rehabilitate-hokkaidos-quake-stricken-industries-the]
- Losses associated with agriculture, forestry and fisheries industries in Hokkaido - the main industrial economic drivers in the area - including damage caused to agricultural facilities, irrigation and drainage canals are estimated to exceed 42 billion yen. [The Straight Times (2018)]
- Losses to the tourism industry, another significant economic driver in the region, were also reported. They include cancellations of reserved accommodations for 940,000 people and reservations for 4,000 sightseeing buses. Among other things, cancellations of large-scale school excursions may have been a heavy blow. The loss of profits tied to accommodations, as well as at eating and drinking establishments, are estimated to reach a total of 29.2 billion yen. [The Straight Times (2018)]
- Outages caused closure of production plants including Toyota for several days. [Al Jazeera (2018) https://www.aljazeera.com/news/2018/09/death-toll-rises-earthquake-japan-hokkaido-island-180910073306436.html]
- Almost all public schools in Hokkaido resumed classes on Sept. 10, with less than 10 percent of all schools still closed. [The Asashi Shimbun (2018) http://www.asahi.com/ajw/articles/AJ201809110026.html]

9.0 Remote Sensing Methods

9.1 Light Detection And Ranging (LiDAR)

The terrestrial LIDAR technique (3D laser scanning) consists of sending and receiving laser pulses to build a point file of three-dimensional coordinates of the scanned surface. The time of travel for a single pulse reflection is measured along a known trajectory such that the distance from the laser, and consequently the position of a point of interest, is computed. Using this methodology, data collection occurs at rates of thousands of points per second generating a "point cloud" of three-dimensional coordinates.

A total of 7 terrestrial lidar scanning (TLS) sites were developed during our reconnaissance (Figure 9.1) over a total of 74 individual scans. TLS data were collected using a Maptek I-Site XR3 lidar scanner capable of a maximum range of ~2.4km. Data were collected to a maximum range of ~1.6km in this reconnaissance. Scans were typically collected at a nominal point spacing of 43mm at 100m, to facilitate coverage of several sites over highly detailed scanning of individual features. Most scans collected in this reconnaissance were of features within 25m of the scanner (e.g., liquefaction damage, roadways, and near landslides). Ground control was established from the XR3 internal GPS. Therefore, precise measurements from these data may be more uncertain than a traditional survey-grade lidar collection effect. Individual lidar scans were merged into a composite point cloud using Maptek's I-suite software. Resultant merged point cloud models, and raw data as .e57 and .las files, are available via DesignSafe. Users should note noise due to passing vehicles or individuals, incidental returns from rain, or other spurious points have not been removed to provide raw and unaltered data to those wishing to perform their own registration or analyses. Secondary lidar scanning data were collected using a Leica BLK360 short range scanner at the Tomakomai Port facility in parallel with our standard XR3 scans. BLK360 data are also available in raw and processed formats at DesignSafe.

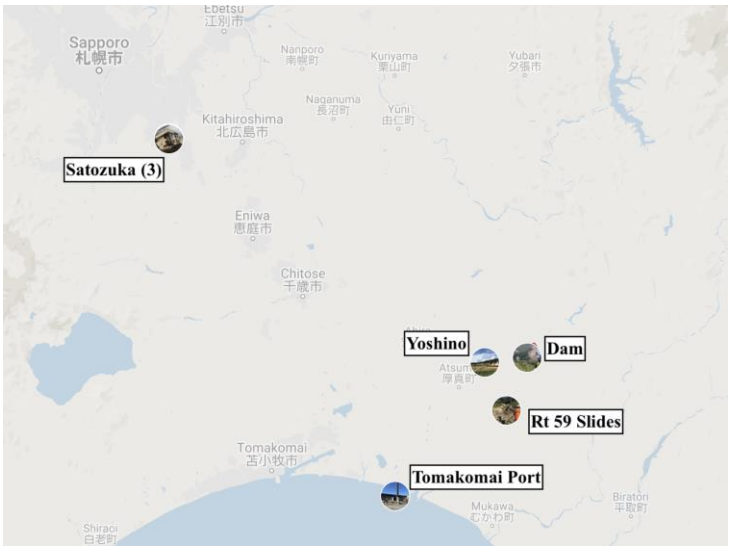

Figure 9-1. Map of the epicentral region showing locations of each terrestrial lidar scan location. The three sets of scans at Satozuka have been merged into a single model following reconnaissance effort.

Table 9-1. Summary of terrestrial lidar scans and developed point cloud models from the GEER reconnaissance. All models and data can be found at 'Designsafe'.

Name (ID)	# of Scans	Key Features	Notes	Extent (km^2)
Yoshino (1)	6	Extensive landslides, multiple buried homes	Test of scanner range (normal-speed) and resolution (8), distant landslides at 1.6km. Active work zone, multiple heavy machinery rigs moving during scans in landslide toe	1.68
Dam (2)	3	Large volume landslides next to a dam abutment	Incomplete coverage due to limited sightlines, single scan location	0.35
Satozuka (3)	38	Extensive liquefaction and significant damage to structures, lifelines. Multiple homes askew.	Large compilation of scans collected over 3 days. Highly variable lighting conditions for lower portion (downslope) of scans. Active work zone, many moving vehicles / people throughout	0.04
Tomakomai Port (4)	13	Minor liquefaction settlement and damage to port facilities	Comparison Scans with BLK360, data includes noise from through going large truck traffic within the port facility	0.01
Rt 59 Slides (5)	14	Large landslide with well preserved soil stratigraphy, one of three slides scanned has a large 3D flow	Upper portions of flow slide missing due to inaccessibility, runout zone for all three landslides had been reworked, large earthen embankment was installed	0.11

Summary images and a brief summary of each TLS model are described below.

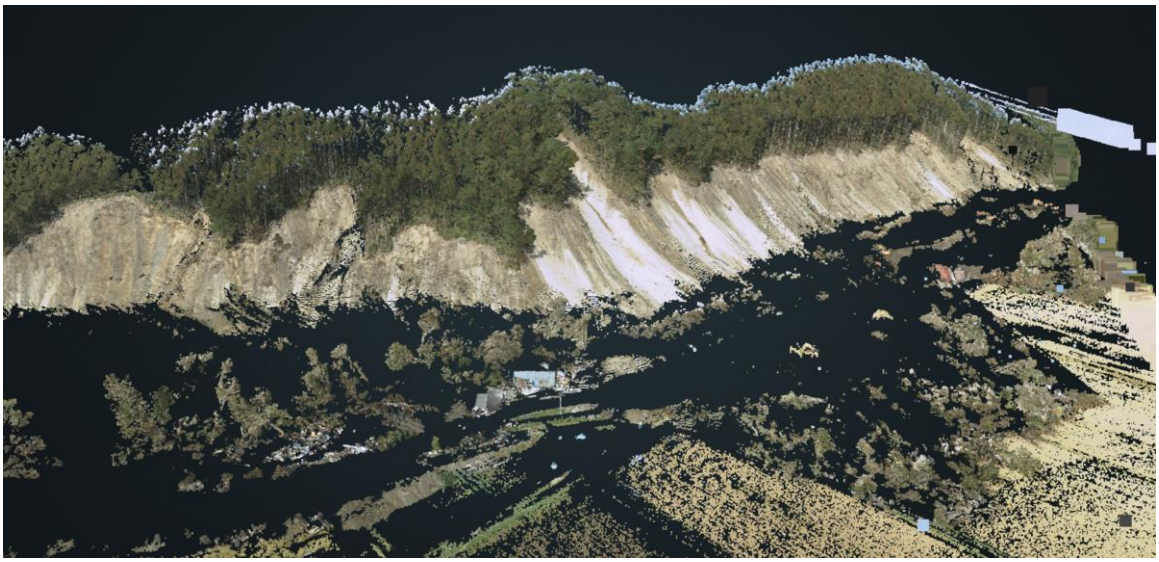

Figure 9-2. Yoshino Landslides. Six merged long range (0.5 – 1.6km) scans collected from two vantagepoints towards the highly destructive Yoshino landslide complex. Many buried homes observed but poorly constrained by data below landslide deposits. Large data gaps (dark zones at toe of slides) due to poor vantage points and active construction along the entire site to rebuild the roadway and clear debris.

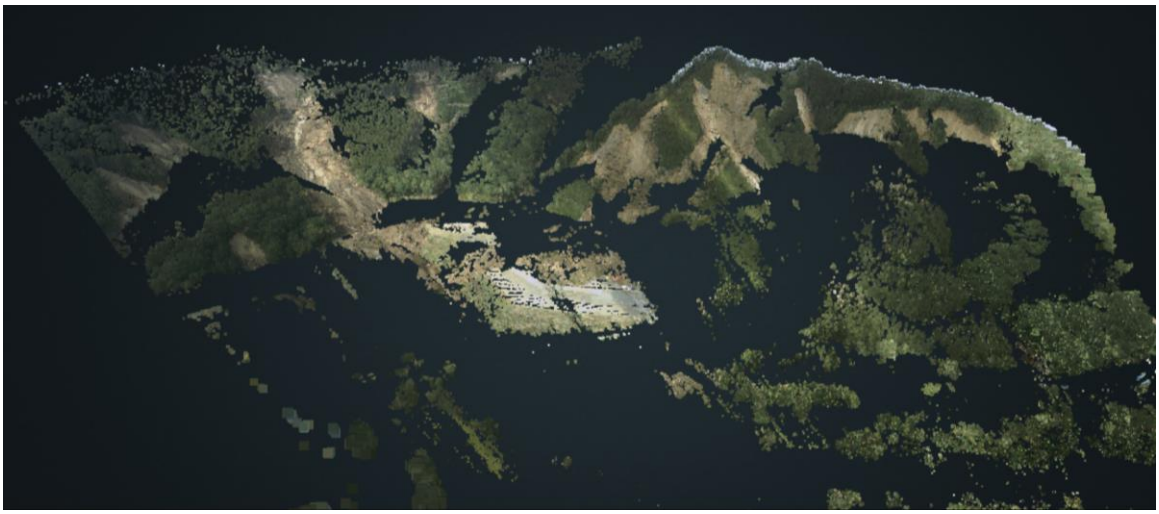

Figure 9-3. Point cloud data for the dam abutment landslides. Limited vantage-points limited the coverage of scans at this location but overall landslide behavior is preserved.

Figure 9-4. East Port of Tomakomai lidar scan. Note multiple noise chirps due to passing trucks along the active port facility road. Scans preserve small vertical settlements along light-post and adjacent structures (left) as well as minor roadway cracks due to liquefaction.

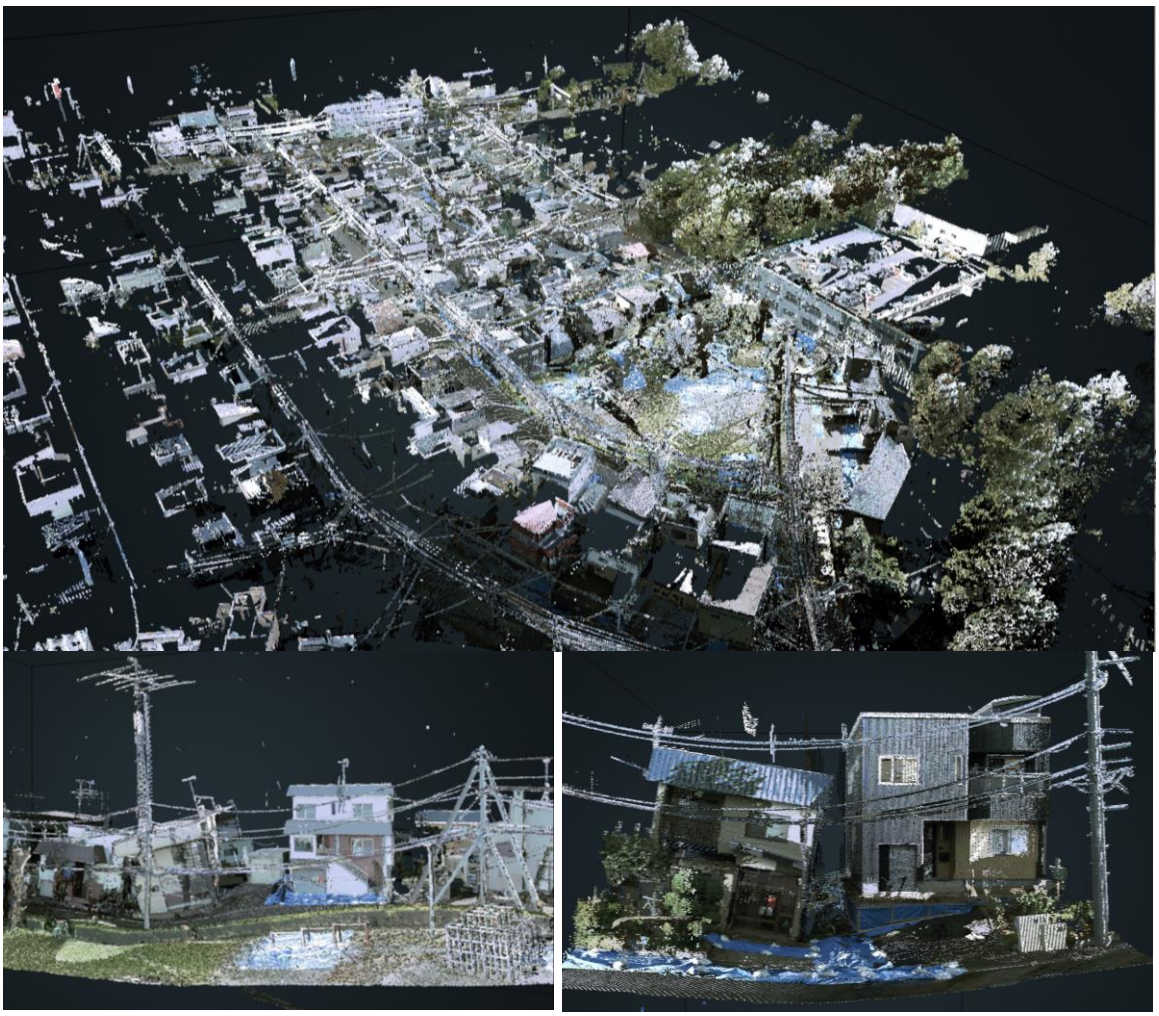

Figure 9-5. Scans collected from Satozuka. top, overview of the complete model from 38 individual TLS scans, flow-failure runs from upper left to lower right along the zone of highest data density. Bottom, example sections from within the data showing damaged and undamaged structures.

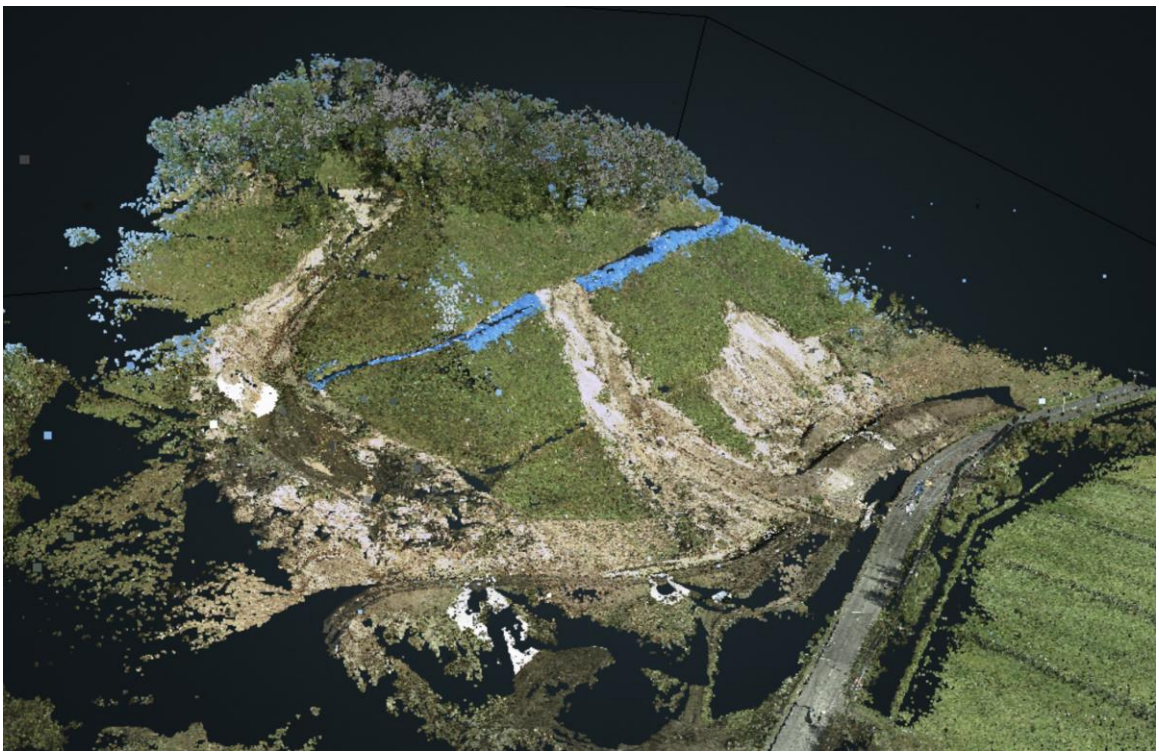

Figure 9-6. Route 59 landslides TLS scans. Three large landslides observed at this site, including one that turns sharply mid-runout. Landslide deposits had been considerably reworked but likely impacted highway below. Adjacent unfailed deposits clearly showed the layered pumice-organic soil mantle involved in nearly all landslides observed during our reconnaissance.

9.2 Structure-From-Motion

An unmanned aerial vehicle (UAV) was used to capture low-altitude aerial imagery from select sites of interest during the Hokkaido reconnaissance. The UAV used to collect the data for this mission was a small, custom made quadcopter that has been configured for collecting low-level aerial images.

The UAV was equipped with fully autonomous mapping capability that allows for pre-programmed flight. The airframe is a Mavic Pro model manufactured by DJI with dimensions. This small aircraft footprint made it ideal for transport to various sights of interest and flying near damaged structures without the risk of causing significant damage or harm in the event of a malfunction.

The UAV was equipped with a fully autonomous 3D autopilot that is capable of flying an entire mission with little or no operator input. The operator was able to monitor the UAV from the ground using a wireless telemetry link connected to a laptop computer. This telemetry link showed the real-time GPS location of the UAV as well as critical flight instruments such as heading, velocity, and artificial horizon. Along with the telemetry link, the operator maintained a separate radio control link at all times. The operator was also equipped with a wireless video down link so the damage visible from the air could be monitored from the ground using first-person view (FPV) goggles in real-time. In the rare event of a loss of communications, the UAV would autonomously return to its starting location and land.

The sensor used to gather the aerial images for this mission was a built-in 20 mega-pixel camera. The camera was mounted on a two axis, stabilized gimbal on the UAV that allowed for minimal motion blur cause by the attitude changes of the aircraft. The camera was also able to be tilted on its elevation axis by the operator on the ground. The image the camera was viewing could also be viewed in real-time by both the operator and geotechnical experts so the UAV could be guided manually to localized earthquake damage. Flights were performed over approximately 10^2km of the study area. No ground control points were surveyed for any of the flights to simplify field operations.

Three-dimensional point cloud and textured models were developed from the aerial images captured with the camera. Structure from Motion (SfM) computer vision technology was used to develop the 3D models. All SfM image processing was performed using the commercial 3D visualization software *PhotoScan 1.1.5 and Context Capture from Bentley Software*. Finalized dense point clouds were exported and were scaled, edited, and analyzed in point cloud manipulation software *CloudCompare 2.6.1* and Maptek *I-Site Studio 7*.

9.3 Geotagged Datasets

During the reconnaissance, vehicles were used to traverse the roads of the epicentral region. Each vehicle was equipped with smartphones, digital cameras, maps, computers for recording site logs, and GPS units for recording track logs and site locations. The reconnaissance team merged the GPS data, site logs, and digital photos into a common database. Following the reconnaissance, a Google Earth KML file was generated to display the observations on dynamic digital maps. The authors recommend downloading and opening the Google Earth map file for this earthquake, shown in Figure 9-7, to navigate through the report observation sites as they are described in the text.

The primary tools of the reconnaissance effort were smartphone (iPhones and Android) devices that are essentially handheld computers, phones, cameras, GPS units, and dictation devices. These devices integrate all the basic functions that were previously done on multiple pieces of equipment. Text messaging proved to be the preferred means of communication during the reconnaissance. Phones required external power to operate all day during the reconnaissance, provided by car adapters and an external power battery charged before the reconnaissance.

For the reconnaissance, all recorded information, photographs, and data observations were located with latitude and longitude coordinates. GPS track logs passively monitored the locations of travel of each reconnaissance team vehicle during the field day. All observations were recorded and reported as ellipsoid heights in the World Geodetic System of 1984 (WGS84).

Figure 9-7. Map showing the locations and data extent of TLS and UAV data collected during this GEER reconnaissance. This map and links to the data represented here are available at: https://drive.google.com/open?id=1rK_A-V_SH_S62tSGDVEl_vbE9SNnqYy8&usp=sharing

References

Abrahamson, N.A., Gregor, N., Addo, K. (2016). BC Hydro ground motion prediction equations for subduction earthquakes, Earthquake Spectra, 32: 23–44.

Abrahamson, N.A., Kuehn, N., Gulerce, Z., Gregor, N., Bozorgnia, Y., Parker, G. Stewart, J.P., Chiou, B., Idriss, I.M., Campbell, K., Youngs, R. (2018). Update of the BC Hydro Subduction Ground-Motion Model using theNGA-Subduction Dataset. Pacific Earthquake Engineering Research (PEER) Center Report 2018/02.

Arai, F. (1986). Catalog for late quaternary marker-tephras in japan ii: tephras occurring in northeast honshu and hokkaido. *Geographical Reports of Tokyo Metropolitan University, 21*, 223-250.

Boore, D.M. (2010). Orientation-independent, non geometric-mean measures of seismic intensity from two horizontal components of motion, Bulletin of the Seismological Society of America, 100, 1830–1835.

Death toll from Hokkaido quake reaches 41 as last missing found. (2018). *The Asahi Shimbun*. Retrieved from http://www.asahi.com/ajw/articles/AJ201809110026.html

Death toll rises after earthquake on Japan's Hokkaido Island. (2018). *Al Jazeera*. Retrieved from https://www.aljazeera.com/news/2018/09/death-toll-rises-earthquake-japan-hokkaido-island-180910073306436.html

Fire and Disaster Management Agency (FDMA), (2018). *Disaster Information Detail Report*. Retrieved from http://www.fdma.go.jp/bn/2018/detail/1074.html). [In Japanese].

Geospatial Information Authority of Japan(GSI). (2018). National Web Map.

Harder, Leslie F. Jr., "Performance of Earth Dams During the Loma Prieta Earthquake" (1991). International Conferences on Recent Advances in Geotechnical Earthquake Engineering and Soil Dynamics. 11. http://scholarsmine.mst.edu/icrageesd/02icrageesd/session12/11

Hokkaido Electric Power Companyl, I. H. (2018a). On the damage situation and recovery prospect of our transmission and distribtuion facility due to the Hokkaido Eastern Earthquake (Part 3) [Press release]. Retrieved from http://www.hepco.co.jp/info/2018/1231121_1753.html [In Japanese].

Hokkaido Electric Power Companyl, I. H. (2018b). *On the damage situation and recovery prospect of our transmission and distribution facility due to the Hokkaido Eastern Earthquake (Part 2)*. Retrieved from http://wwwa.hepco.co.jp/pdf/18091601.pdf [In Japanese].

Hokkaido Electric Power Companyl, I. H. (2018c). President's press conference remarks summary [Press release]. Retrieved from http://www.hepco.co.jp/info/info2018/1229671_1762.html [In Japanese].

Hokkaido Electric Power Companyl, I. H. (2018d). Press releases on the 2018 East Iburi Earthquake power outage Retrieved from http://www.hepco.co.jp/h30_iburi_earthquake/index.html [In Japanese].

Hokkaido Electric Power Companyl, I. H. (2018e). *Report on the power outage and recovery correspondence during the earthquake*. Retrieved from http://www.hepco.co.jp/info/info2018/__icsFiles/afieldfile/2018/11/01/181101b.pdf. [In Japanese].

Ishia, M., Soya, T., and Suda, Y. (1980). *Geological Map of Sapporo, Hokkaido.* .

Ishii, J. (1963). The weathering processes of volcanic ash and pumice deposits in Hokkaido. *Journal of the Faculty of Science, Hokkaido University. Series 4, Geology and mineralogy= 北海道大學理學部紀要, 11*(4), 545-569.

Isomi, H. (1965). *Tectonic map of Japan*: Geological Survey of Japan.

Japan Meteorological Agency (JMA). Past Meteorological Data Search.https://www.data.jma.go.jp/obd/stats/etrn/index.php

Japan Meteorological Agency (JMA). (2018a). Press Release on September 14, 2018 [Press release]. Retrieved from https://www.jma-net.go.jp/osaka/topics/H30/20180914takashio.pdf

Japan Meteorological Agency (JMA), (2018b). *Prompt Weather Report from August 13 to 18, 2018*. Retrieved from https://www.jma-net.go.jp/sapporo/tenki/yohou/saigai/pdf/KishoH300813-0818.pdf

Japan Meteorological Agency (JMA), (2018c). Tropical Cyclone Information [Press release]. Retrieved from https://www.data.jma.go.jp/fcd/yoho/typhoon/route_map/bstv2018.html

Jayaram, N., and Baker, J. W. (2009). Correlation model for spatially distributed ground-motion intensities, Earthquake Engineering and Structural Dynamics 38, 1687–1708

Kishida, T., Stewart, J.P., Graves, R.W., Midorikawa, S., Miura, H., Bozorgnia, Y., and Campbell K.W. (2013). Comparison of ground motion attributes from 2011 Tohoku-oki mainshock and two subsequent events, in Proceedings 10th International Conf. on Urban Earthquake Engin., Center for Urban Earthquake Engineering, March 1-2, 2013, Tokyo Institute of Technology, Tokyo, Japan.

Kobayashi, C. and McKirdy, E. (2018). Typhoon Jebi leaves trail of destruction in Japan. *CNN*. Retrieved from https://www.cnn.com/2018/09/04/asia/japan-typhoon-jebi-intl/index.html

Kwak, D. Y., Mikami, A., Brandenberg, S. J., and Stewart, J. P. (2012). Ground motion estimation for evaluation of levee performance in past earthquakes, in Proceedings of the 9th International Conference on Urban Earthquake Engineering, 4th Asia Conference on Earthquake Engineering, Center for Urban Earthquake Engineering, 6–8 March 2012, Tokyo Institute of Technology, Tokyo, Japan.

Kwak, D. Y., Stewart, J. P., Brandenberg, S. J., and Mikami, A. (2016). Characterization of seismic levee fragility using field performance data, Earthquake Spectra 32, 193–215.

Kyodo. (2018). 13,000 fled to 768 evacuation centers in Hokkaido after powerful quake. *The Japan Times*. Retrieved from https://www.japantimes.co.jp/news/2018/09/25/national/13000-fled-768-evacuation-centers-hokkaido-powerful-quake/#.XBRFo2hKiUl

Machida, H. (1999). The stratigraphy, chronology and distribution of distal marker-tephras in and around Japan. *Global and Planetary Change, 21*(1-3), 71-94.

Marafi, N. A., Eberhard, M. O., Berman, J. W., Wirth, E. A., & Frankel, A. D. (2017). Effects of deep basins on structural collapse during large subduction earthquakes. *Earthquake Spectra, 33*(3), 963-997.

McCurry, J. (2018). Typhoon Jebi: Japan hit by strongest storm of 25 years. *The Guardian*. Retrieved from https://www.theguardian.com/world/2018/sep/04/typhoon-jebi-japan-hit-by-strongest-storm-for-25-years

Minato, M., Hashimoto, S., Fujiwara, Y., Kumano, S., & Okada, S. (1972). Stratigraphy of the Quaternary Ash and Pumiceous Products in Southwestern Hokkaido, N. Japan (The Pliocene and Quaternary Geology of Hokkaido, 1st Report). *Journal of the Faculty of Science, Hokkaido University. Series 4, Geology and mineralogy= 北海道大學理學部紀要, 15*(3-4), 679-736.

Miura, S., Yagi, K., & Asonuma, T. (2003). Deformation-strength evaluation of crushable volcanic soils by laboratory and in-situ testing. *Soils and Foundations, 43*(4), 47-57.

Nowicki Jessee, M., Hamburger, M., Allstadt, K., Wald, D., Robeson, S., Tanyas, H.,... Thompson, E. (2018). A Global Empirical Model for Near-Real-Time Assessment of Seismically Induced Landslides. *Journal of Geophysical Research: Earth Surface, 123*(8), 1835-1859.

Okada, H. (1982). Geological evolution of Hokkaido, Japan: an example of collision orogenesis. *Proceedings of the Geologists' Association, 93*(2), 201-212.

On the 2018 East Iburi Earthquake power restoration and outage. (2018). Retrieved from https://unavailable.jp/days/jpnews/hokkaido-earthquake-blackout/ [In Japanese].

Osaka Regional Headquarters, JMA: Press Release on September 14, 2018 (in Japanese) https://www.jma-net.go.jp/osaka/topics/H30/20180914takashio.pdf

Saito, M., Bamba, T., Sawa, T., Narita, E., Igarashi, T., Yamada, K., & SATOH, H. (1967). Metallic and Nonmetallic Mineral Deposits of Hokkaido. Geological Survey of Japan, 575p.

Scasserra, G., Stewart, J. P., Bazzurro, P., Lanzo, G., and Mollaioli, F. (2009). A comparison of NGA ground-motion prediction equations to Italian data, Bulletin of the Seismological Society of America 99, 2961–2978.

Seyhan, E., Stewart, J.P., Ancheta, T.D., Darragh, R.B., Graves, R.W. (2014). NGA-West 2 site database, Earthquake Spectra, 30, 1007-1024.

Somerville, P. G., Smith, N. F., Graves, R.W., and Abrahamson, N. N. (1997). Modification of empirical strong ground motion attenuation relations to include the amplitude and duration effects of rupture directivity, Seismological Research Letters 68, 199–222.

Stafford, P. J. (2012). Evaluation of structural performance in the immediate aftermath of an earthquake: a case study of the 2011 Christchurch earthquake, International Journal of Forensic Engineering 1, 58–77.

Stewart, J. P., Lanzo, G., Pagliaroli, A., Scasserra, G., Di Capua, G., Peppoloni, S., Darragh, R. B., and Gregor, M. (2012). Ground motion recordings from the Mw 6.3 2009 L'Aquila earthquake in Italy and their engineering implications, Earthquake Spectra 28, 317–345.

The Straight Times (2018). "Swift assistance needed to rehabilitate Hokkaido's quake-stricken industries: *The Yomiuri Shimbun*." Retrieved from https://www.straitstimes.com/asia/east-asia/swift-assistance-needed-to-rehabilitate-hokkaidos-quake-stricken-industries-the

Taira, A. (2001). Tectonic evolution of the Japanese island arc system. *Annual Review of Earth and Planetary Sciences, 29*(1), 109-134.

Wang, P., Stewart, J.P., Bozorgnia, Y., Boore, D.M., Kishida, T. (2017). "'R"'Package for computation of earthquake ground-motion response spectra" Report No. 2017/09, Pacific Earthquake Engineering Research Center, UC Berkeley.

Watson-Lamprey, J., and Boore, D. M. (2007). Beyond SaGMRotI: conversion to SaArb, SaSN, and SaMaxRot, Bulletin of the Seismological Society of America 97, 1511–1524.

Wells, D. L., and Coppersmith, K. J. (1994). New empirical relationships among magnitude, rupture length, rupture width, rupture area, and surface displacement, Bulletin of the Seismological Society of America 84, 974–1002.

Yanagida, M. (1994). Age of the Shikotsu pumice fall-1 deposit. *The Quaternary Research (Daiyonki-Kenkyu), 33*(3), 205-207.

Zimmaro, P., Scasserra, G., Stewart, J.P., Kishida, T., Tropeano, G., Castiglia, M., Pelekis, P. (2018). Strong Ground Motion Characteristics from 2016 Central Italy Earthquake Sequence. Earthquake Spectra, 34, 1611-1637.

Appendices

A.1. Ground Motion Database

This appendix identifies an electronic database of station and associated ground motion records in the region. Shown below is an exert from the electronically available data set.

Table A-1. Ground motion database for the 2018 Mw 6.6 Hokkaido Eastern Iburi Earthquake.

Sta_ID	Longitude	Latitude	Vs30	Rjb	Rrup	station_na	Vs30_Mea	Vs30_Cod	PGA_Rot5	PGV_Rot5	PGD_Rot5	T0.010S	T0.020S	T0.022S	T0.025S
ABSH04	143.0767	44.192	1135.9	183.4397	188.0148	TAKINOUE	1	0	0.001423	0.2011	0.069026	0.001423	0.001425	0.001425	0.001427
ABSH07	143.0861	43.8494	290.3	152.5715	158.0427	SHIRATAK	1	0	0.014886	1.642255	0.442975	0.014908	0.014976	0.014993	0.015021
ABSH13	143.4514	43.7419	463.6	164.4962	169.5832	RUBESHIB	1	0	0.007047	1.08221	0.388688	0.007056	0.007084	0.007093	0.007105
ABSH15	143.51	43.6352	464.9	160.863	166.0613	OKETO-E	1	0	0.00771	0.819381	0.20679	0.007715	0.007741	0.007748	0.007765
AOM001	140.9244	41.5267	447.4	144.6844	147.4919	OHMA	1	1	0.027496	1.293337	0.165773	0.027623	0.028026	0.028147	0.028346
AOM002	140.8132	41.328	418.3	168.129	170.551	FUKUURA	1	1	0.023325	0.720122	0.048889	0.023475	0.023983	0.024155	0.024463
AOM003	141.1691	41.4053	179.8	145.7944	148.5809	OHHATA	1	1	0.058861	3.002488	0.484019	0.059068	0.059915	0.060241	0.060736
AOM004	141.4486	41.4087	376.7	136.7215	139.6891	SHIRIYA	1	1	0.022749	0.957024	0.126756	0.023094	0.024205	0.024554	0.025144
AOM005	141.1972	41.2948	293.4	155.9675	158.5754	MUTSU	1	1	0.052997	3.025329	0.687609	0.053197	0.053842	0.054002	0.05439
AOM006	140.9972	41.1976	272	172.8741	175.2306	KAWAUCH	1	1	0.029913	1.495533	0.209144	0.030002	0.030274	0.030348	0.030486
AOM007	141.3846	41.169	284.1	163.7703	166.2558	MINAMID	1	1	0.027692	0.96242	0.125011	0.027847	0.028279	0.028402	0.028603
AOM008	141.2552	41.084	373.6	176.0811	178.3952	YOKOHAM	1	1	0.030007	1.435173	0.176632	0.030217	0.030882	0.031097	0.03148
AOM009	141.3733	40.9665	337.4	185.7058	187.9014	42203	0	2_4c	0.017358	0.914722	0.183675	0.017433	0.017676	0.01775	0.017876
AOM027	140.8219	41.1453	308.5	184.9953	187.1992	WAKINOS	1	1	0.015777	0.966198	0.11055	0.015812	0.015921	0.015952	0.016008
AOMH01	140.9127	41.5273	302	145.2003	147.998	OOMA	1	0	0.044953	1.63999	0.337562	0.045152	0.04573	0.045894	0.046172
AOMH03	140.9896	41.234	653.7	169.5717	171.9734	KAWAUCH	1	0	0.012949	1.013883	0.249016	0.013004	0.013188	0.013253	0.013363
AOMH06	141.3738	40.9664	385.6	185.7058	187.9014	ROKKASY(	1	0	0.035295	1.316647	0.206892	0.035437	0.035856	0.03598	0.036216
HDKH01	142.2296	42.7031	368.3	19.31905	38.88025	BIRATORI-	1	0	0.568064	40.25526	3.750223	0.568831	0.571318	0.572136	0.575147
HDKH03	142.3521	42.5934	341.1	26.3794	43.38801	MONBETS	1	0	0.317185	14.45104	1.374954	0.317777	0.319528	0.319984	0.320846
HDKH04	142.0381	42.5126	235	9.725651	30.3709	MONBETS	1	0	0.410117	44.88541	10.72268	0.410449	0.412293	0.412766	0.414029
HDKH05	142.5446	42.5977	766.2	42.10018	56.20085	NIIKAPPU	1	0	0.062384	3.768289	0.721836	0.062485	0.062922	0.063064	0.063235
HDKH06	142.3572	42.3498	412.2	39.26083	50.63015	SHIZUNAI	1	0	0.165232	17.94418	4.083704	0.165353	0.165679	0.165758	0.16588
HDKH07	142.9164	42.133	459.1	89.91778	97.63009	SAMANI	1	0	0.03675	2.600395	0.695158	0.036796	0.036938	0.036979	0.037049
HKD019	141.6978	44.3611	325.2	177.3992	182.0662	HABORO	1	1	0.008712	1.755239	0.608057	0.008715	0.008719	0.008721	0.008724
HKD020	141.6642	44.1486	614.5	154.2408	159.2718	MINATOM	1	1	0.007994	1.124721	0.306339	0.008002	0.008031	0.008037	0.008045
HKD021	141.637	43.9407	315.1	131.7233	136.9857	RUMOI	1	1	0.038613	3.348811	0.634844	0.038654	0.038797	0.038833	0.038864
HKD022	141.5275	43.8515	370.8	123.9096	128.8234	MASHIKE	1	1	0.031826	4.667879	1.287498	0.031917	0.032195	0.032272	0.032363
HKD023	141.3685	43.7735	270.1	119.6896	123.9104	OFUYU	1	1	0.036229	2.158348	0.269882	0.036266	0.036388	0.036426	0.036503
HKD024	141.8573	44.0489	373.7	141.892	147.6005	TATSUPU	1	1	0.013539	1.146908	0.21604	0.013563	0.013633	0.013654	0.013688
HKD027	142.3427	44.4806	447.8	192.9023	197.2581	BIFUKA	1	1	0.004464	1.504762	0.584626	0.004465	0.004468	0.004469	0.004471
HKD028	142.4547	44.3598	413.3	181.6507	186.2697	NAYORO	1	1	0.006722	1.068873	0.306226	0.006724	0.006728	0.006729	0.006731
HKD029	142.6419	44.3111	442	180.7095	185.352	SHIMOKA'	1	1	0.004743	0.997813	0.41698	0.004744	0.004748	0.004749	0.004751

B.1. UAV And Lidar Data

An emphasis of this GEER reconnaissance was the collection of both UAV and terrestrial lidar scan (TLS) data utilizing NHERI-RAPID equipment and data processing capabilities. These data were then developed into 3D point-cloud models and uploaded to DesignSafe to preserve these post-earthquake data and make them available to anyone within the hazards community for future research.

B.1.1. Coverage And Collection

A total of 7 TLS scans (merged into 5 models) and **Z** UAV flights of **Y** sites were collected during our reconnaissance (**Figure B.1**). TLS data were collected using a Maptek I-Site XR3 lidar scanner capable of a maximum range of ~2.4km. Data were collected to a maximum range of ~1.6km in this reconnaissance. Scans were typically collected at a nominal resolution of xxx points per m^2 at 100m, to facilitate coverage of several sites over highly detailed scanning of individual features. Ground control was established from the XR3 internal GPS. Therefore, precise measurements from these data may be more uncertain than a traditional survey-grade lidar collection effect. Individual lidar scans were merged into a composite point cloud using Maptek's I-suite software. [[[couple sentences about UAV platform and standard settings]].

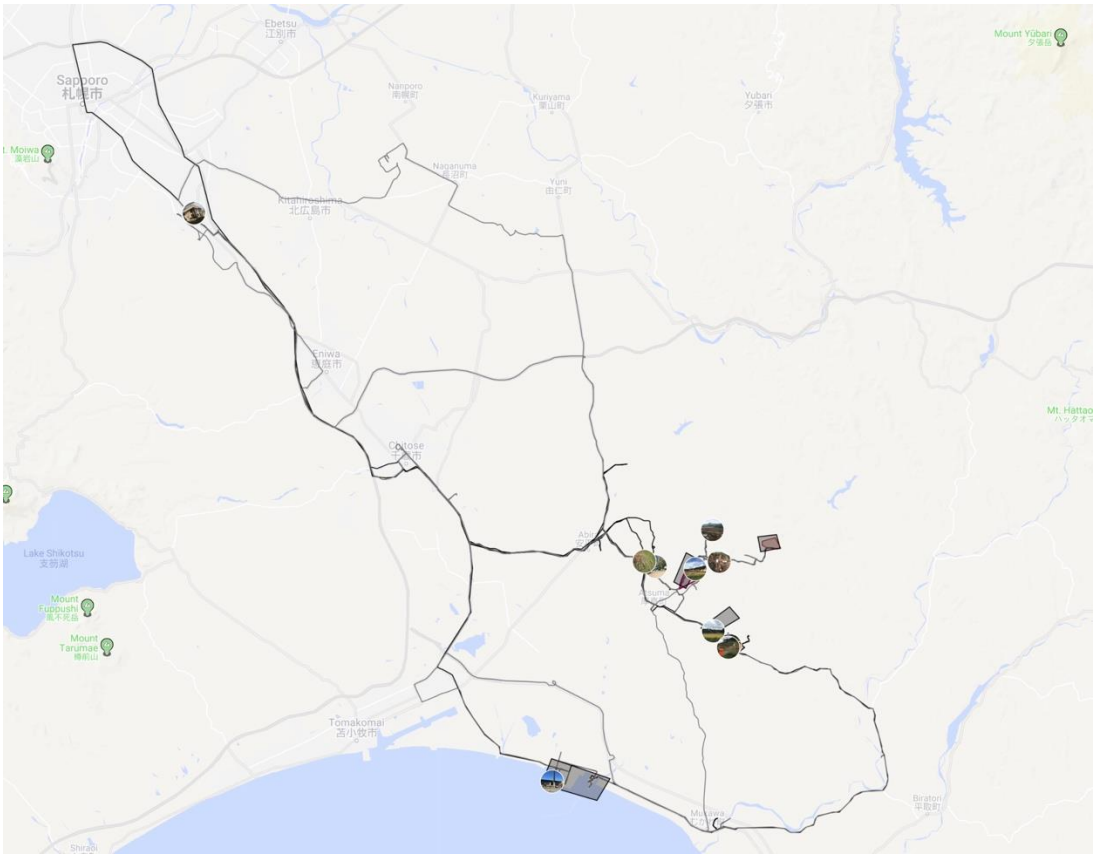

Figure B.1 Map showing the locations and data extent of TLS and UAV data collected during this GEER reconnaissance. This map and links to the data represented here are available at: https://drive.google.com/open?id=1rK_A-V_SH_S62tSGDVEl_vbE9SNnqYy8&usp=sharing

B.2.1. Accessibility

Data needs to be fully uploaded into DesignSafe and made public for this section to be fully relevant / useful. Skeleton below we should add final details into.

All data collected on this reconnaissance are available from DesignSafe,. This project, and individual datasets can be accessed via the map shown in Figure X.1 here:

https://drive.google.com/open?id=1rK_A-V_SH_S62tSGDVEl_vbE9SNnqYy8&usp=sharing

Thumbnail images for each TLS and UAV data point provide links to the relevant data.

Find and view DesignSafe lidar / UAV data with Potree

Sign into DesignSafe, (designsafe-ci.org)

Find the data:

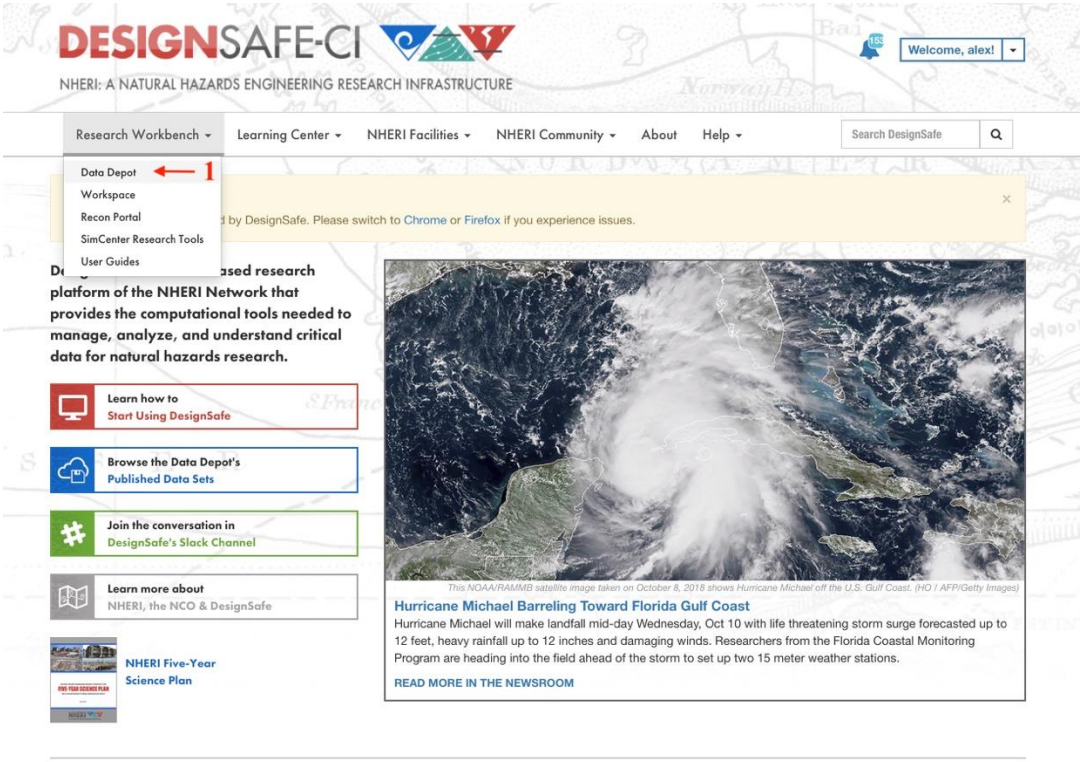

Under the Research Workbench tab, select ‘Data Depot’

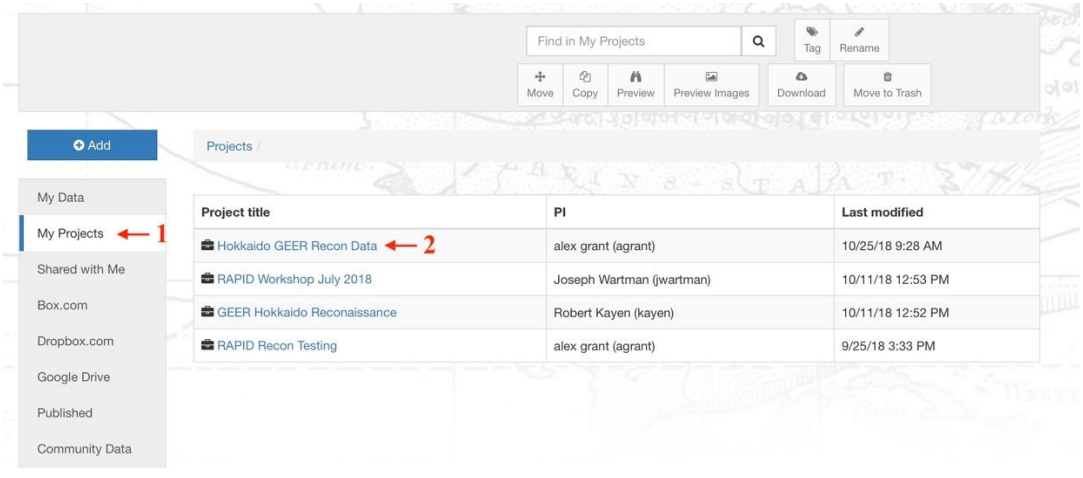

Here you can connect to personal data, shared public/private projects, published datasets, or drobox etc., externally hosted data. Our Hokkaido data is in the folder ‘Hokkaido GEER Recon Data’

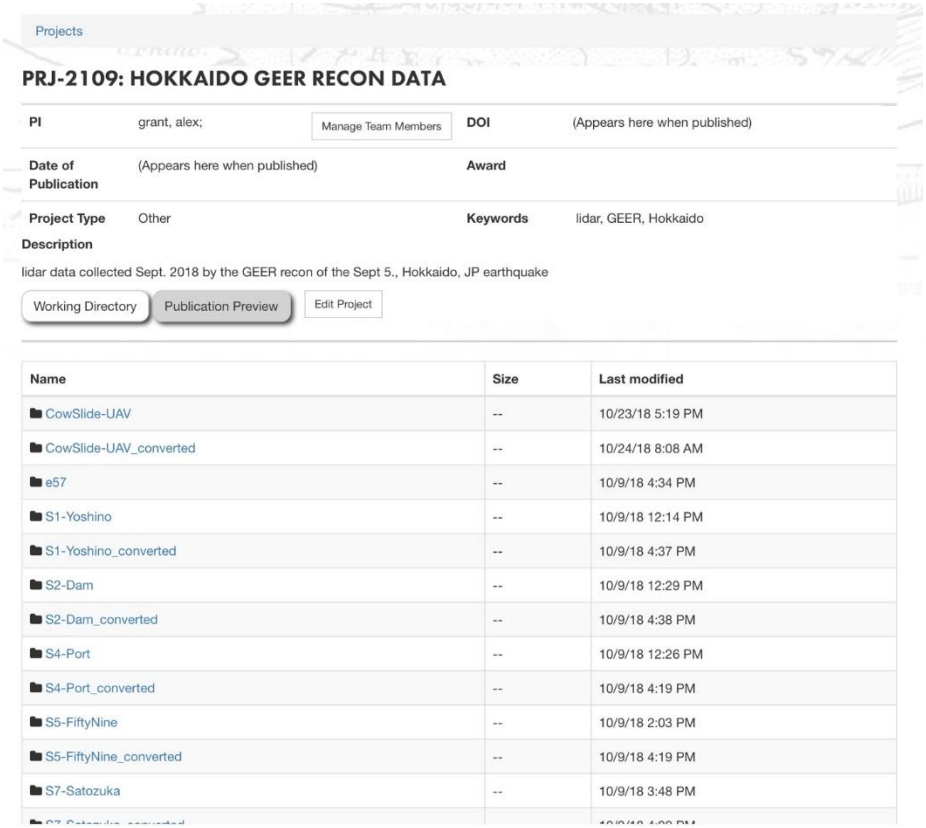

Directory of .las, .e57, and potree converted lidar and UAV data collected during the reconnaissance. When published and with a DOI users will be able to directly access this directory

Look at the data

Return to the Research Workbench tab and select ‘Workspace’

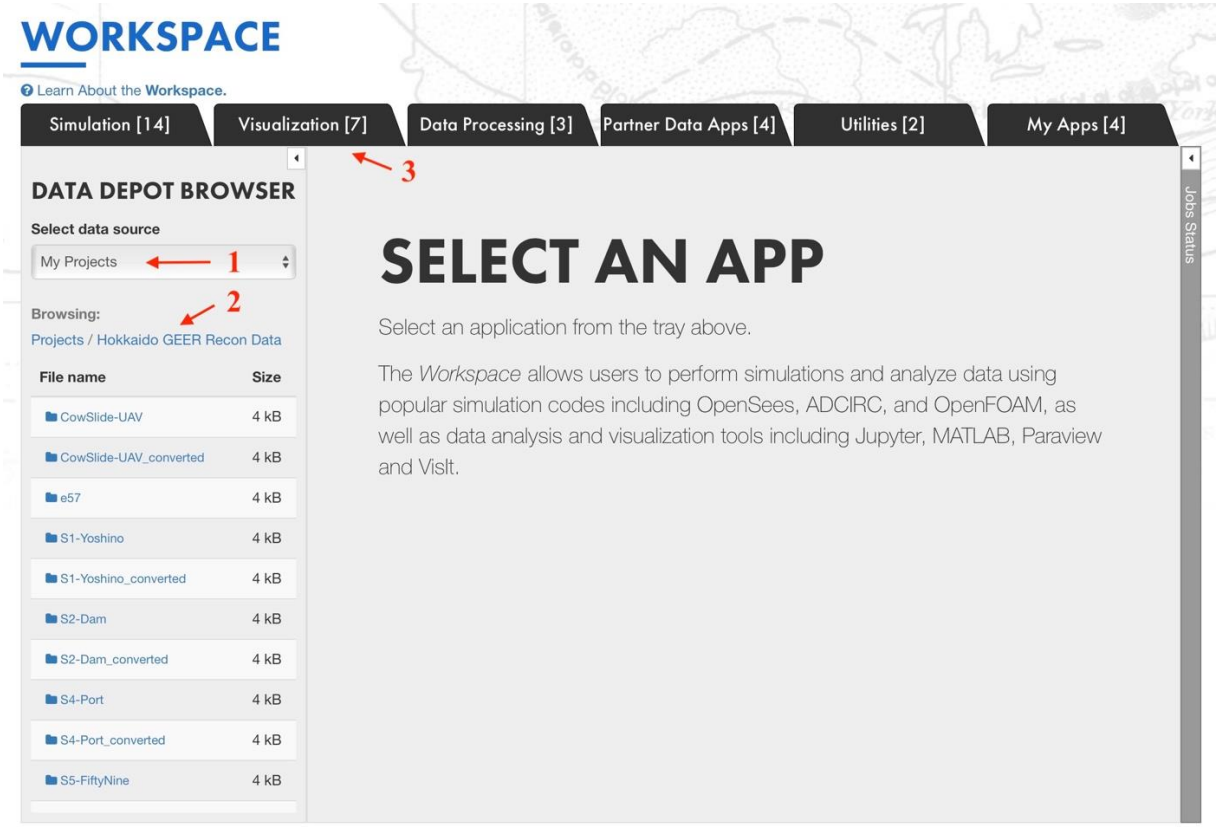

In the workspace, change your data source to ‘my projects’ (or wherever your data are), select the parent folder of the data you’re interested in (Cow Slide UAV data here), and select the Visualization tab.

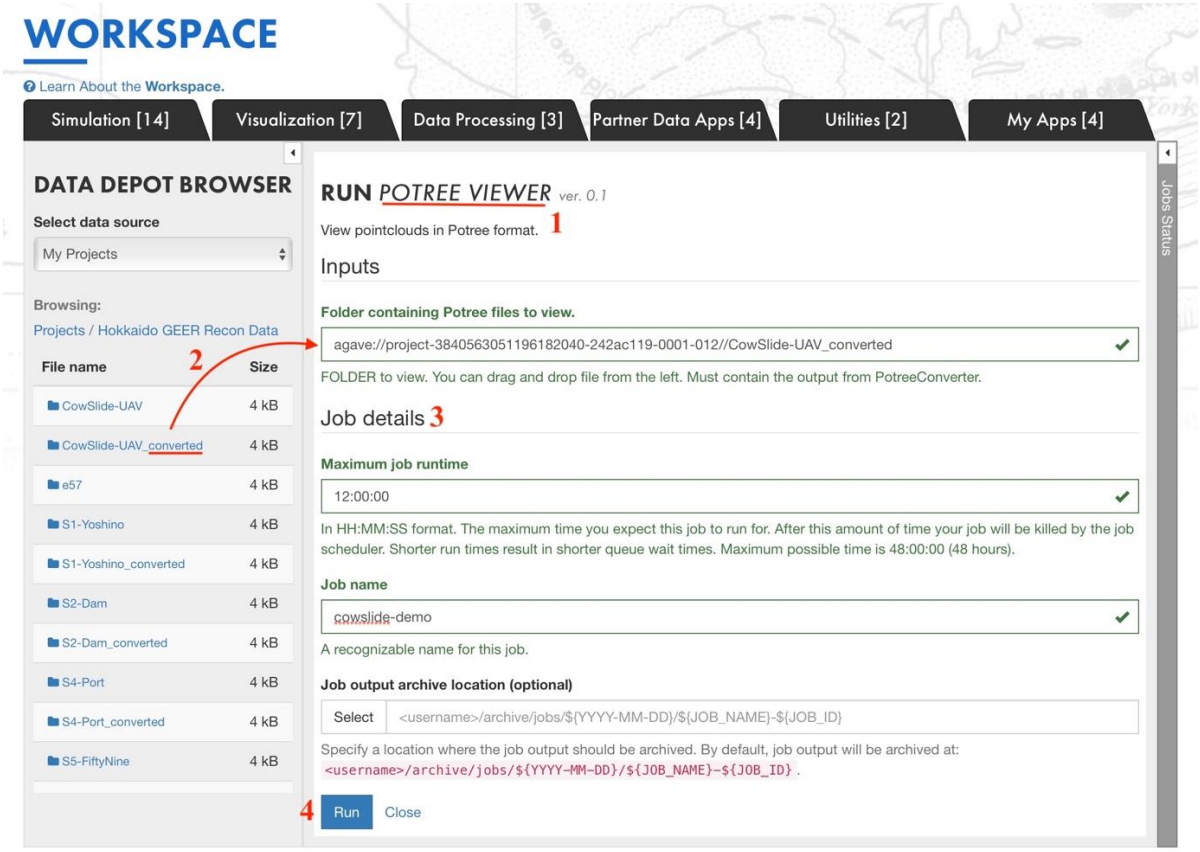

Select 'Potree Viewer' and then drag and drop the '*_*converted'* folder of interest into the top input. Fill in the remaining job details (runs capped at 24hr) and select run.

Wait. (Usually 1 – 5min)

This window will appear:

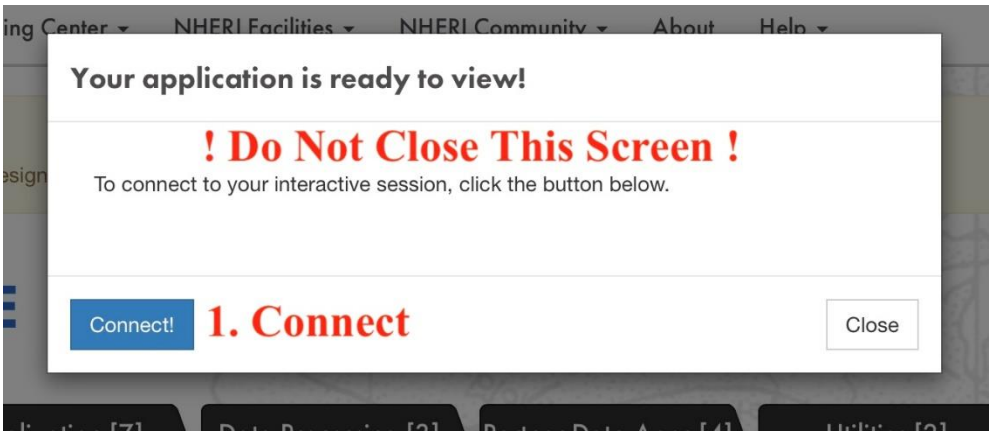

As of writing, this is the only chance you have to link to the virtual machine you have created. Click connect.

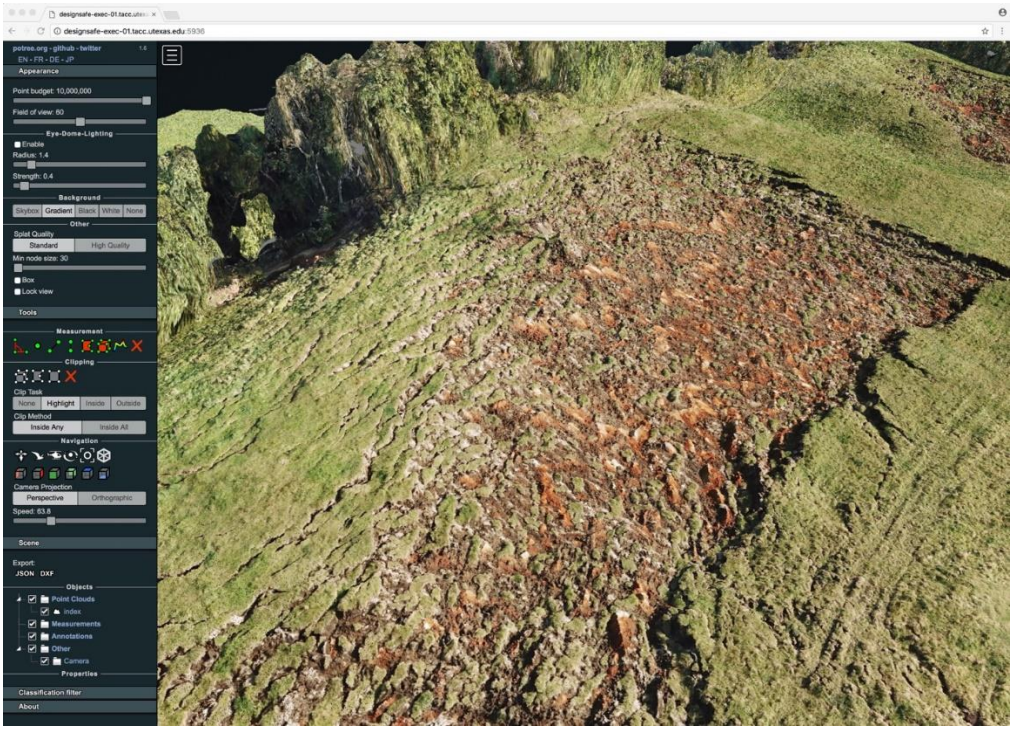

You can now explore the data*, start by copying the url and saving it somewhere. You can reconnect via this public URL, but DesignSafe will not reconnect you any other way. Second, move the top-left slider (point budget) all the way to the right for max resolution.

*in Chrome of Firefox, this part does not work in Safari.